Negative microfilm
received from university

66-6659

MOORE, John William, 1938-
THE STRUCTURE AND PROPERTIES OF ORIENTED COMPOUND EUTECTICS.

The University of Michigan, Ph.D., 1965
Engineering, metallurgy

University Microfilms, Inc., Ann Arbor, Michigan

THE STRUCTURE AND PROPERTIES OF ORIENTED COMPOUND EUTECTICS

John William Moore

A dissertation submitted in partial fulfillment
of the requirements for the degree of
Doctor of Philosophy in the
University of Michigan
1965

Doctoral Committee:

Professor Lawrence H. Van Vlack, Chairman
Professor Wilbur C. Bigelow
Professor William F. Hosford
Professor Donald R. Peacor
Professor Lars Thomassen

ACKNOWLEDGMENTS

It is a pleasure for the author to acknowledge the many people who have contributed to this investigation. I am especially indebted to the following:

Professor L. H. Van Vlack, whose example, guidance and support in both research and teaching have been invaluable throughout my training at the University.

Professors W. C. Bigelow, W. F. Hosford, D. R. Peacor, L. Thomassen and R. M. Denning for their cooperation, criticism and assistance throughout the course of the investigation.

Drs. Gerald I. Madden, Otto K. Riegger and James M. Dahl for the many stimulating discussions of this work.

Diane L. Schaafsma for her able assistance in editing and typing the manuscript and guiding it through the final printing and distribution.

The Office of Research Administration for the drafting of figures and reproduction of the thesis.

Messrs. Bolen, Connell, Darling, Drogosz, Reed, Sevarin and Wurster of the University staff for their assistance in the experimental phases of the thesis.

Finally, to my wife, Diann P. Moore, who has provided the support, encouragement and understanding which has made the satisfactory completion of my graduate studies possible.

To My Wife

TABLE OF CONTENTS

	Page
LIST OF TABLES	v
LIST OF FIGURES	vi-viii
CHAPTER	
I. INTRODUCTION	1
II. LITERATURE REVIEW	3
A. Eutectic Phase Relationships	3
B. Eutectic Microstructure	6
C. Crystallographic Relationships	19
D. Property Relationships	26
1. Hardness	28
2. Deformation and Fracture	30
a. Single Crystals	31
b. Polycrystals	33
c. Bicrystals	36
3. Thermal Expansion	43
III. EXPERIMENTAL PROCEDURE	45
A. Sample Preparation	45
1. Raw Materials	45
2. Eutectic Ingots	47
3. Sections	50
B. Testing	51
1. Microstructural Analysis	51
2. Crystallographic Orientation	52
3. Thermal Expansion Determination	54

Table of Contents (Concluded)

	Page
4. Deformation and Fracture Analysis	55
5. Hardness Testing	56
IV. RESULTS AND DISCUSSION	57
A. Phase Relationships	57
1. Crystallographic Orientations	57
a. MnO-MnS	58
b. FeO-FeS	64
c. NaCl-NaF	66
d. NaBr-NaF	70
e. LiF-NaF	71
2. Microstructure	72
a. Phase Morphology	72
b. Colony Structure	84
c. Irregularities	96
B. Property Relationships	103
1. Thermal Expansion	103
2. Deformation and Fracture	115
a. Crystallographic Effects	115
b. Microstructural Effects	122
3. Hardness	126
a. Crystallographic Effects	126
b. Microstructural Effects	132
C. Summary of Results	139
V. CONCLUSIONS	146
REFERENCES	150

LIST OF TABLES

Table		Page
I.	Precession X-ray Camera Settings	53
II.	Volume Ratios of Discontinuous Phases	78
III.	Volume Percent of Matrix and Discontinuous Eutectic Phases	141
IV.	MnO Single Crystal Knoop Hardness	144
V.	MnO-MnS Eutectic Knoop Hardness	145

LIST OF FIGURES

Figure		Page
1.	MnO-MnS phase diagram.	4
2.	Impurity effects in liquid ahead of solidifying lamellar eutectic.	16
3.	Growth of octahedra under restricted conditions.	27
4.	Bicrystal tensile specimen with longitudinal boundary.	38
5.	MnS purification.	46
6.	Eutectic unidirectional solidification apparatus.	49
7.	Crystallographic orientations of MnO-MnS and FeO-FeS eutectic phases in relation to lamellar interfaces and growth directions.	59
8.	Buerger precession zero-level x-ray transmission photographs of lamellar MnO-MnS eutectic.	60
9.	Schematic diagram of crystallographic misorientation between MnO and MnS lamellae versus radial curvature direction of solidification front.	62
10.	Crystallographic orientations of NaCl-NaF, NaBr-NaF and LiF-NaF eutectic phases in relation to lamellar interfaces and growth directions.	67
11.	NaCl-NaF Laue exhibiting doubling of spots and second cubic pattern rotated 2° from primary pattern.	69
12.	Lamellar microstructure of the MnO-MnS eutectic.	73
13.	Lamellar microstructure of the LiF-NaF eutectic.	74
14.	Lamellar microstructure of the NaCl-NaF eutectic.	75
15.	Lamellar microstructure of the FeO-FeS eutectic.	76
16.	Microstructure of the NaBr-NaF eutectic.	77
17.	Lamellar spacing versus solidification rate for the MnO-MnS eutectic compared with alkali halide eutectic data of Penfold and Hellawell and this study.	80

List of Figures (Continued)

Figure		Page
18.	Lamellar spacing versus the inverse square root of solidification rate for MnO-MnS and LiF-NaF.	82
19.	Transverse cross section of MnO-MnS eutectic colonies.	85
20.	Transverse cross section of NaBr-NaF eutectic colonies.	86
21.	Colony development along MnO-MnS eutectic ingot.	88
22.	Longitudinal section of grain and colony boundaries in MnO-MnS eutectic.	89
23.	Longitudinal section of MnO-MnS eutectic ingot showing transverse band outlining domed solidification front.	90
24.	Transverse and longitudinal sections of MnO-MnS eutectic ingots showing microstructure and outline of solidification front near crucible wall.	91
25.	Transverse section of MnO-MnS eutectic colonies showing stability of lamellae growing radially to colony boundary.	93
26.	Transverse section of MnO-MnS ingot showing lamellae growing radially to the outer periphery of ingot.	95
27.	Dendrites of MnO, MnS and Fe in transverse sections of MnO-MnS eutectic ingots.	97
28.	Pronounced colony structure and MnS "discs" in transverse section at top of MnO-MnS ingot.	99
29.	Iron globules associated with lamellar flaws in MnO-MnS eutectic.	104
30.	Iron globules segregated to low angle boundaries in MnO-MnS eutectic.	105
31.	Linear thermal expansions for MnO, MnS, MnO-MnS eutectic and Fe from room temperature to 1000°C.	106

Figure

Page

32. Lattice parameter versus temperature for MnS, MnO and Pt. 108

33. Experimental mean linear thermal expansion coefficients of MnO, MnS and the MnO-MnS eutectic compared with various calculated eutectic values. 111

34. Dispersed phase particles in low angle boundary and kink in crack at Vickers indentation in MnO single crystal. 117

35. Slip lines and fractures around Vickers indentations on (100) surface of MnO single crystal. 118

36. Slip lines and fractures around Vickers indentations on (110) surface of MnO single crystal. 119

37. Slip lines and fractures around Vickers indentations on (11$\bar{2}$) surface of MnO-MnS eutectic. 124

38. Vickers indentations on (111) and (110) surfaces of MnO-MnS eutectic. 125

39. Crystallographic variations in Knoop Hardness Number for MnO and MnS single crystals. 127

40. Crystallographic variations in Knoop Hardness Number for MnO, MnS and the MnO-MnS eutectic. 130

41. Microstructural variations in the Knoop Hardness Number for the MnO-MnS eutectic. 134

CHAPTER I

INTRODUCTION

This investigation is concerned with the growth of oriented ceramic composites by unidirectional eutectic solidification and the relationships between the microstructure, crystallographic orientations, plastic deformation, fracture, hardness and thermal expansion of such composites.

This problem was chosen because it was felt that eutectic unidirectional solidification, recently developed in metallic systems, might provide a valuable technique for fabrication of uniform, oriented ceramic and ceramic-metal engineering materials. Furthermore, if simple two-phase ceramic microstructures could be grown, they would provide a valuable intermediate step in the process of relating single crystal ceramic properties to those of isotropic polycrystalline ceramic aggregates.

It was hypothesized that (1) binary eutectic mixtures of ionic compounds could be unidirectionally solidified to form microstructurally and crystallographically oriented two-phase ceramic composites with a fibrous or lamellar dispersed phase and that (2) the structure-sensitive physical properties of these two-phase ceramic composites would vary with orientation but be related by some mixture rules to the properties of similarly oriented single crystals of the component phases.

The idea for this work came from observing small

regions of a fibrous dispersion of MnO in an impure manganese sulfide (MnS) ingot prepared for a study of the MnO-MnS phase diagram.[1] Therefore, in order to capitalize on the phase data as well as the preparation techniques and physical property data available for MnS, the major portion of this study was performed on the MnO-MnS system. The microstructure and crystallographic orientations of the phases in the FeO-FeS, NaCl-NaF, NaBr-NaF and LiF-NaF eutectics were also studied in order to determine whether the growth and orientation results of the MnO-MnS study were generally applicable to ionic compound eutectics with different crystal structures and ion size ratios.

Knoop and Vickers micro-indentation hardness procedures were chosen as the principal physical property tests since they are relatively nondestructive, well suited to the scale of the microstructures obtained and can provide information on both plastic deformation and fracture mechanisms. Thermal expansion was studied by x-ray and dilatometric techniques since it was felt that an understanding of the thermal stresses caused by cooling the composite from the eutectic solidification temperature to room temperature would be necessary to the analysis of the interaction of the individual phase properties in the composite structure.

CHAPTER II

LITERATURE REVIEW

This literature review summarizes and discusses previously reported material which was utilized in this investigation or which contributes to the understanding of the results obtained.

The review is divided into four main sections:

A. Eutectic Phase Relationships
B Eutectic Microstructure
C. Crystallographic Relationships
D. Property Relationships

A. Eutectic Phase Relationships

The eutectic reaction is defined as "the isothermal, reversible reaction of a liquid that forms two different solid phases (in a binary alloy system) during cooling."[2] The MnO-MnS phase equilibrium diagram is a typical binary eutectic (Figure 1). The phase equilibrium diagrams for FeO-FeS, NaCl-NaF, LiF-NaF and NaBr-NaF-NaI were also used in this study to determine approximate eutectic compositions.[3]

Various theories[4, 7] have been proposed to predict the phase ratios at which eutectic compositions will occur. Stockdale in 1935 first suggested that the compositions of binary metallic eutectic points corresponded with simple whole number ratios of the two kinds of atoms.[4] Gorboff[5] (1909) and Desch[6] (1910) had earlier observed that in

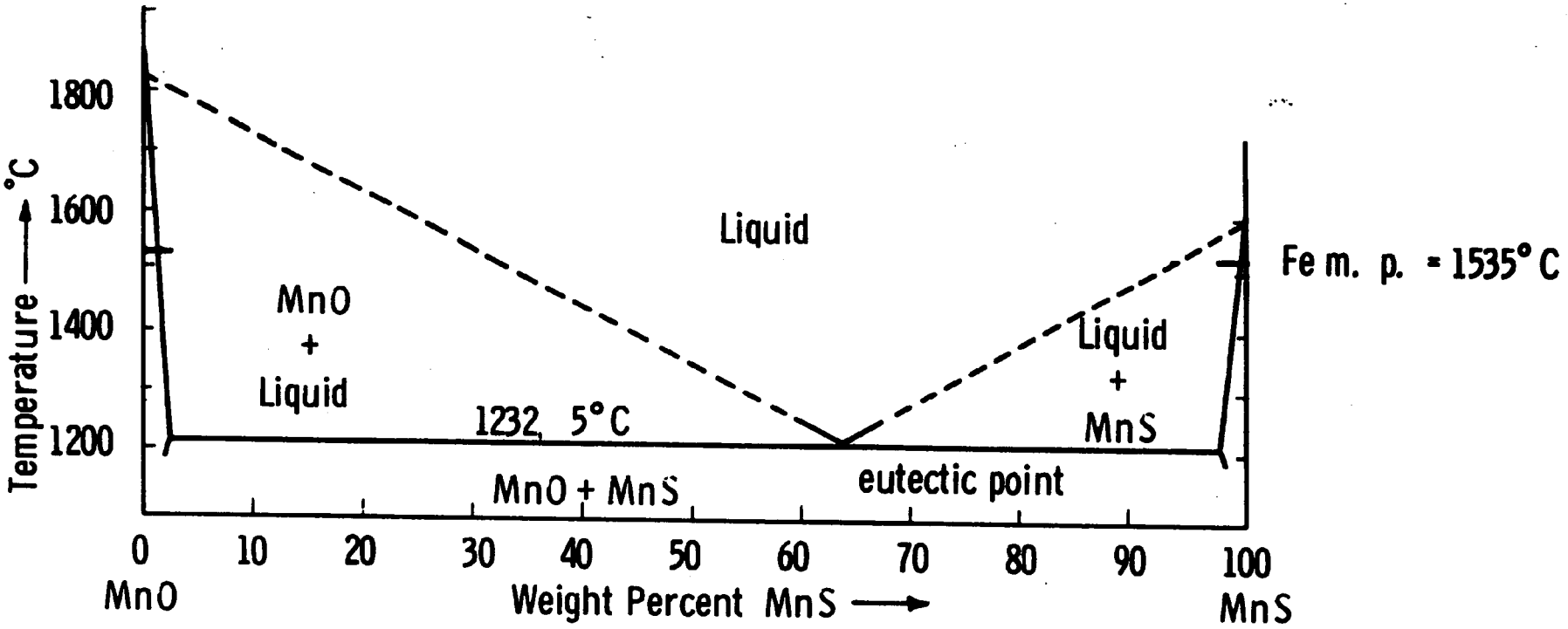


Figure 1. MnO-MnS phase diagram after Chao, Smith and Van Vlack.[1]

certain organic, inorganic and intermetallic compound systems the eutectic phase proportions seemed to be such that one of the components was equally distributed between the phases. No theoretical basis has been found for this proposal, however, and it does not apply at all to eutectics formed by terminal solid solutions such as those used in this study.

Hume-Rothery and Anderson[7] have recently re-examined all available experimental data on eutectic alloy proportions and have concluded that Stockdale's original proposal seems to have some merit for predicting the most probable eutectic composition ratios.

The alkali halide eutectic compositions of this study were melted in graphite crucibles, but since no significant crucible-melt interactions were suspected or observed, carbon-alkali halide phase equilibria will not be discussed. The FeO-FeS and MnO-MnS eutectics were melted in high purity Ferrovac iron crucibles, however, and there was evidence of iron distributed in the eutectic microstructures. The iron-oxygen and iron-sulfur systems have been discussed in great detail by Darken and Gurry.[8] The Fe-Mn-S-O quaternary system[9] and the Fe-S-O ternary system[10] have been discussed qualitatively by Hilty and Crafts. Their results are sufficient to serve at least as a guide to the analysis of the crucible-melt interactions in these systems.

B. Eutectic Microstructure

The earliest commercial eutectics were probably used as solders, at least as early as the Roman occupation of Great Britain.[11] However, the earliest scientific study of minimum melting point mixtures was on the properties of "cryohydrates" of salt and water as reported by Guthrie in 1875.[12] These solids were originally thought to be compounds, but according to Brady,[13] Ponsot in 1895 proved them to be intimate mixtures of the primary phases. The eutectic microstructure develops on solidification by a process of nucleation and subsequent simultaneous growth of the primary phases in directions and with morphologies determined by impurities and growth conditions. The nucleation phenomena are less important to microstructural morphology than to crystallographic orientation; therefore, they will be discussed in that section.

Several empirical attempts have been made to group the many known eutectic systems on the basis of similarities in the appearance of their microstructures.[13, 14, 15, 16, 17] The most recent review, by Chadwick,[17] chooses to divide eutectics into the following microstructural classes:

1. "Continuous" microstructures, wherein both phases are essentially continuous in the growth direction, as in the fibrous and lamellar cases in this study.

2. "Discontinuous" microstructures, wherein there

is no continuity in the phase which is dispersed as discrete particles in the matrix phase.

3. "Spiral" microstructures, wherein interlocking, spiral platelets of the two phases exist.

Since all five of the ceramic eutectic systems in this investigation exhibited the continuous or first type of microstructure, this review will be limited to the literature applicable to this type.

A study of the microstructure of metallic eutectics can be found as early as 1912 in the work of R. Vogel[18] who related solidification rate to the scale of the eutectic microstructure. He unfortunately worked with the zinc-cadmium system and observed only the colony or eutectic grains and their boundaries without resolving the fine lamellar primary phases. This was rectified by Brady[13] who used magnifications to 800X on etched specimens to prove that the colonies noted by Vogel were themselves made up of an intimate mixture of zinc and cadmium phases as fine lamellae. Brady also noted that the eutectic lamellae became finer with increased severity of quench and that the scale of the microstructure increased from the center to the edge of the colonies. He then attempted to account for the formation of widely varying eutectic microstructural shapes by relating the various shapes noted to the relative surface tensions and melting points of the liquid phases.

Lamplough and Scott[19] in 1914 first noted that there were differences in the appearance of the eutectic

microstructure adjacent to primary particles of the two eutectic phases which correlated with undercooling data, indicating that only one of the two phases was effective in heterogeneously nucleating the eutectic.

Since these earliest studies there have been many attempts to catalog eutectics in terms of their microstructural appearance and to relate microstructure to crystallographic and surface energy relationships between the phases and to various solidification variables.[13, 14, 15, 16, 17, 18, 19]

It has only been since the advent of the zone-refining process for purifying materials, however, that there has been any real progress in understanding eutectic microstructures. The very high purity metallic and covalent elements which have been produced by this process have made possible the preparation of binary eutectics in which third-element effects on microstructure can be essentially eliminated or, at least, controlled. The understanding of single phase solidification phenomena resulting from zone refining research has provided the necessary basis for extension of this work to the two phase solidification occurring in eutectics. The unidirectional solidification technique which is an outgrowth of the zone-refining technique permits the growth of microstructurally and crystallographically oriented eutectics in which the effect of solidification variables on structure can easily be studied.

For obvious reasons most of the eutectic research done to date has been on low melting point metal and metal-

intermetallic compound alloys. In fact, the only other references found on oriented ionic compound eutectics up to the time of this report were those of Hellawell, et al, on the NaCl-NaF and LiF-NaF alkali halide systems.[20, 21, 22, 23]

Pfann's[24] original work on zone-melting was an extension of earlier treatments[25, 26, 27] of solute segregation in normal freezing in which it was shown that the concentration, C, solidifying was a function of the initial solute concentration, C_o, the fraction solidified, g, and the ratio of the solute concentration in the solid to that in the liquid, k:

$$C = k\, C_o\, (1 - g)^{k - 1}.$$

These derivations were based on assumptions that (1) diffusion in the solid is negligible, (2) diffusion in the liquid is complete, and (3) k is constant. Pfann's work showed that it was possible to enhance or eliminate solute segregation by varying growth conditions when traversing a relatively long charge of solid alloy with a small molten zone. Rutter and Chalmers[28] observed and studied a cellular substructure in unidirectionally solidified metal single crystals which indicated that a non-planar solidification interface could be stabilized under certain conditions not predicted by previous theories.

Tiller, Jackson, Rutter and Chalmers[29] extended the understanding of single phase solidification by showing that when convection in the liquid was limited, the finite

liquid metal diffusion coefficients (1-10 cm^2/day) caused local build up of rejected solute ahead of the solidification interface for distribution coefficients less than one. This local solute build up decreased exponentially from the solidifying interface into the liquid with a form governed by the rate of diffusion of solute into the liquid and the rate of emission of solute at the solidifying interface. They also showed that the solute concentration retained in the solid would be very rate sensitive since increased solidification rates would give locally increased solute concentration in the solid and decreased rates would give lower concentrations. This transverse banding or periodic variation in solute concentration in the direction of solidification due to growth rate variations has also been observed in eutectics, notably those of this study.

Rutter and Chalmers[30] showed that the constitutional supercooling and associated cellular interface occur in single phase solidification if the growth rate, R, is too rapid or the temperature gradient, G, in the liquid at the interface is too low for a particular impurity content. Tiller and Rutter[31] showed that such supercooling could stabilize a cellular interface if random growth projections in a planar interface created radial impurity rejection, lowering the freezing temperature of the projection boundaries.

The developments in the understanding of the single phase unidirectional solidification discussed above have

been very important to subsequent understanding of two phase eutectic solidification. Weart and Mack[32] first pointed out the correlation between the "cellular" interface observed in dilute single phase alloys and the "colony" substructure which was the major disturbing influence in the otherwise ordered eutectic microstructures previously obtained. They further pointed out that eutectic grains, which grow from a single nucleus in a manner analogous to single phase grains, must be differentiated from eutectic "colonies." The colony structure is a disturbance in the phase morphology within the essentially monocrystalline matrix phase of a single grain or over a polycrystalline region of several grains. Decanting experiments[32] proved that each "colony" was caused by a single cell dome in the non-planar, cellular solidification interface. The cellular front is stabilized by the presence of a constitutionally supercooled impurity zone ahead of the interface in impure alloys at high growth rates and low temperature gradients. Because of the dome shape of the solidification front of each colony and the evident tendency for the individual phase particles to grow perpendicular to the dome surface, the phase particles must grow in a curving direction towards the boundary of each colony (Figure 22). Since the overall cell groove velocity in the direction of growth must be approximately equal to the growth velocity at the center of each cell, the phase particle growth rates perpendicular to the dome (or cell surface) must decrease.

Previous explanations of the thickening of eutectic phase particles as they curved toward colony boundaries had been based on decrease of surface tension,[13] liberation of latent heat,[33] supercooling effects,[15] and displacement from the eutectic composition.[34] Weart and Mack[32] concluded, however, that the major reason for the thickening was the decrease in solidification rate at the boundaries since other studies[35, 36, 37] showed that lamellar thickness was inversely proportional to growth rate.

The coarsened lamellae or rods of adjacent colonies behind an advancing inter-colony groove gives this region the appearance of a grain boundary, but Fraser and Burr,[38] using a semi-microbeam x-ray technique, and Eastwood,[39] using slip lines, showed that a maximum of 1-2° misorientation existed across colony boundaries.

Tiller[40] had previously shown theoretically that constitutional supercooling could occur in even pure two component alloys such as binary eutectics. This would mean that it would be impossible to eliminate the cellular interface, and therefore the colony substructure, by eliminating impurities in eutectic alloys. However, recent experiments by Chilton and Winegard[41] on zone-refined lead-tin eutectic alloys have shown no evidence of the formation of colony boundaries in even chill-cast sections of these high purity alloys.

Chilton and Winegard, however, verified the prediction of Tiller[40] that the lamellae thickness, λ, would

increase with the decrease of the growth rate, R, as described by

$$\lambda R^{1/2} = \text{constant.}$$

Tiller's prediction was based on the necessity for redistribution of solute ahead of the lamellae in the liquid and surface energy requirements of the solid eutectic phase interfaces. Chilton and Winegard concluded, therefore, that the reason for the failure of Tiller's colony prediction in "pure" binary eutectics was that lamellae can continue to subdivide to relieve the concentration gradient in the liquid at even high rates of growth, and thus supercooling and the resultant cellular solidification front cannot develop. This argument should also hold for the three constituent ionic compound eutectics of the present study.

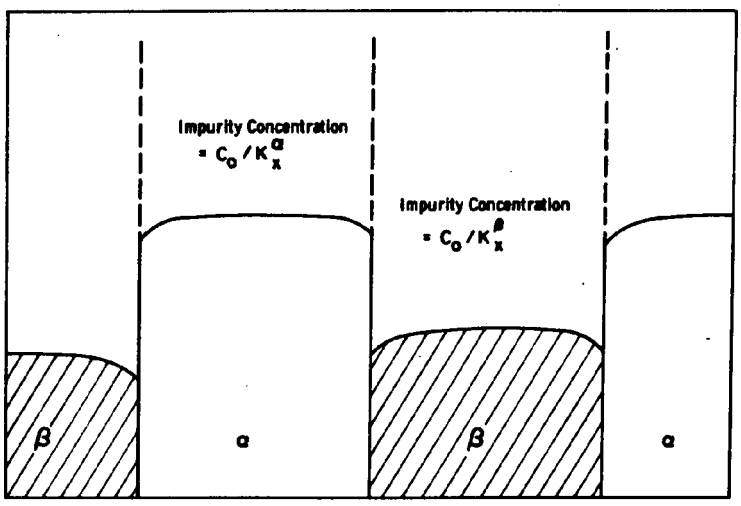
The effects of growth conditions, colony formation and impurities on the micromorphology of the individual phases in the eutectic microstructure have been the topic of recent intensive investigations.[42, 43, 44] Both rod-like and lamellar dispersions of the two eutectic phases have been observed in many different metallic eutectics. In fact, both morphologies have been observed in the same alloy, with intermediate regions suggesting that under certain conditions the lamellae broke down into the rod structure.[17]

Hunt and Chilton[45] proved that metal eutectic systems such as Pb-Cd, Sn-Cd, Cd-Zn and Sn-Zn, which had

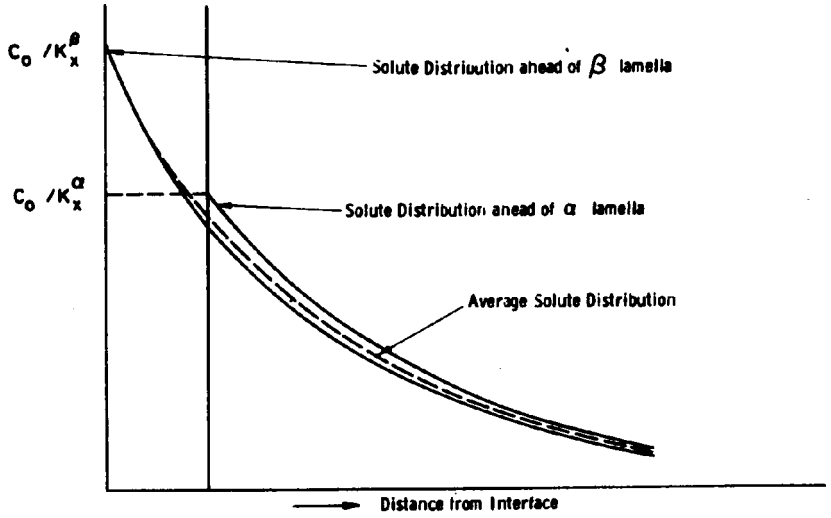
previously been observed to form rod-like microstructures, could be grown with a completely lamellar phase morphology at all growth rates if the alloys were zone-refined to higher purities. They further showed that the lamellar structure could be forced to break down into rods if a eutectic grain were grown around an obstacle so the solidification interface would curve in a direction normal to the lamellar interface. Rods formed in this way in zone-refined alloys did not extend significantly beyond the disturbed region, however. Solidification front curvature which altered the lamellar growth direction in the plane of the lamellae did not cause the lamellae-to-rod transformation. They concluded that the rod-like areas in the colony boundaries of impure eutectics were due to the curvature of the colony solidification front. Subsequent work by Chadwick[37] has indicated that there is probably another mechanism of rod formation. Chadwick has applied the constitutional supercooling mechanism developed to explain the cellular solidification front formed in impure single phase and binary eutectic alloys to the formation of rod-like morphology. Brady[13] had previously proposed that the phase with the highest surface tension, which was also supposed to be of the smallest volume fraction, would form globules or rods to minimize interphase surface area. Hunt and Chilton[45] and Chadwick[37] had also shown that interphase surface area would be minimized by transforming from the lamellar to rod structure at phase volume ratios greater

than about 2:1. However, it appears that this is a minor effect since eutectics with phase volume ratios up to 12:1 have been shown to prefer the lamellar morphology.

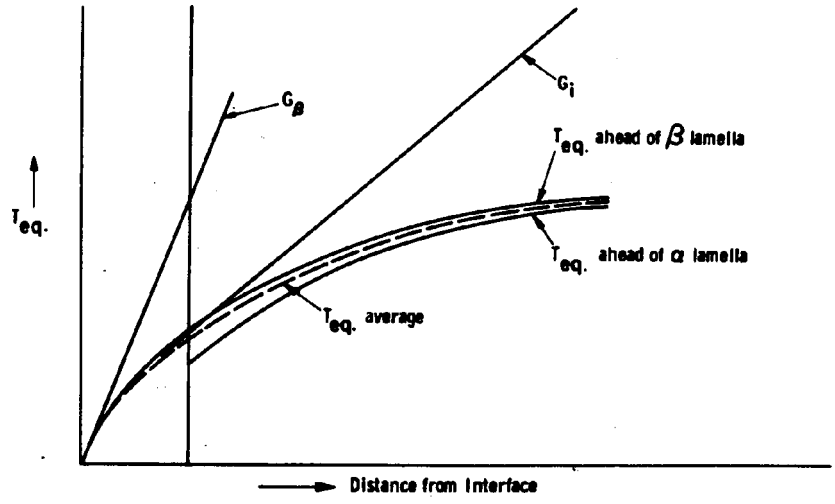
The mechanism proposed by Chadwick to explain the lamella-to-rod transition is based on the assumption that present in the eutectic is an impurity, x, which has distribution coefficients k_x^α and k_x^β in the two phases. Assuming that $k_x^\beta < k_x^\alpha < 1$, at a steady growth rate the β phase will reject more impurity on solidification than the α phase. The excess solute, x, built up ahead of the β lamellae, will then lower the equilibrium freezing point of the liquid in contact with the β phase, thus causing the β lamellae to grow a finite distance behind the α lamellae (Figure 2a). Experimental support for the hypothesis of a leading phase has been recently presented by Davies.[44] The rejected solute can never distribute itself evenly across the interface at even the slowest growth rates since the β phase will always reject more solute than the α phase. This will lead to the solute distribution in the liquid shown schematically in Figure 2b and equilibrium freezing temperatures in the liquid shown schematically in Figure 2c after Chadwick.[36] The critical temperature gradient below which long range constitutional supercooling will occur ahead of the solidification interface is shown by tangent G_i. The steeper temperature gradient, G_β represents the limiting value for local constitutional supercooling ahead of the β lamellae. Thus, as the temperature gradient is



(a) Profile of a lamellar eutectic interface in the presence of an impurity element where $k_x^{\alpha} > k_x^{\beta}$.



(b) Composition of the liquid ahead of the interface of (a).



(c) Equilibrium freezing temperatures of the liquid ahead of the interface of (a).

Figure 2. Impurity effects in liquid ahead of solidifying lamellar eutectic after Chadwick.[36]

decreased below G_β, any random protrusions of the lamellar β phase will be stabilized, just as the long range supercooling stabilizes the cellular colony interface. The stabilized β phase protrusion will then reject the α component atoms radially and cause bridging of the more advanced α lamellae around the β protrusion to give the rod-like β morphology in an α matrix. For temperature gradients between G_i and G_β, the β rods can be stabilized in an overall planar growth front without the existence of a cellular colony structure. At temperature gradients less than G_i, long range supercooling will stabilize the cellular colony structure while, due to local supercooling, the rod-like structure remains. Chadwick has further hypothesized that the reason for the tendency of otherwise lamellar eutectics to break down at colony boundaries into the rod form is that the balance of the distribution coefficients of the two phases for impurity, x, changes at higher concentrations of x to give $k_x^\beta = k_x^\alpha = k_i$ at lower x concentrations. Thus, when the cellular colony structure stabilizes and begins rejecting more impurity to the cell boundaries, the resultant change in distribution coefficients could permit local supercooling and thus stabilize the rod-like β phase. The geometric effect of increased cell curvature at the colony boundary proposed by Hunt and Chilton also probably contributes to the lamellar breakdown, but the relative importance of the two effects cannot yet be estimated.

Other microstructural features have been observed in continuous eutectics, primarily as perturbations or faults in the previously described hierarchy of grains, colonies and phases. Kraft and Albright[43] noted "lamellar faults" analogous to edge dislocations caused by the presence of extra lamellae on one side of a fault line. Yue[42] has observed a lamellar tilt boundary analogous to low angle boundaries described as linear arrays of edge dislocations in single phase solids. Yue attributes this structure to a shallow indentation in the solidification front which will increase in depth, and thus in tilt angle, with increasing growth rate.

It has further been noted by Kraft and Albright[43] that the microstructural appearance of binary eutectic ingots tends to be divided into three zones: at the beginning, center and end of a length of unidirectionally solidified material. The first region contains a relatively disordered array of fairly isotropic eutectic grains caused by many initial nuclei. As growth continues into the center of the ingot, those nuclei which are favorably oriented tend to elongate, and a few dominant grains will normally persist until another disordered region is reached at the end of the ingot. If a colony substructure is present, this too will be elongated in the growth direction, and of course the rods or lamellae of each phase grow parallel to the direction of solidification except where locally perturbed. The disordered region at the end of the ingot is

due to the entrapment of all the impurities rejected in previous solidification which have a very strong disordering effect at all levels of the microstructure.

Virtually all the research discussed above has been conducted on two component metallic eutectics. An original objective of this study was to determine whether two and three component ionic compound eutectics would behave similarly to two component metallic eutectics. However, prior to the completion of this study, Loxham and Hellawell[20] published photomicrographs of rod and lamellar microstructures in unidirectionally solidified, two component alkali halide eutectics. Subsequently, Penfold and Hellawell[22] have reported that these same alkali halide eutectics (LiF-NaF and NaCl-NaF) exhibited a dependence of interlamellar spacing on growth rate and formation of a colony structure caused by impurities similar to metallic two component eutectics. Truelove and Hellawell[23] indicated that all the alkali halide eutectics they studied exhibited a (111) interface coincidence between the phases in lamellar microstructures.

C. Crystallographic Relationships

Probably both nucleation and growth are important in determining the possible and preferred interfacial orientations and growth directions in binary eutectics. It seems natural to describe the process of solidification of a eutectic as follows:

1. Formation of a nucleus of phase A of sufficient size to continue growth and resultant depletion of its surroundings of phase A ions.

2. The resultant increase in concentration of phase B ions around the phase A nucleus, leading to heterogeneous nucleation of solid phase B on the phase A nucleus at preferential sites or on preferred planes.

3. Growth of the two phases in directions governed by:

a. thermal diffusion gradients,
b. concentration gradients,
c. preferred growth directions of the nucleating and/or leading phase, and
d. interfacial surface energy minimization.

The factors involved are probably similar to, if not the same as, those in oriented overgrowth from a liquid or vapor phase on a solid substrate. The regular forms of the phase particles in the lamellar eutectics have led investigators from the beginning to assume that the interfaces between phases represent low index crystallographic planes. It would then follow, by analogy with epitaxial growth, that this is the result of nucleation of one phase by the other from a plate-like nucleus and resultant growth of the lamellae in preferred crystallographic directions parallel to the lamellar interface. Tammann[46] first proposed that the growth occurred normal to the lamellar interface with progressive build up of alternate plates of each phase by renucleation on the previous phase lamellae. Rosenhain and Tucker[34] assumed that dendrites of one phase formed and

that the second phase solidified in the interstices of the first phase at a later time. Vogel[18] was the first to propose simultaneous crystallization of the two phases in the growth direction, but he proposed a polygonal prism rather than lamellae as the phase form. Straumanis and Brakss[47] experimentally verified that the correct growth mechanism was by simultaneous edgewise growth of the lamellar phases in the direction of heat flow. Several mathematical models based on numerical solutions of the thermal and mass diffusion equations involved in eutectoid growth have been proposed, involving simplified assumptions and boundary conditions.[48, 49] These models have been extended to eutectics by Tiller,[50] Li and Weart,[51] and Jackson and Chalmers.[17] All involve the assumption of an undercooling or energy absorption caused by the formation of the interphase boundary in the eutectic solid. Thus, from the beginning, it has seemed natural to assume that nucleation and growth would result in certain preferred crystallographic orientations and bounding planes for the lamellar eutectic phases, whether a mechanistic or thermodynamic viewpoint was taken.

Brady[13] gave the first evidence that the orientation of the crystal structure of eutectic phases might be constant. He presented four types of evidence: (1) homogeneity of surface etching, (2) euhedral form of many discontinuous phases, (3) continuity of slip bands as found by Ewing and Rosenhain, and (4) uniformity of polarization color in naturally occurring nonmetallic eutectics of quartz-

feldspars. Since the utilization of x-ray diffraction techniques for crystal orientation, many studies have been performed which have for the most part verified the fact that low index planes and directions of both phases of binary lamellar eutectics are orthogonally related to lamellae interfaces and growth directions. However, there has not always been agreement among different experimenters as to precisely what the orientations were for a particular system. This is not to be completely unexpected, however, since studies of heterogeneous nucleation have shown many inconsistencies, due to impurity effects and also due to the fact that more than one crystallographic orientation can be nucleated in a single system.

Sundquist and Mondolfo have utilized the finely subdivided liquid droplet technique developed by Turnbull and his associates to study heterogeneous nucleation of one phase by the other in binary metallic eutectics in the absence of impurity effects.[52] They first studied the undercooling possible in hypo- and hypereutectic alloys by observing the freezing of finely divided alloy drops in a hot stage microscope. The undercoolings observed verified the findings of Lamplough and Scott[19] in a study of metallic eutectics in 1914 that only one of the primary phases in a binary system was effective in nucleating the eutectic, if any effect was observed at all. Sundquist, et al[52] further concluded that the relative solid-liquid interfacial energies of the catalyst and nucleated solid is the important factor in

determining nucleation effectiveness, and not lattice misfit as was formerly believed. They were thus able to relate the nucleating power of metals to their gram-atomic solid-liquid interfacial energies, crystal structures, entropies of fusion, and for the same crystal structures, to their melting point. For the metallic and intermetallic systems studied they concluded that phases with higher solid-liquid interfacial energies, entropies of fusion and melting points would readily nucleate, but not be nucleated by phases of lower values with the same crystal structure. They further concluded that phases with more "complex" (directionally bonded) crystal structures should tend to nucleate those of simpler structure but not the reverse. They explain the fact that the relative solid-liquid interfacial energies for anisotropic crystal structure phases do not always indicate their relative nucleating power by the contention that their measured interfacial surface energies are only average values due to the directional anisotropy of this property. Sundquist and Mondolfo[53] extended this work in a combined study of undercooling and relative crystallographic phase orientations of self-nucleated eutectic alloys of lead. They concluded that a multiplicity of orientation relationships can occur, but they will usually tend to be between low index planes with low linear lattice misfits in simple crystal structures. However, the lowest possible misfit was not the most frequent orientation relationship; therefore, they concluded that other

factors were involved. Good symmetry relationships between mating planes seemed to be a second important factor, corresponding to the findings of previous experiments on epitaxial overgrowth.[54] However, the amount of undercooling observed did not seem to vary with orientation relationships or lattice disregistries.

The above findings indicate that the nucleation process probably does not constrain eutectics to only one possible set of crystallographic mating planes between the phases as was previously assumed. However, virtually all the eutectic phase orientation results reported to date have proposed a single set of relationships for a particular system. This situation may have occurred because of the general assumption that a single equilibrium relationship should exist and a reluctance to accept and report contradictory results. It should be noted, however, that different workers have reported different orientation results for the same systems.[17]

Additional constraints due to the unidirectional growth process have not yet been studied in as great a detail as the nucleation effect on orientation, but they could also contribute to the reduction of the number of possible crystallographic orientations between lamellar eutectic phases. Kraft and Albright[43] have indeed shown that in the Al-$CuAl_2$ system a preferred crystallographic orientation is developed gradually between the phases as the lamellae grow along the length of the ingot. Cooksey

et al[21] have observed a similar tendency toward a preferred orientation during unidirectional eutectic growth which they ascribe to a process of repeated nucleation resulting from larger undercoolings which exist at the non-equilibrium freezing interfaces. Kraft has proposed a general rule for predicting the lowest energy or equilibrium form for lamellar eutectics based on his detailed analyses of the Al-$CuAl_2$ and Mg-Mg_2Sn systems:

> "The unit cells in each phase tend to assume an orientation relative to one another such that the interface between them is parallel to actual physical planes or puckered planes of atoms of wide spacing and nearly equal atomic densities."[55]

He contends that such configurations would minimize the solid-solid interfacial energy, which would in turn minimize the depth of the interlamellar groove at the solid-liquid solidification interface, according to the theory of Tiller. This, in turn, would facilitate lateral diffusion in the liquid by forming a more planar solidification front.

The growth direction in a normal eutectic, in which the lamellae grow normal to the solidification front, must be one which lies in the crystallographic plane of the lamellar interface. It is not so clear, however, why one direction seems to be preferred to another in such a plane. Barrett has summarized the available data on the preferred growth directions of columnar grains in single phase metal castings.[56] For face-centered cubic and body-centered cubic metals [100] was the preferred growth direction.

Edmunds[57] has explained these results on the basis that the natural crystal faces that tend to develop are the planes of maximum atomic density, {111} in face-centered cubic, {110} in body-centered cubic, and (0001) + $\{2\bar{1}\bar{1}0\}$ in close-packed hexagonal. The maximum growth velocity should thus be in the direction of the maximum dimension of the solid formed by these bounding surfaces. This would be the [100] direction for the octahedra and dodecahedra of cubic crystals and a direction dependent on the c/a ratio for close-packed hexagonals. Kraft has used this theory to explain the preference of the Al-$CuAl_2$ eutectic lamellae for a [112] growth direction by postulating that the constraint of one opposing pair of (111) planes as interlamellar boundaries would indeed stabilize the [112] direction as the maximum dimension of an octahedra parallel to these two planes (Figure 3).[58] Further restriction of charge balance requirements will, however, probably be involved in the application of this theory to three component ionic compound eutectics.

D. Property Relationships

This section will review the pertinent literature on the physical properties studied in this investigation under the following headings: hardness, deformation and fracture and thermal expansion.

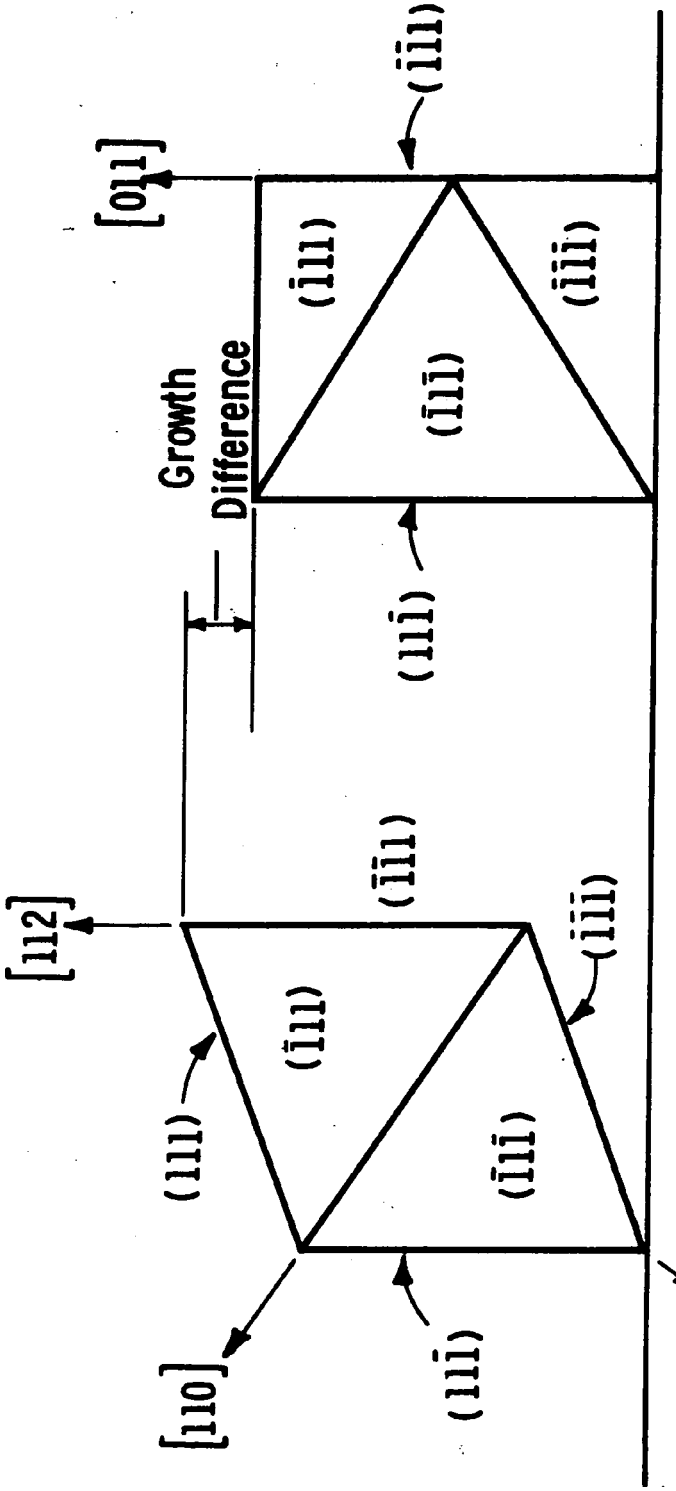


Figure 3. Growth of octahedra under restricted conditions. $(11\bar{1})$ and $(\bar{1}\bar{1}1)$ perpendicular to paper and to horizontal line at bottom of figure. After Kraft.[58]

1. HARDNESS

The hardness tests used in this study were Knoop and Vickers micro-indentation types applied by a Tukon hardness machine. This review will therefore be limited to indentation hardness and primarily to the meaning of this type of hardness as applied to ceramic or ionic materials. The indentation hardness technique has been used extensively in the characterization of polycrystalline materials, and a vast literature has resulted which has been summarized in several books.[59, 60, 61, 62] Much less work has been reported on hardness and hardness variations in single crystals. Perhaps this is because even the most isotropic, highly symmetric single crystals show marked variations in hardness with respect to shape and orientation of the indentation, thus requiring much more detailed analysis to produce meaningful results. Recent use has been made of Vickers and Knoop indentation for the study of plastic deformation and fracture in single crystals of various materials, including MgO,[63] MnS,[64] Al,[65] Mg,[66] Zn[66] and quartz.[67]

Greater hardness has generally been empirically associated with a greater strength in materials, and many attempts have been made to establish useful correlations between hardness and other measures of the resistance of a solid to deformation. This is because hardness is a simple value to measure, and the testing can usually be done in a nondestructive way in very small samples. Unfortunately,

most hardness tests probably measure some complex combination of elastic properties, tensile or compressive strength and plastic flow properties such as yield stress and capacity to work harden.[68] In metals the yield strength is usually much smaller than the elastic moduli,[69] and therefore their hardness values are principally a function of their plastic deformation or compressive stress-strain curve.[61] In the covalent and ionic materials, however, elastic and fracture behavior become important in determining the measured hardness in addition to plastic characteristics.[70] Empirical correlations have also been observed between hardness and (1) melting point,[71, 72] (2) surface energy of the indented materials,[73, 74, 75, 88] and (3) the energy needed to create new surfaces at fractures.[76]

Westbrook[77] reported a linear relationships between the yield stress of NaCl-type crystals and their Vickers indentation hardness of the form

$$Y.S. = H_V/35,$$

where Y.S. is the yield stress in kg/mm^2 and H_V is the Vickers hardness in kg/mm^2. Gilman has reported a similar linear relationship between microhardness and elastic modulus of other NaCl-type crystals.[78] Thus, microhardness can be used in these materials to estimate these more fundamental properties.

Moore studied the change in hardness of NaCl with temperature from room temperature to 1075°F.[79] Chao, et al[80] have measured the indentation hardness of MnS versus

temperature from room temperature to 1000°C.

In recent years attempts have been made to study modes of plastic deformation of ceramic single crystals around various kinds of indentations.[63] Keh innovated the use of etch pit techniques to study deformation patterns around indentations in MgO at various temperatures.[63] This technique had been used previously to study etch pit rosettes caused by hard particle impacts on cleaved surfaces of LiF[81] and MgO.[82] Chao et al studied indentation rosettes and cleavage in MnS single crystals.[64]

Chao et al also reported work on the variation of the hardness of single crystal and polycrystalline MnS with temperature and the variation of hardness across the phase diagram of the MnS-FeS system.[80] They found only slight changes in hardness of the MnS phase as the iron content in solution was increased until FeS was precipitated as a Widmanstätten phase on the {111} planes of MnS. Then the rate of increase of hardness was greater at all temperatures up to 1000°C as the FeS content increased. They were unable to measure the hardness of FeS alone due to its extreme brittleness, but they concluded that it was harder than the MnS phase.

2. DEFORMATION AND FRACTURE

The mechanical properties of ceramic materials manifested in their deformation and fracture behavior have only recently been intensively studied.[63, 64, 81, 82] This work

has to a great extent grown out of, and followed the same course as, the efforts of physical metallurgists to relate the complex behavior of polycrystalline metals to the atomistic mechanisms of slip and fracture deduced from single crystal studies. Since the realization of the great importance of mechanical constraints at grain boundaries on the operation of these mechanisms in polycrystals[83, 84, 85] and the formulation by Taylor[86] of the theory of multiple slip to explain polycrystalline behavior, a great deal of progress has been made in relating single crystal properties to those of complex polycrystals in metals, and more recently, in ceramics. A most valuable experimental means of bridging the gap between single crystals and random polycrystals has been the study of deformation and fracture in single-phase bicrystals with various relative crystal orientations across the single grain boundary involved. It is proposed that the two phase, crystallographically and microstructurally oriented eutectic polycrystals grown in this study can provide an additional bridge between the studies of bicrystals and true multi-phase random polycrystals. Therefore, this review will include a discussion of the known behavior of single crystals, polycrystalline aggregates and oriented bicrystals, insofar as they might apply to the understanding of eutectic properties.

a. Single Crystals

Plastic deformation in metallic single crystals

generally occurs by slip or twinning. Twinning has not been observed in NaCl structure crystals; therefore, this review will be limited to the slip mechanism. Slip occurs by the relative movement of planes of atoms or ions on a slip plane, {hkl}, by means of the propagation of linear defects or dislocations in a slip direction <hkl>. Many investigators have shown that there is a critical resolved shear stress necessary to cause slip to occur in a particular plane and direction which is not sensitive to stress components normal to the glide plane and direction.

Gilman's[78] review of the plastic deformation of NaCl-type crystals indicates that, except for the highly polarizable PbS and PbTe, all are reported to have primary <110>{110} glide with a secondary <110>{100} glide in some systems. A <110>{111} glide has been reported by Buerger[87] in sodium halides. Keh[63] found only the <110>{110} glide system in MgO. However, Chao et al[64] found a secondary <110>{111} glide system in addition to the primary <110>{110} glide system in MnS.

Fracture occurs most easily by cleavage on {100} planes in all NaCl-type crystals.[78] A phenomenological explanation for this has been proposed by Kuznetsov[88] based on the observation that any shear displacement of one {100} plane over another would cause very high like-ion coulombic repulsions between the planes because of the arrangement of alternating positive and negative ions on these planes. In fact, Kuznetsov contends that even when

cleavage is constrained to the {110} or {111} planes, the surfaces of the cleavage planes are made up of tiny {100} facets. Gilman[78] and Keh,[63] however, have reported secondary cleavage on {110} planes. Keh attributed the {110} cleavage cracks around indentations to the interactions of dislocations moving on {110} planes inclined 45° to the {100} indentation surface.

Chao et al[64] observed that grain boundary fracture occurred easily in polycrystalline MnS when MnO was present as an impurity segregated in the grain boundaries. He also observed that although {100} cleavage was primary in the crushing of MnS, the {110} fracture was primary around indentations. It was deduced that this fracture was due to the interaction of $(01\bar{1})$ and $(10\bar{1})$ slip near the (001) indented surface. A minor amount of fracture was observed on {110} planes lying 90° to the indented (001) surface caused by the interactions of {111} slip planes.

b. Polycrystals

The plastic deformation of random isotropic polycrystalline aggregates has been studied extensively.[89, 90, 91] Recently the effect of the variation of grain size in such aggregates versus the yield point of flow stress has been investigated.[92, 93, 89] Early suggestions as to this effect were made by Kochendorfer,[94] Nabarro[95] and Kocks.[91] Armstrong et al[89] have summarized the work on yield point versus grain size in metals in which several systems obey the relation,

$$\sigma_{lyp} = \sigma_o + k\ell^{-1/2},$$

where σ_{lyp} is the lower yield stress, σ_o and k are constants and ℓ is the grain diameter. They suggest that a similar relationship should hold even in materials which do not exhibit yield point behavior for flow stress at constant strain, σ_f, as follows:

$$\sigma_f = \sigma_o + k\ell^{-1/2}.$$

The constant σ_o is the stress a slip band could sustain if there were no effective resistance to its passage at the grain boundary. This would equal the friction resisting the movement of an isolated dislocation on the slip plane in the simplest case. The relationship involving the grain diameter, ℓ, is derived directly from the analysis by Eshelby et al[96] that the stress concentration factor a short distance, r, ahead of a slip band of length, ℓ, is $(1/4r)^{1/2}$, assuming similarity between a slip band and a crack in relieving stress. They attribute this behavior to the grain boundary resistance to propagation of slip bands between grains which reaches a limiting value proportional to $\ell^{-1/2}$ when plastic deformation is induced at the end of the slip band. They[89] also proposed for the constant of the previous equation the equation

$$k = m^2\tau_c r^{1/2},$$

in which m is an orientation factor dependent on the crystal structure and polycrystalline constraints, τ_c is the shear stress required to operate a source or force a dislocation across the boundary, and r is the distance ahead of

the slip band at which the maximum shear is generated. These factors determine the sensitivity of flow stress to grain size, and they in turn are determined by the number of possible slip systems, the shear modulus, any dislocation locking, and possibly by the dislocation density, according to Armstrong.[89] Thus, it is claimed that this relationship explains the principal differences in the sensitivity of flow stress to grain size observed in various alloys. For instance, the smaller the number of slip systems, the greater is m, since poorly oriented slip planes must operate. This would be significant in the case of NaCl-type structures since the possible slip systems are greatly reduced compared with metallic crystals due to coulombic restraints. Furthermore, since the shear modulus, μ, is a principal factor in determining the shear stress, τ_c, it is certain that the value of k will be different when propagating from MnO to MnS compared with the reverse case since MnO and MnS have different shear moduli. In general it would appear that, it this analysis developed for metals is applicable to ceramics, there should be a strong dependence of flow stress, and therefore of hardness, on grain size in the MnO-MnS system.

Taylor's analysis[86] of plastic deformation of polycrystals was based on the assumption of homogeneous strain throughout the aggregate, and it led to the deduction that at least five independent slip systems would have to operate in the general grain to permit all the randomly

oriented grains to conform to the overall shape change. He then used a "least work" concept to propose that the specific combination of five slip systems that would operate for a particular imposed strain in a given grain would be the one which could satisfy the shape change with the minimum total shear. It will later become apparent that the number of independent slip systems required is reduced for the general bicrystal and even further reduced for the "symmetric" bicrystal and eutectic lamellae due to the fewer constraints involved.

Bishop and Hill[97] have mathematically formulated Taylor's hypotheses and assumptions and applied them in detail to the face-centered cubic crystal structure.

c. Bicrystals

Considerable attention has been paid recently to the plastic deformation and fracture of single phase bicrystals with various relative orientations of the two crystals.[83, 84, 98, 99, 100] Since the lamellar two phase eutectics in this study are probably more like an array of bicrystals with a constant low misorientation between the crystals than like a random polycrystalline aggregate, it is suggested that the results of these studies are pertinent to the analysis of the mechanical behavior of the eutectic. This is especially true since MnO and MnS phases have the same NaCl-type crystal structure, differing only in unit cell size. Of course the physical properties of MnO and MnS phases are different in terms of elastic moduli,

hardness and flow stress, but their plastic deformation mechanisms are quite similar.

Unfortunately most of the testing of bicrystals reported to date has been in simple tension, which is much easier to analyze than indentation hardness.

Livingston and Chalmers[98] have applied a form of Taylor's polyslip plasticity theory to the tensile deformation of "isoaxial" (both crystals having a common crystal direction parallel to the tension axis) bicrystals of aluminum. Using a macroscopic continuum model of a bicrystal (Figure 4), they contend that for the two grains to remain contiguous, the compatibility conditions for the strains E_{ij} across the boundary must hold; i.e.,

$$E^A_{zz} = E^B_{zz},\ E^A_{xx} = E^B_{xx},\ E^A_{xz} = E^B_{xz}.$$

If the above conditions apply to grains A and B when strained separately, they are considered compatible in terms of the macroscopic average strains at the grain boundary. In single phase bicrystals this implies only mirror image crystallographic orientations across the grain boundary, but due to differences in elastic moduli, critical shear stresses and lattice parameters, this is not sufficient when a bicrystal of two different materials is considered, even when the crystal structures are the same. They use a microscopic model in which they assume that a pile up of dislocations on one side of a bicrystal grain boundary imposes a pure shear stress across the boundary. They then resolve this shear stress by standard tensor

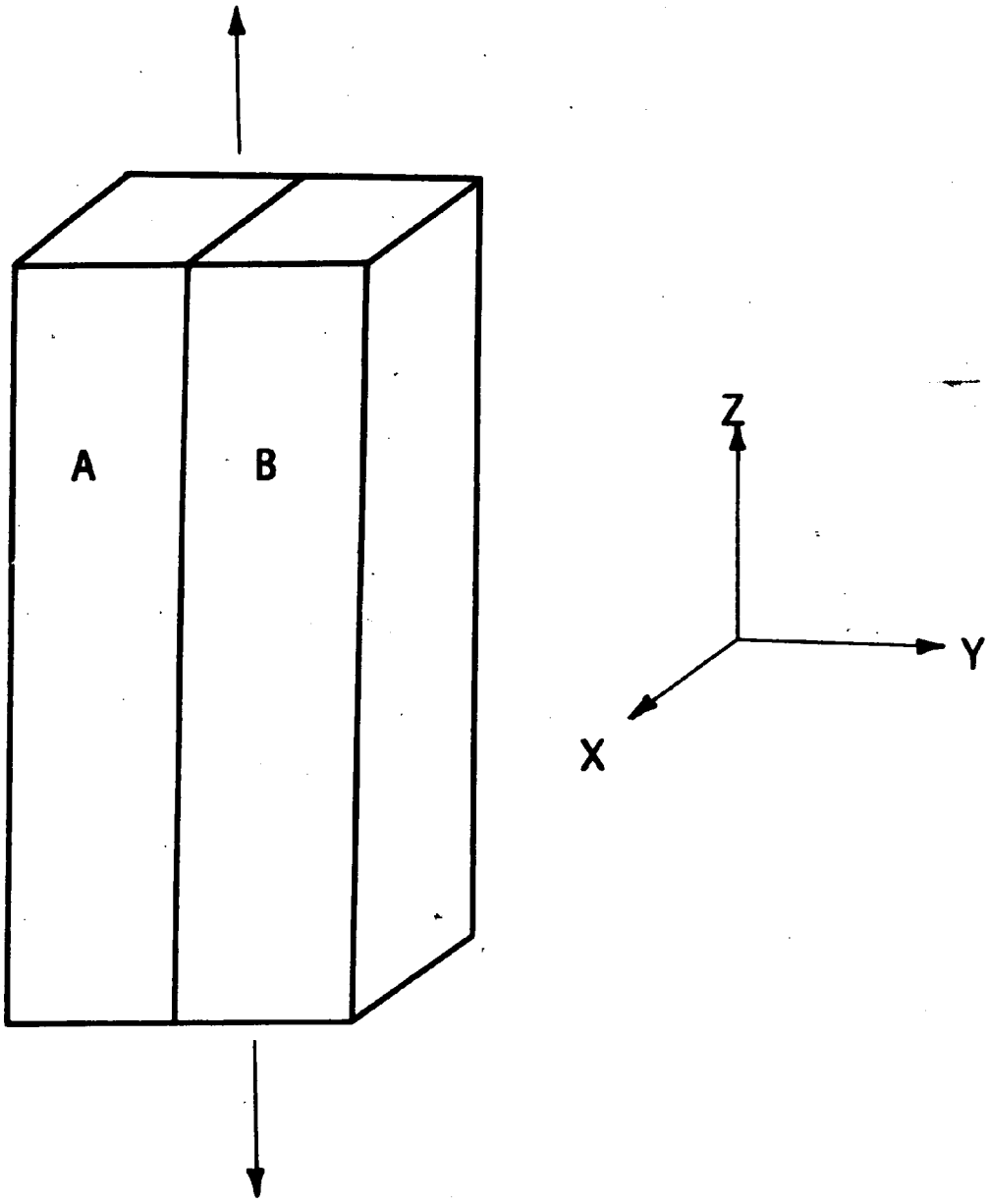


Figure 4. Bicrystal tensile specimen with longitudinal boundary. After Livingston and Chalmers.[98]

transformation on the various slip systems on the other side of the boundary to predict which such system will operate. They of course predict that the system in the second crystal with the highest resolved shear stress, caused by the dislocation pile up, will operate. They use Taylor's analysis to show that for the general, incompatible isoaxial bicrystal to deform in tension and still maintain macroscopic continuity at the grain boundary, the operation of four independent slip systems in the two crystals will be required, distributed with three in one crystal and one in the other or with two in each. Recent investigations by Fleischer and Backofen[101] verify that compatible, isoaxial bicrystals do give stress-strain curves coinciding with those of single crystals and that slip lines occur for the primary slip system only. Several investigators, however, have found that the rate of work hardening, $\frac{d\sigma}{d\epsilon}$, is greater in isoaxial, non-compatible bicrystals than in single crystals due to the operation of more than one slip system adjacent to the grain boundary.[102, 103] Fleischer and Backofen[101] also noted that a size effect existed since bicrystals with a small dimension normal to the grain boundary, where duplex slip could extend over the entire crystal, exhibited higher work-hardening rates than wider bicrystals. Elbaum[104] further demonstrated that for isoaxial, incompatible tri- and quadrucrystals, progressively higher strain hardening rates occurred, with more complex slip patterns than in bicrystals.

Dorn and Mote[83] have summarized the findings on metallic bicrystals:

> 1. "The grain boundary per se offers no resistance to plastic deformation. Isoaxial bicrystals having compatible orientations have the same stress-strain curves as similarly oriented single crystals.
>
> 2. "The yield strength of incompatible as well as compatible isoaxial bicrystals is identical with that for similarly oriented single crystals. Thus, the differences in orientation of each grain of incompatible isoaxial bicrystals does not increase the stress for initiation of plastic deformation.
>
> 3. "Incompatible isoaxial bicrystals strain-harden at a much higher rate than similarly oriented single crystals. The increase in the rate of strain hardening can be ascribed principally to the operation of multiple slip (at least four systems) in the vicinity of the grain boundary, a condition which is imposed by the necessity of satisfying the compatibility relationships in the grain boundary region.
>
> 4. "Multiple slip is most prevalent in the immediate vicinity of the grain boundary of bicrystals and multicrystals. Consequently, the rate of strain hardening increases as the grain size of multicrystals decreases.
>
> 5. "Multiple slip occurs almost exclusively on the usual slip systems found operative in single crystals, but occasionally new slip systems become operative."

Studies on MgO bicrystals having the same NaCl structure as MnO and MnS have been performed by Johnston, Stokes and Li.[84] They examined the effect of slip propagating from a line source into bicrystal boundaries with a range of tilt and twist misorientations on the compression side of a bend specimen. They were able to distinguish three processes occurring at the boundary in three ranges of

misorientation:

> 1. "The shear stress concentration ahead of the pile-up nucleates dislocation loops and thereby slip bands in the {110} planes of the adjacent grain. This relaxes the stress concentration and cracks do not form. This process occurs preferentially when the slip planes on either side of the boundary are almost coplanar.
>
> 2. "The tensile stress concentration beneath the blocked slip band nucleates a {110} transgranular crack in the adjacent grain. Under macroscopic compression, the cleavage crack decelerates and generates dislocation loops which subsequently develop into slip bands in the adjacent grain. This process occurs when the misorientation is such that the resolved tensile stress concentration due to the pile-up exceeds the cohesive strength of the {110} plane before the resolved shear stress concentration exceeds the theoretical shear strength to nucleate slip.
>
> 3. "The tensile stress concentration beneath the blocked slip band nucleates an intergranular crack. Under macroscopic compression the crack is stable. This process occurs when the resolved tensile stress concentration exceeds the intergranular strength before it exceeds the cohesive strength of the cleavage plane. As the misorientation changes from small to medium to large, then the predominant, though not exclusive, process changes from (1) to (2) to (3)."

These results indicate that at the low misorientations which exist between the eutectic phases in the systems of this study there is little possibility of intergranular or even transgranular cracks being created by the pile up of dislocations. Westwood,[105] however, concluded that cracks may be nucleated at a low angle grain boundary in MgO bicrystals through the superposition of tensile stress fields caused by two dislocation pile ups occurring within a range of one or two microns of one another on

either side of a bicrystal boundary.

Day and Stokes[90] have reported a great deal of work on MgO in single crystal, bicrystal and polycrystal forms Their conclusions can be summarized as follows:

1. MgO crystals are plastic only in the presence of suitably oriented mobile slip dislocation sources.

2. In the absence of slip sources bicrystals are strong and elastic but are weak and brittle in tension when mobile sources are present because of crack nucleation caused when the slip bands are blocked by the grain boundary.

3. Only simple tilt boundaries of a few degrees misorientation can relax the stress concentration by transfer of slip from one grain to another.

4. The increased ductility of MgO above 1700°C is due to three factors:

a. increased ability of {110}<110> slip systems to interpenetrate and operate concurrently.

b. increased number of slip planes on which the <110> slip vector can operate. Factors (a) and (b) combine to permit sufficient slip systems to operate in a given volume of polycrystalline MgO to satisfy the von Mises criterion.

c. polygonization and recrystallization processes which relieve internal local stresses can operate.

5. Pores act as stress raisers to cause crack

nucleation and therefore more brittle behavior in less than 100% dense MgO.

3. THERMAL EXPANSION

This section will review the pertinent literature on (1) the thermal expansion of NaCl structure crystals and (2) the thermal expansion of two phase composites.

Austin[106] has reviewed the fundamental significance of thermal expansion and its relationships to crystal structure in nonmetallic crystals. He concluded that the thermal expansion of crystals such as the NaCl types of this study should be isotropic and vary in direction proportion to the melting point or heat of formation in an isomorphous series. Wooster[107] observed that the expansion coefficient for binary compounds with the same cation increased with anion size. Thus, the thermal coefficient of MnS would be expected to be larger than that of MnO.

The thermal expansion coefficients for MnO, FeO and MnS have been reported by Ellefson and Taylor[108] over the range of 100 to 200°K where certain expansion anomalies occur in these materials. The thermal expansion of MnO has been reported by Foex[109] from -120 to 700°K. However, thermal expansion data has not been published for MnS above 200°K.

The apparent thermal expansion of a two phase composite should be some value intermediate between that of the two phases involved according to experiments by Kingery.[110]

Turner[111] and Kerner[112] have formulated mathematical models to predict the thermal expansion of composites when the expansivities and moduli of the individual phases are known.

The microstresses due to thermal expansion differences in multi-phase composites have been discussed in detail by Laszlo[113] and more recently by Kingery.[110] The calculation of these stresses is a matter of balancing the strains imposed by each phase on its neighboring phase particles and the amount of relief of such strains which can occur by the various mechanisms of viscous flow, diffusion, slip and fracture.

Measurement of internal micro-strains by x-ray and other methods has been discussed by Fulrath[114] and Lauchner.[115]

CHAPTER III

EXPERIMENTAL PROCEDURE

A. Sample Preparation

1. RAW MATERIALS

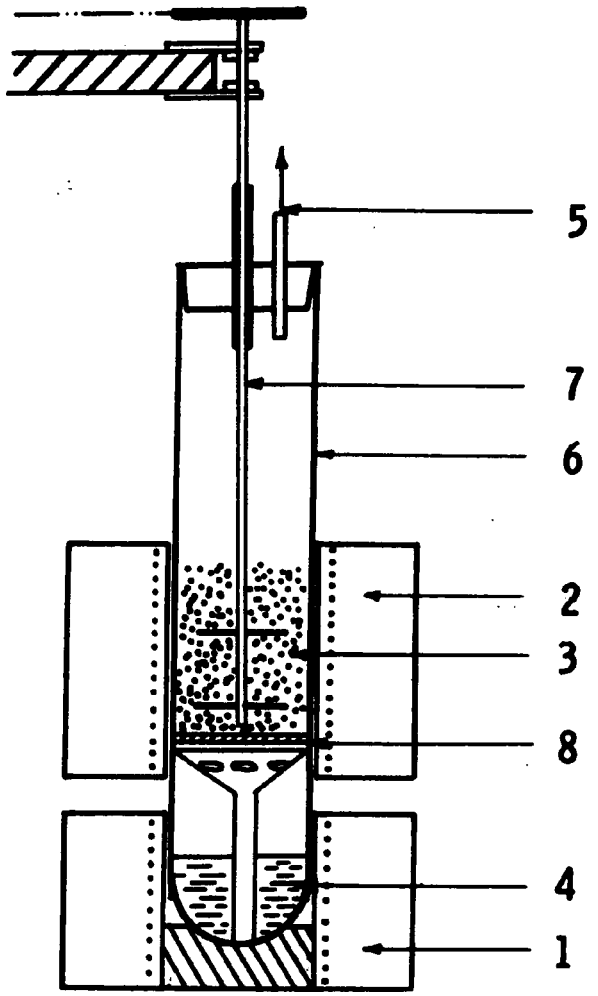
The manganous oxide (MnO) was prepared by reduction of reagent grade manganese dioxide (MnO_2) of 99.9% purity in hydrogen at 950°C. The reaction can be represented by

$$MnO_2 + H_2 \rightarrow MnO + H_2O\uparrow.$$

The manganous sulfide (MnS) was prepared using a technique previously reported by Chao and Van Vlack.[64] This involved the deoxidation of reagent grade manganous sulfate monohydrate powder ($MnSO_4 \cdot H_2O$) of 98.8% purity by sulfur according to the reaction

$$MnSO_4 \cdot H_2O + S_2 \rightarrow MnS + 2SO_2\uparrow + H_2O\uparrow.$$

The sulfur was vaporized at 410°C by a small resistance furnace in the lower part of a vitrified silica tube. The sulfur vapor then reacted with the charge of $MnSO_4$ powder in the upper part of the furnace tube held at 900°C by a second resistance furnace. Mechanical stirring of the $MnSO_4$ powder speeded completion of the reaction. A schematic diagram of the apparatus used is shown in Figure 5, after Chao.[64] The MnS powder was then melted into ingots in an induction furnace using a graphite crucible-susceptor. Neither optical examination nor x-ray powder patterns indicated that phases other than MnS were present. The lattice



1. Lower furnace, 410°C
2. Upper furnace, 900°C
3. $MnSO_4$ charge
4. Liquid sulfur
5. SO_2 exhaust
6. Reaction tube
7. Stirrer
8. Support of graphite felt and porcelain filter to hold charge

Figure 5. MnS purification. Stoichiometric manganese sulfide has been prepared most satisfactorily by the above method.

constant, a_o, for the MnS was checked by calculating a_o's for a series of powder pattern lines and extrapolating the curve obtained to $\theta = 90°$ versus the Nelson-Riley factor, $1/2(\frac{\cos^2\theta}{\sin\theta} + \frac{\cos^2\theta}{\theta})$. The value obtained was 5.223Å compared with 5.225Å reported by Chao,[64] 5.224Å by ASTM,[116] and 5.165 to 5.260Å by Boniszewski and Baker.[117]

Some of the MnS used in this study was zone-refined in a horizontal induction furnace under a purified argon atmosphere with a final pass of one inch per hour as previously described by Chao and Van Vlack.[64]

The iron sulfide (FeS) was prepared by reacting stoichiometric ratios of high purity (99.98%) ferrovac iron wire and U.S.P. grade sulfur to completion in an evacuated and sealed Vycor tube,[64] according to the reaction

$$2Fe + S_2 \rightarrow 2FeS.$$

The iron wire in one end of the tube was held at 880°C and the sulfur liquid in the other end was held at 440°C in a furnace temperature gradient. X-ray powder patterns indicated that the iron was completely reacted and no other phases were present.

All of the other raw materials used in preparation of the five eutectics of this study were reagent grade chemicals with no further preparation and purification. These include reagent grade NaF (99.0%), NaCl (99.9%), NaBr (99.5%), LiF (99.9%), and Fe_2O_3 (99.0%).

2. EUTECTIC INGOTS

The raw materials described above were mixed as

powders in the proper weight ratios as indicated by the phase diagram for each eutectic. The powders were then mixer-milled together in steel canisters containing steel balls in a Spex Mixer-Mill. The eutectic mixtures were then charged into Ferrovac iron crucibles for MnO-MnS and FeO-FeS, and into spectroscopic grade graphite crucibles for NaCl-NaF, NaBr-NaF and LiF-NaF The crucibles were usually 1/4 inch i.d., 1/2 inch o.d., and 18 inches long. An ingot of 1/4 inch o.d. and about 6 inches in length was obtained in all cases if the crucible was charged completely full of eutectic powder.

The general procedure involved completely melting the powder charge by passing the crucible slowly through a silicon carbide resistance or high frequency induction furnace under an argon atmosphere. This initial melting was performed while moving the crucible vertically upward through the furnace. The unidirectional solidification was performed by withdrawing the crucible and its refractory envelope vertically downward from the heating zone of the furnace. In the case of the induction furnace the relative motion of the crucible and heating coil was accomplished by moving the coil instead of the crucible. The induction heating method was very difficult to control, and although it originally appeared to offer advantages over resistance heating, it was eventually abandoned in favor of the apparatus shown in Figure 6. The crucible was transported through the silicon carbide resistance furnace by the drive

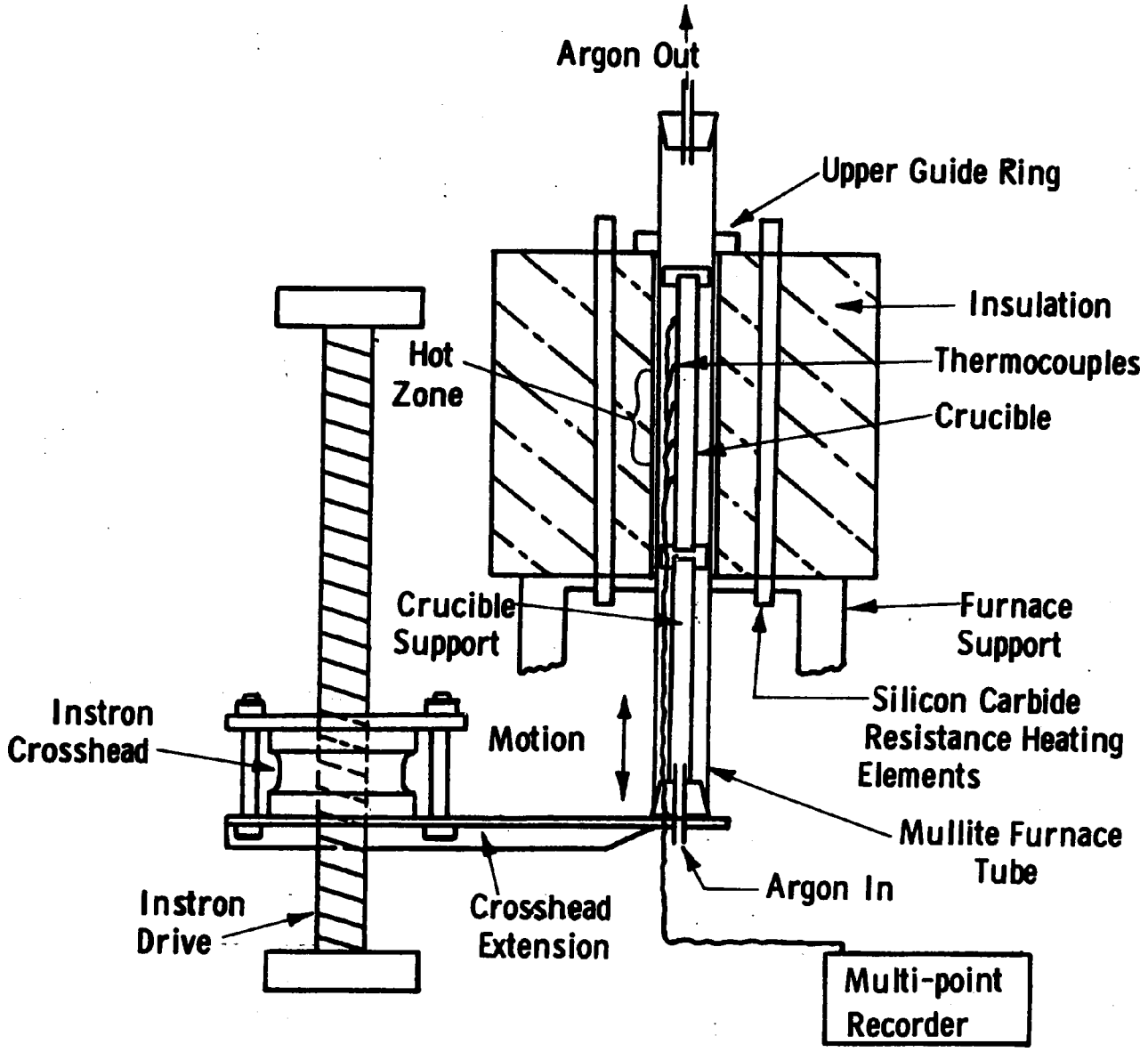


Figure 6. Eutectic unidirectional solidification apparatus.

mechanism of an Instron testing machine permitting synchronous speeds of down to 0.002 inches/min. The actual solidification front speed was not usually equal to the nominal speed of crucible withdrawal due to changes in the temperature profile along the crucible as it was withdrawn from the furnace. Platinum-10% rhodium thermocouples were used to instrument some of the Ferrovac iron crucibles to determine the true rate of movement of the solidification front for correlation with lamellar widths in MnO-MnS ingots.

All the ingots were melted and solidified in open top crucibles except the FeO-FeS eutectic. This ingot was prepared by mixing FeS with the proper amount of reagent grade Fe_2O_3 and sealing the mixed powders in a Ferrovac iron crucible. The crucible was sealed by Heliarc welding a Ferrovac iron plug into its top. The necessary iron to react with the Fe_2O_3 to form the desired FeO was supplied by the iron crucible.

3. SECTIONS

The eutectic ingots were prepared for testing by removing them from their crucibles and cutting out transverse and longitudinal sections. The oxide-sulfide ingots had to be removed by cutting longitudinal slices from the Ferrovac iron crucibles and splitting the crucible slices away from the ingot individually since iron has a higher thermal expansion than oxides and sulfides. The alkali halide ingots could be slipped out of their graphite crucibles very

easily at room temperature since graphite has a lower thermal coefficient of expansion than alkali halides.

High speed, resin-bonded silicon carbide cutting disks 0.010 inch thick were used in sectioning the oxide-sulfide ingots, and a bandsaw was used in sectioning the alkali halide ingots.

In most cases the ingot sections were imbedded in cast polyester resin mounts for polishing and microstructural examination prior to testing.

B. Testing

1. MICROSTRUCTURAL ANALYSIS

The mounted ingot sections were prepared for microstructural analysis by standard metallographic polishing techniques. The oxide-sulfide eutectics were rough polished on increasingly finer silicon carbide polishing papers (from 240 to 600 grit) and then on 8 micron and 1 micron diamond wheels. It was difficult to remove all scratches since small particles of ceramic would occasionally break out of the polished surface at unsupported edges during fine polishing, causing coarse scratches. The alkali halide eutectics were rough polished on 600 grit paper and then fine polished on a silk wheel with Linde B alumina polishing powder in alcohol-water solutions. The polished sections were then examined and photographed on standard reflected light microscopes and metallographs. It was necessary to observe the microstructure on two adjacent

sections at right angles in order to determine the three dimensional form and orientation of the rod-like or lamellar phases.

2. CRYSTALLOGRAPHIC ORIENTATION

The crystallographic orientation of selected regions of the eutectic ingots was determined by back-reflection Laue and Buerger precession transmission x-ray techniques. The NaCl-NaF and NaBr-NaF eutectics gave excellent back-reflection Laue results with well defined spots and low background intensities, permitting unambiguous orientations with respect to growth direction and microstructural orientation. For these eutectics selected regions of uniform lamellar microstructure were chosen at the intersection of two polished surfaces of each ingot for cleavage of an x-ray transmission specimen. A small glass fiber was then cemented to the desired region and a small fragment cleaved out of the ingot with a razor blade under a stereomicroscope. The cleavage zone was photographed before and after cleavage, and the cleavage fragment was photographed from several angles so the orientation of the lamellae with respect to the cleaved and polished surfaces of the fragment and with respect to the glass fiber was recorded.

The cleavage fragment was then mounted on a two-circle goniometer head and optically oriented by means of reflections from its various cleaved and polished surfaces. The goniometer head was then transferred to a Buerger precession x-ray camera made by the Charles Supper Co.

Several low precession angle ($10°\bar{\mu}$) exposures were then made to guide the final precise orientation of the lamellar eutectic fragment with respect to the x-ray beam and film. Then several 0-level precession x-ray exposures were made of the low index crystallographic planes parallel and perpendicular to the eutectic lamellae. All exposures were made on North American Philips Co. x-ray generators using a molybdenum target tube (Serial No. 20168) at 40 kv and 15 ma settings. Exposure times were one-half to two hours for orientation shots and 5 to 20 hours for 0-level exposures. The procedures used for taking and analyzing the precession x-ray photographs were those described in the text by Buerger[118] and the manual by the Charles Supper Co.[119] The usual settings used are given in the table below.

TABLE I

Precession X-Ray Camera Settings

	Orientation	0-level
Precession angle, $\bar{\mu}$	10°	20°
Film-to-crystal distance, F	60 mm	60 mm
Screen-to-crystal distance, s	28.4 mm	41.2 mm
Radius of screen, r	6.0 mm	15.0 mm

Precession photographs were taken of at least two low index planes for one cleavage mounting and of one other plane with the cleavage mounted at right angles to its original orientation. The NaCl-NaF and NaBr-NaF eutectics were also checked by this technique to verify the Laue orientation results.

3. THERMAL EXPANSION DETERMINATION

The thermal expansion coefficient of manganous sulfide (MnS) was determined by using high temperature x-ray powder patterns to determine the change in lattice parameter from room temperature to 1200°C. A Rigaku-Denki high temperature x-ray camera with provision for recording powder patterns for several temperatures on a single film was used in this study. The MnS powder was ground to -325 mesh in an agate mortar and inserted in a 0.2 mm vitrified silica tube. The silica tube was then sealed and cemented to an alumina rod 1.5 mm in diameter and 3.5 cm long with a Sauereisen cement. A 28 gauge platinum wire was cemented alongside the silica tube to serve as a standard for calibrating the temperature of the specimen. The furnace was evacuated by a mechanical vacuum pump to reduce air scatter and oxidation. Unfiltered chromium radiation was used at 35 kv and 10 ma to obtained the maximum number of back-reflection lines for measurement. Standard methods of precision lattice parameter determination by extrapolation of a_o versus the Nelson-Riley function to $\theta = 90°$ were utilized. The specimen temperatures indicated by a platinum-10% rhodium thermocouple adjacent to the specimen were corrected to the actual specimen temperature by calculating the lattice parameter of the platinum standard at each temperature and determining the true temperature of the specimen from the linear expansion versus temperature curve for platinum reported by Campbell.[120]

The thermal expansion coefficient of a polycrystalline MnS specimen was determined by the same dilatometric procedure used on the MnO-MnS eutectic specimen to verify the x-ray results. A Leitz HTV dilatometer was used which compared the linear expansion of a 50 mm long specimen with that of a 50 mm Chronin standard at a 200X optical magnification. The linear expansion of the Chronin standard was reported in the Leitz manual[121] from room temperature to 100°C so that the Chronin could be used as a temperature calibration.

4. DEFORMATION AND FRACTURE ANALYSIS

The deformation and fracture modes of single crystal MnO and lamellar MnO-MnS eutectic grains were determined from cleavage and Vickers indentation hardness tests. The fracture behavior was determined by attempting to cleave the MnO and MnO-MnS samples along various crystallographic planes with a sharp blade and by observing the predominant form of fragments caused by crushing. The fracture patterns observed around large Vickers indentations also contributed to this analysis.

The deformation behavior of MnO and the MnO-MnS eutectic was studied by observing the slip lines around Vickers indentations in oblique reflected light at 100 to 500X magnifications. The MnO sample used was a flame-fusion grown single crystal boule obtained from the Marubeni-Iida-America Co., Chicago, Illinois. The low index crystallographic planes on which the indentations were made were

cleaved or ground and checked with Laue back-reflection x-ray photographs.

5. HARDNESS TESTING

The same ground or cleaved planes of the MnO crystal and the MnO-MnS eutectic ingots were used for the Knoop micro-indentation hardness tests. The Knoop indenter is a pyramid with a longitudinal angle of 172°30' and a transverse angle of 130°0'. It gives a diamond shape indentation with diagonals of an approximately 7 to 1 length ratio. Very little elastic recovery occurs along the long diagonal of the Knoop indentation; therefore, the measured length of this diagonal and the dead weight applied load were used to determine the ratio of applied load to unrecovered projected indentation area in kg/mm^2. This is called the Knoop Hardness Number (KHN). A calibrated filar eyepiece was used to measure the indentation length, and a table of KHN values versus indentation lengths published by the Wilson Mechanical Instrument Co. was used to convert the lengths to KHN. Both the Vickers and Knoop hardness indentations were made on a Wilson Tukon Hardness Tester.

CHAPTER IV

RESULTS AND DISCUSSION

The eutectic microstructures of this study consisted of a continuous matrix phase with crystallographically related discontinuous plates or rods of a second phase unidirectionally arrayed in the matrix. A single crystal grain of the matrix phase along with the related rods or plates of the discontinuous phase is considered a eutectic grain. A eutectic colony is a region bounded by a layer of coarse eutectic rods in a fan-like array generated by a convex dome-shaped solidification front cell. A colony cell may include a part of a grain, an entire grain or many grains of the eutectic. A lamella is made up of a plate of each of the two eutectic phases in a two layer composite.

This section will first discuss the results of this study in terms of the crystallographic and microstructural phase relationships for the MnO-MnS, FeO-FeS, NaCl-NaF, NaBr-NaF and LiF-NaF systems, and then the property relationships for thermal expansion, deformation and fracture, and hardness of the MnO-MnS system.

A. Phase Relationships

1. CRYSTALLOGRAPHIC ORIENTATIONS

This section will discuss the results of crystallographic orientation studies on MnO-MnS, FeO-FeS, NaCl-NaF, NaBr-NaF and LiF-NaF. The nominal orientation of each

phase of the eutectics with respect to the interface plane between lamellae and the growth direction of the ingot will be summarized in the notation of Kraft;[58] i.e.,

$$\text{Interface} \parallel (hkl)_\alpha \parallel (h'k'l')_\beta$$
$$\text{Growth Direction} \parallel [h''k''l'']_\alpha \parallel [h'''k'''l''']_\beta$$

The symbol $\parallel$ means "is parallel to." The crystal planes are indicated by their (hkl) Miller indices in parentheses, and crystal directions are indicated by their [hkl] lattice intercepts in square brackets.

a. MnO-MnS

$$\text{Interface} \parallel (111)_{MnS} \parallel (111)_{MnO}$$
$$\text{Growth Direction} \parallel [11\bar{2}]_{MnS} \parallel [11\bar{2}]_{MnO}$$
$$\text{Continuous Phase} = MnS$$

The MnO and MnS phases exhibit a common (111) plane interface and an approximately common $[11\bar{2}]$ growth direction (Figure 7). A twist misorientation corresponding to a 3° rotation about the common [111] interface normal was consistently observed between the $[11\bar{2}]$ growth directions of the two phases as shown in the x-ray precession camera photographs of Figure 8. The twist direction indicates that the MnS phase tends to have a greater lattice rotation towards the crucible wall than the MnO phase at all points in the eutectic. The MnS phase is the leading phase according to the microstructural appearance near transverse bands and the fact that it is the continuous phase, as is discussed later. There is also a slight mosaic substructure evident in precession photographs normal to the lamellar interface or in

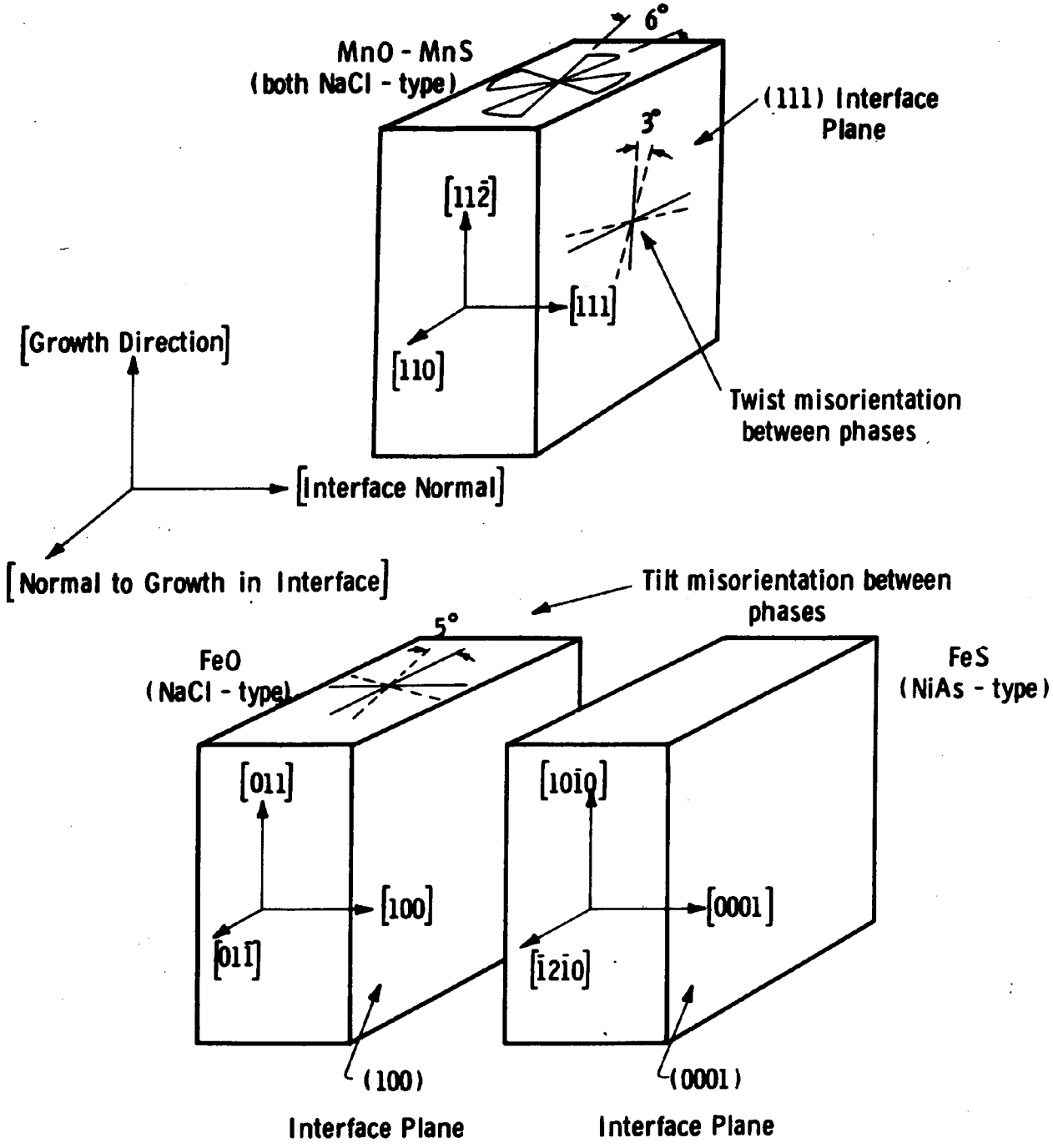
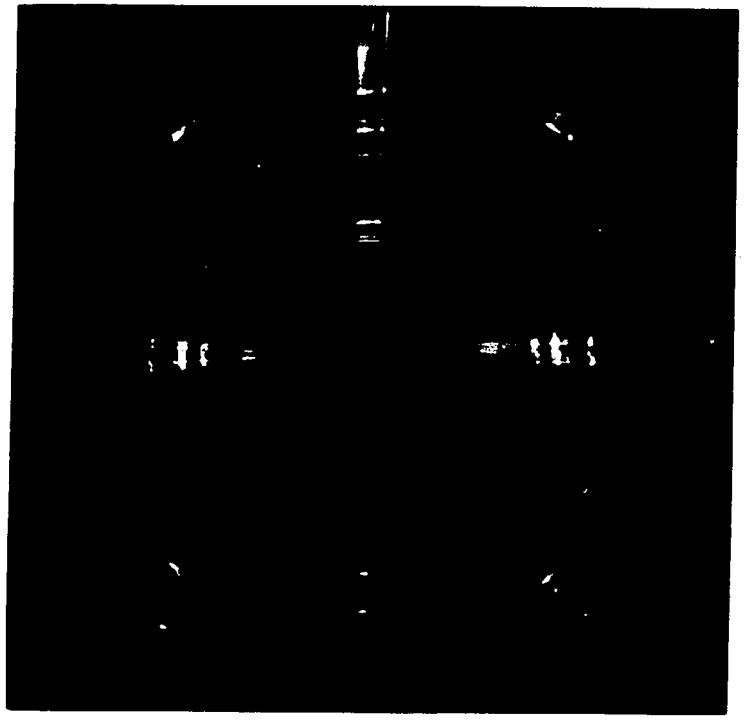
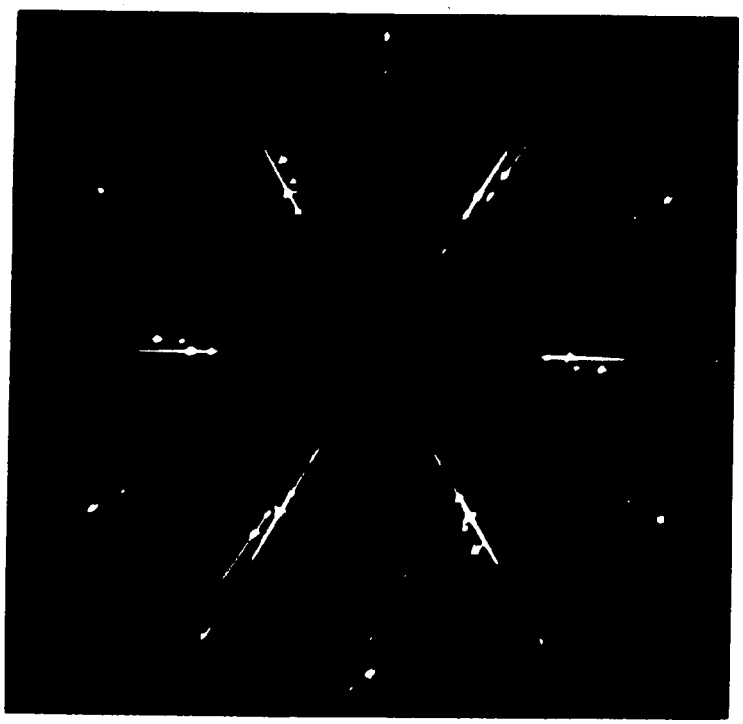


Figure 7. Crystallographic orientations of MnO-MnS and FeO-FeS eutectic phases in relation to lamellar interfaces and growth directions.



(a) Parallel to Growth Direction [112].

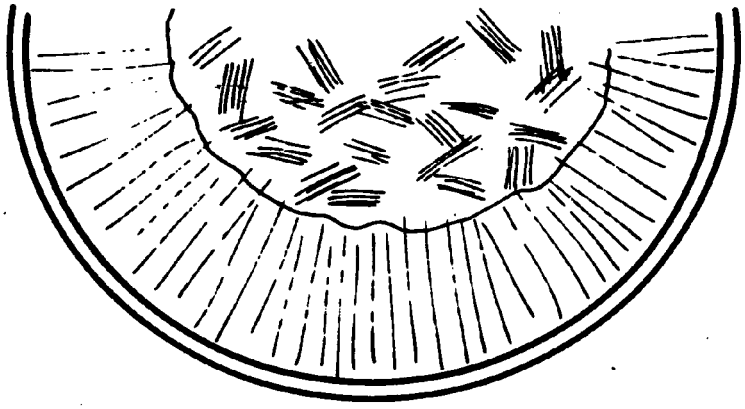


(b) Parallel to Interface Normal [111]

Figure 8. Buerger precession zero-level x-ray transmission photographs of lamellar MnO-MnS eutectic.

the [11$\bar{2}$] direction with a simultaneous rotation of both phases of ± 3° about the growth axis (Figure 8).

A schematic cross section of an MnO-MnS ingot showing the curving solidification front and resultant curved grains along with the misorientation amounts and directions observed across a typical cross section is shown in Figure 9. The fact that the direction of the misorientation corresponds with the direction in which the lamellae are curving indicates that the factor controlling the misorientation may be the tendency for each phase to grow normal to the solidification front. This mechanism might also be used to explain the constant misorientation value of 3° if it is hypothesized that the solidification front of one phase could be rotated by as much as 3° relative to the other phase. This would involve a variation in the distance that the MnS phase leads the MnO phase along the ingot radius (Figure 9). However, the 3° misorientation found in the MnO-MnS system would only require that the MnO phase lag behind the MnS phase by about 0.0065 inches more in the center than at the periphery of the 1/4 inch diameter ingot. A mechanism for such a lag can be postulated on the basis that the dome-shaped solidification front would force radial diffusion, and consequently a radial impurity gradient, across the solidification front. Chadwick has postulated that the lamellae of phase β will grow a finite distance behind phase α when an impurity, x, has a smaller partition coefficient in the β phase, k_x^β, than in the α phase, k_x^α.[36] This leads to a



Transverse Ingot Cross-section Showing
Radial Lamellae Around Periphery of Ingot

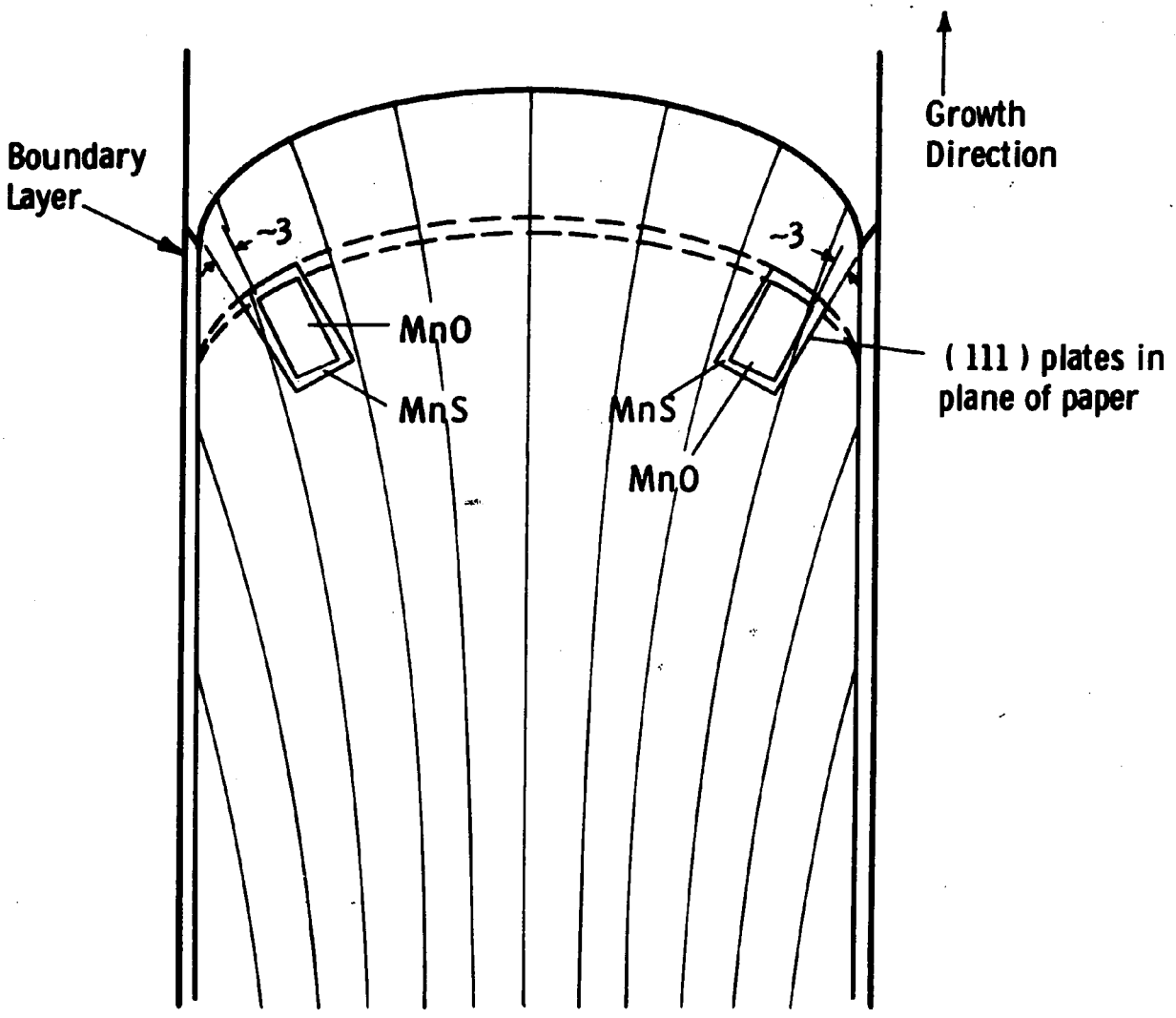


Figure 9. Schematic diagram of crystallographic misorientation between MnO and MnS lamellae versus radial curvature direction of solidification front.

greater concentration of solute, x, ahead of the β lamellae and thus a lower equilibrium freezing point for the liquid ahead of β, causing it to grow behind α. If a radial concentration gradient of the solute, x, is imposed upon Chadwick's model, it is only necessary to postulate that the ratio of k_x^β/k_x^α varies with the absolute concentration of x to define a system in which the lag distance of phase β behind phase α would vary along the radial concentration gradient. This in effect would mean that each phase would have a different radius of curvature at its solidification interface; thus, the phase with the flatter growth front would grow with the least lamellar curvature as the lamellae grow normal to the solidification front. The postulate that the ratio of k_x^β/k_x^α varies with the absolute concentration of x is precisely the one which Chadwick uses to explain the premature lamellar-to-rod breakdown at colony boundaries.[37] Therefore, it seems appropriate to use it here since this breakdown phenomenon is also observed in the MnO-MnS colonies (Figure 25). The radial lamellae which seemed to predominate around the outer radius in the central section of the MnO-MnS ingots would also be favored by the above mechanism since the lateral diffusion would tend to disturb the concentration gradients ahead of non-radial lamellae, thus causing them to break down into the more easily curved rods which would presumably grow out to the edge of the ingot and disappear. This coincides with the observation that lamellae in small colonies tend to break down into rods more easily when they are not

radially oriented (Figure 25).

Many attempts were also made to determine the crystallographic orientations of MnO and MnS phases by Laue back-reflection x-ray methods, but due to excessive background and smearing of the Laue spots, the patterns were not uniquely interpretable. The smearing of the Laue spots seems to support the hypothesis that severe interlamellar strains due to cooling the eutectic from the solidification temperature to room temperature are present.

b. FeO-FeS

$$\text{Interface} \parallel (100)_{FeO} \parallel (0001)_{FeS}$$
$$\text{Growth Direction} \parallel [110]_{FeO} \parallel [10\bar{1}0]_{FeS}$$
$$\text{Continuous Phase} = FeS$$

The FeO-FeS system was chosen for study since it involves an NaCl structure compound (FeO) and an NiAs structure compound (FeS) which differ primarily in the stacking of their hexagonally arrayed, close-packed anion planes. FeO can be considered a stack of hexagonally arrayed (111) planes in an ABCABC sequence. FeS can be considered a stack of hexagonally arrayed (0001) planes in an ABAB sequence. Since the dense (111) planes were the interface planes in the MnO-MnS system it was expected that (111) and (0001) might be the respective interfaces in the FeO-FeS eutectic.

The FeO-FeS microstructure was made up primarily of a rod-like dispersion of FeO in the FeS matrix. The rods generally tended to be aligned in rows, however, and occasionally exhibited a ribbon-like cross section with small regions of true lamellae (Figure 15). There were no regions

in which cellular colony structure was absent as in the MnO-MnS ingots; therefore, it is concluded that the equilibrium orientations of the phases might not have been completely established.

The region studied by the Buerger precession technique is shown in Figure 15, and the orientations of the phases with respect to the psuedo-lamellae and the growth direction are shown in Figure 7.

The interface plane of the FeS matrix phase was found to be the (0001) plane in this NiAs structure, agreeing with the findings in the MnO-MnS system described above. However, the coincident plane in the FeO phase was found to be approximately equal to the (100) plane. A 5° rotation about the [110] axis of the FeO phase normal to both the growth direction and interface normal was the only misorientation observable between the phases. This is the direction of rotation required to bring the (111) FeO plane into coincidence with the (0001) plane. This rotation would also give the same $[11\bar{2}]$ growth direction in FeO which was found in both the MnO and MnS phases.

Laue back-reflection x-ray photographs were also tried on the FeO-FeS system but without success due to excessive background and smearing of the spots.

The observation that the matrix phase is oriented as expected while the dispersed phase is tending toward the expected orientation would correspond with the observation of Kraft regarding the Al-$CuAl_2$ system.[58] He observed that the

matrix phase achieved its equilibrium orientation very quickly but that a greater growth distance was required for the dispersed phase to become properly oriented. In this work the marked colony structure prevented detection of any further re-orientation of the FeO phase towards the $[11\bar{2}]$ growth direction than 5°. It may also be that a slight misorientation between the phases is a low energy configuration due to the difference in lattice parameter of the phases.

c. NaCl-NaF

$$\text{Interface} \parallel (110)_{NaCl} \parallel (110)_{NaF}$$
$$\text{Growth Direction} \parallel [001]_{NaCl} \parallel [001]_{NaF}$$
$$\text{Continuous Phase} = NaCl$$

The NaCl-NaF eutectic was checked for crystallographic orientation by both Laue back-reflection and Buerger precession x-ray techniques. Four different grains were checked by the Laue method in the ingot studied, and all four exhibited a [001] growth direction and a (110) interface plane between lamellae (Figure 10). Three of the four also exhibited a 3 to 4° rotation of one phase pattern about the [001] axis towards a $[11\bar{2}]$ direction and the same amount about the [110] axis towards a (111) interface plane. There was much less smearing of the Laue spots in this system compared with the oxide-sulfide Laue photographs, indicating that less internal strain and mosaic are present at room temperature. The microstructure in the region where the Laue study was made consisted of a very regular lamellar array parallel to the growth direction with little curvature of lamellae. However, the region checked was only from

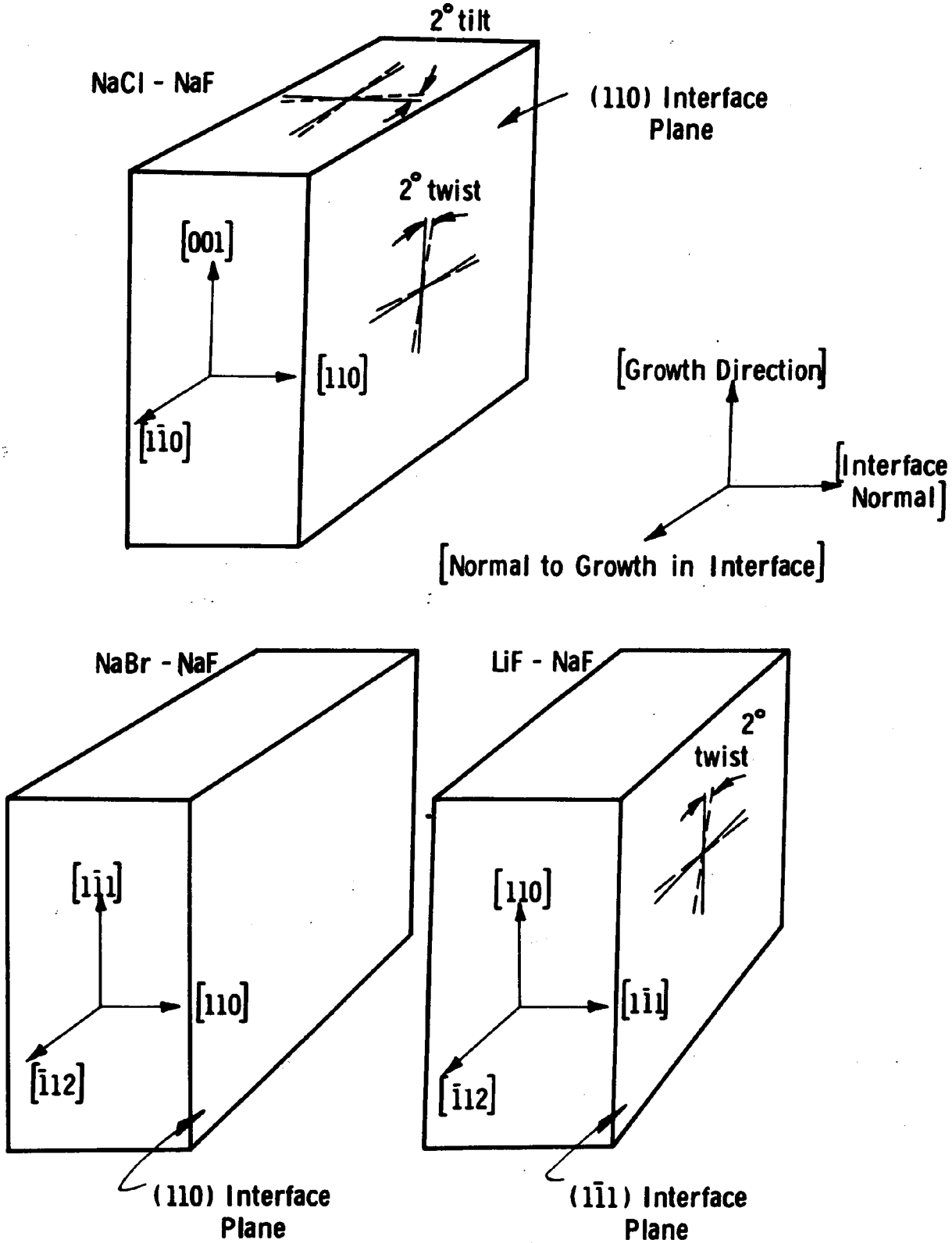


Figure 10. Crystallographic orientations of NaCl-NaF, NaBr-NaF and LiF-NaF eutectic phases in relation to lamellar interfaces and growth directions.

1 1/2 to 3 cm above the bottom of the ingot; therefore, the stable crystallographic orientation may not have been achieved. There did not seem to be any greater rotation than 3 to 4° towards the (111) and <112> orientations anywhere along the ingot length studied.

A very clear doubling of all the spots of the primary pattern was observed in all Laue photographs of this system (Figure 11).

A single cleavage fragment was studied by the precession x-ray technique, and the orientations indicated by the Laue study were confirmed. The misorientations indicated by this method were a 2° tilt of the interface plane and a 2° twist about the lamellar interface normal. These are the same misorientations indicated by the Laue photographs, but they are of smaller magnitude. The cleavage fragment was taken at 5 cm above the ingot bottom, and the grains were curving towards the crucible wall.

Penfold and Hellawell[22] have reported observation of lamellae which lie in two lateral directions at an angle of approximately 70° to each other in transverse sections of LiF-NaF and NaCl-NaF colonies. Truelove and Hellawell[23] have determined that the interphase boundary in these two eutectics corresponds within ± 10° to a {111} plane, according to Laue x-ray back reflection photographs. They noted that all their patterns could be indexed as two cubic lattices with a misorientation of less than 4°. They further observed that precipitates of NaF in an NaCl matrix had an

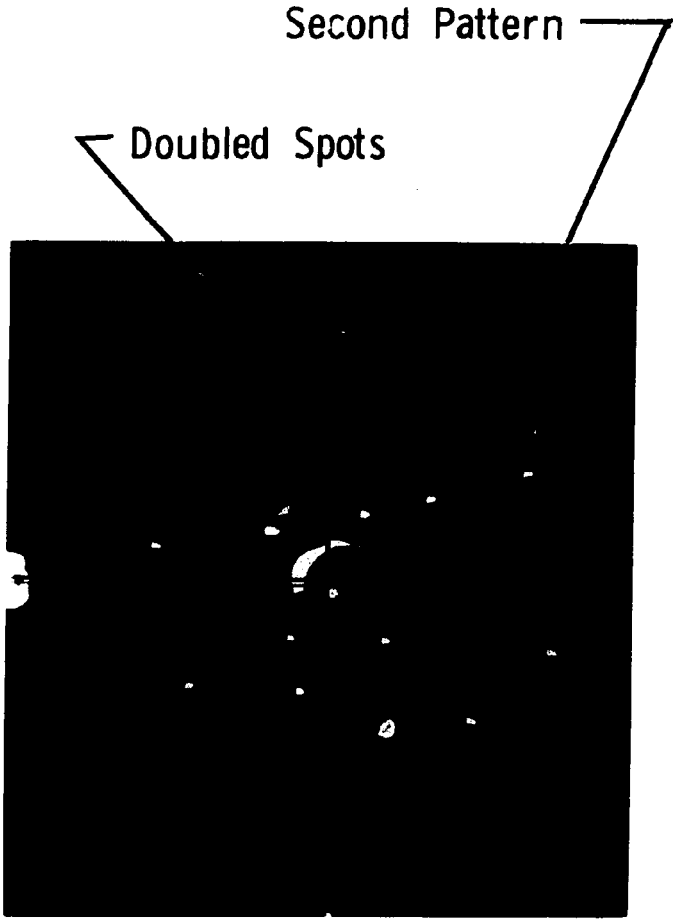


Figure 11. NaCl-NaF Laue exhibiting doubling of spots and second cubic pattern rotated 2° from primary pattern.

octahedral habit with the {111} planes of the octahedra oriented parallel to the {111} planes of the NaCl matrix. They attribute the tendency for {111} interlamellar planes to the homopolarity of such planes, although they note that there is not an exclusive preference for homopolar habit planes in other alkali halide dispersed particle systems.

Sundquist et al[53] have shown that the formation of regular lamellar or rod-like metallic eutectics with simple crystallographic relationships between the phases is due to nucleation of one phase by the other. However, they found as a rule that a multiplicity of different, simple crystallographic relationships could occur. It would not be expected, therefore, that all grains of a eutectic ingot would nucleate and grow with the same crystallographic relationships unless some influence such as an impurity were causing a particular relationship to be preferred throughout the ingot. It is well established that certain impurities can "poison" or inhibit growth on certain planes of growing crystals, completely changing their external shape. Thus, different impurities in the crucible or charge might cause different relationships of the several possible to be preferred in the same eutectic system.

d. NaBr-NaF

$$\text{Interface} \parallel (110)_{NaBr} \parallel (110)_{NaF}$$
$$\text{Growth Direction} \parallel [1\bar{1}1]_{NaBr} \parallel [1\bar{1}1]_{NaF}$$
$$\text{Continuous Phase} = NaBr$$

The NaBr-NaF system was studied by Laue and precession techniques in a limited region where a lamellar

microstructure was obtained. The Laue photographs indicated that the growth direction was approximately a $[1\bar{1}1]$ axis and that the interface was a (110) plane as in the case of NaCl-NaF (Figure 10). Well defined Laue spots with a fine doubling as in the case of NaCl-NaF were also observed.

A cleavage fragment taken from the same region and carefully oriented with respect to the lamellae verified the growth direction and interface indicated by the Laue photographs. There were no slight misorientations between phases in this case. The growth front, however, did not have a well defined curvature in the region studied in this system.

e. LiF-NaF

$$\text{Interface} \parallel (111)_{LiF} \parallel (111)_{NaF}$$
$$\text{Growth Direction} \parallel [1\bar{1}0]_{LiF} \parallel [1\bar{1}0]_{NaF}$$
$$\text{Continuous Phase} = \text{NaF}$$

The LiF-NaF eutectic was studied by both back-reflection and precession techniques. The back reflection photographs were very similar to those obtained for the oxide-sulfide systems. The spots were smeared and spotty, indicating that residual internal strains and mosaic substructure were more pronounced in this system than in the other two alkali halides.

The precession orientation of a cleavage fragment taken from a section 7 1/2 cm above the ingot bottom and 7 cm above the beginning of a unidirectionally oriented region indicated that the lamellar interface was a (111) plane as in the MnO-MnS system. The growth axis, however, was found

to be a <110> direction (Figure 10). A twist misorientation of 2° about the interface normal was also observed. This would be the proper rotation to bring the <112> axis around as the growth direction, but the rotation was not observed to increase along the length of the ingot. The growth front had a slight curvature in this ingot which might be the cause of this misorientation by the same mechanisms postulated for the MnO-MnS system.

2. MICROSTRUCTURE

This section will discuss the results of microstructural observations of the five eutectic systems in terms of their phase morphologies, colony structures, and microstructural irregularities.

a. Phase Morphology

The observed phase morphology for the MnO-MnS eutectic is a uniform array of nearly continuous lamellae or plates of manganous oxide (MnO) in a fully continuous matrix of manganous sulfide (MnS) (Figure 12). Lamellar regions were also observed in LiF-NaF (Figure 13), NaCl-NaF (Figure 14) and FeO-FeS (Figure 15). Flattened ribbons and linear arrays of rods suggesting an impurity-modified lamellar structure were observed in the NaBr-NaF system (Figure 16).

It has been previously reported[17] that the lamellar structure is the stable morphology for most two component metallic eutectics when the third component impurity level is very low. The boundary energies of the rod and lamellar

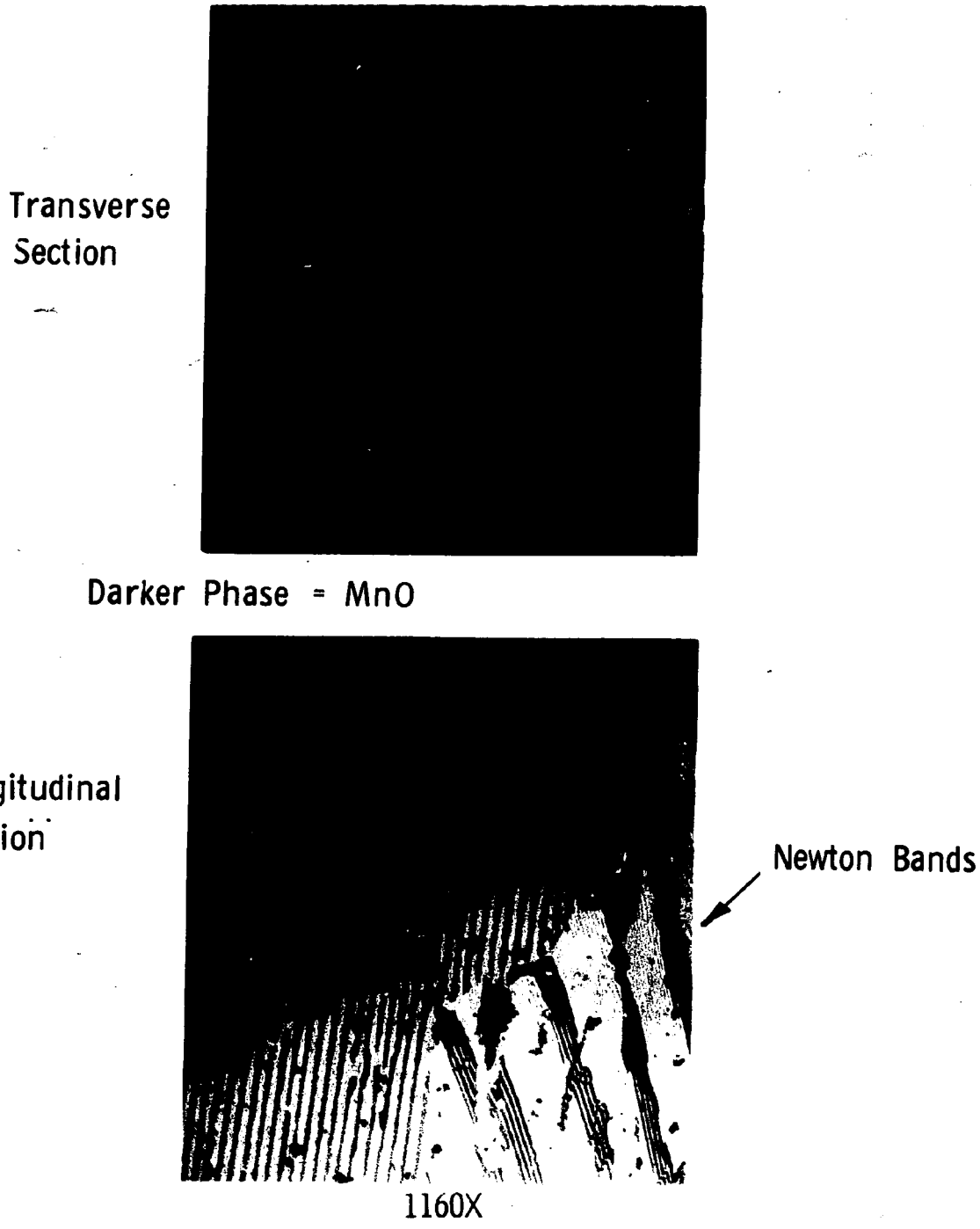
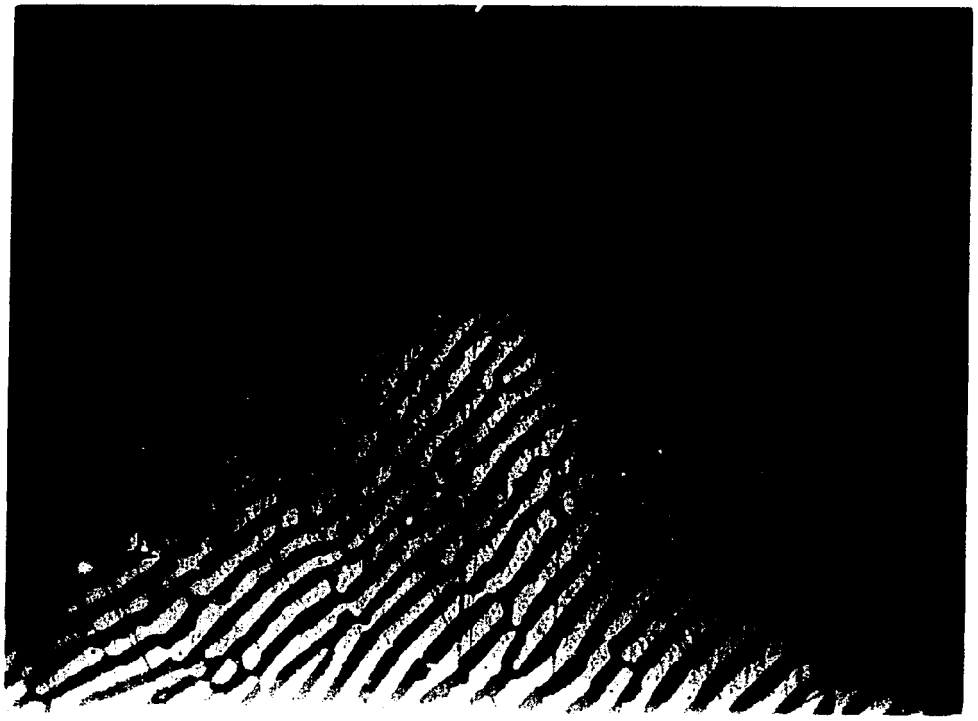
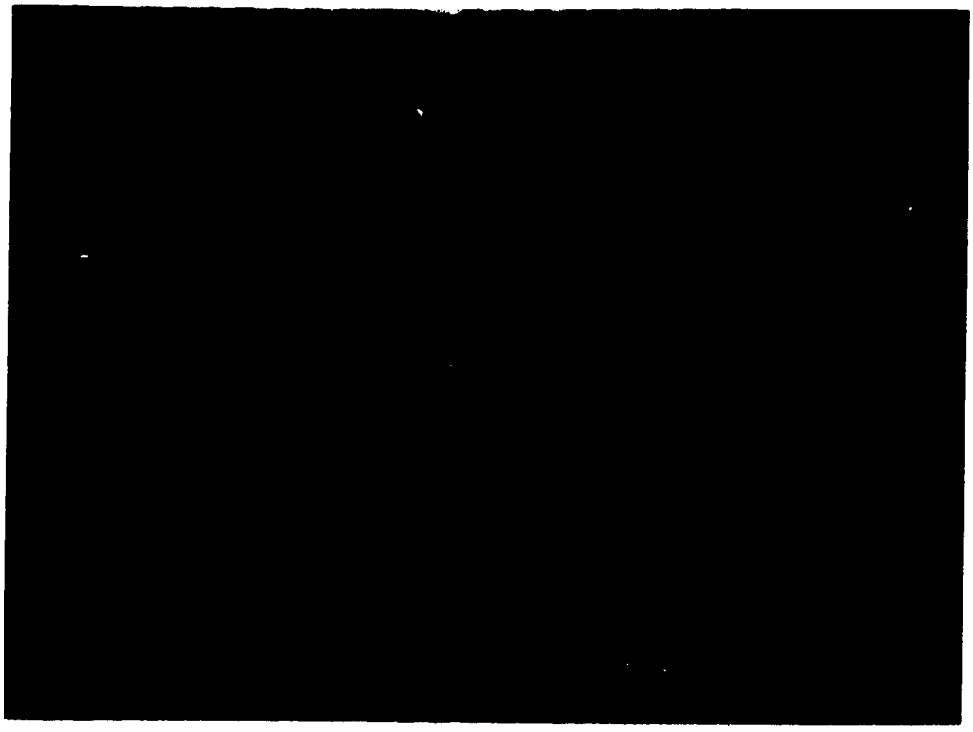


Figure 12. Lamellar microstructure of the MnO-MnS eutectic.



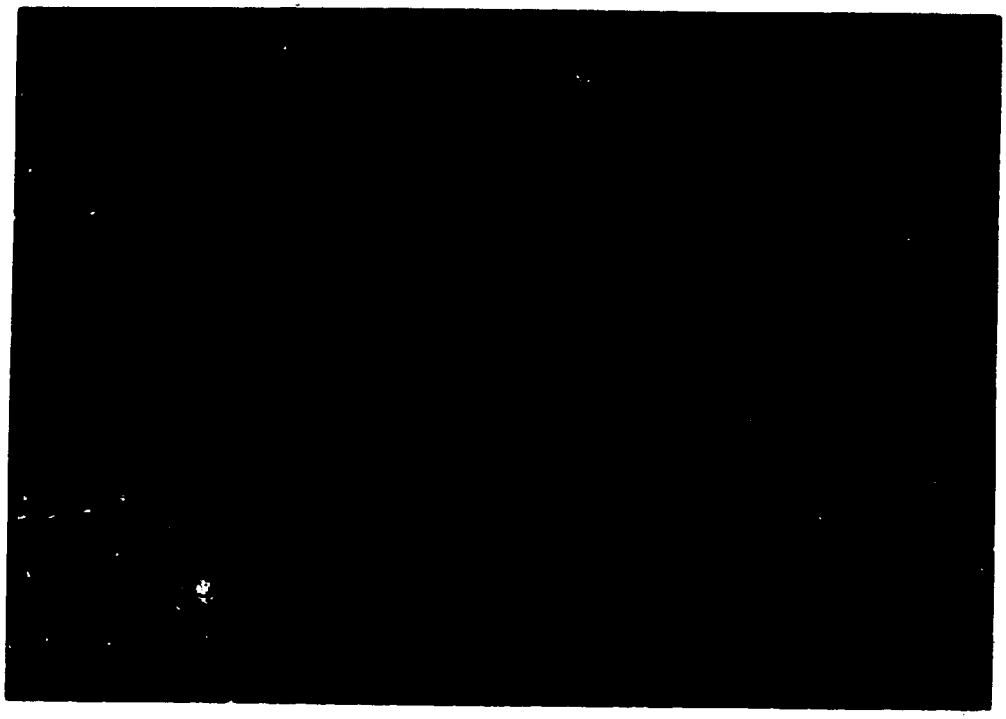
Transverse Section

Darker Phase = NaF



Longitudinal Section.

Figure 13. Lamellar microstructure of the LiF-NaF eutectic. 500X.



Transverse Section

Darker Phase = NaF

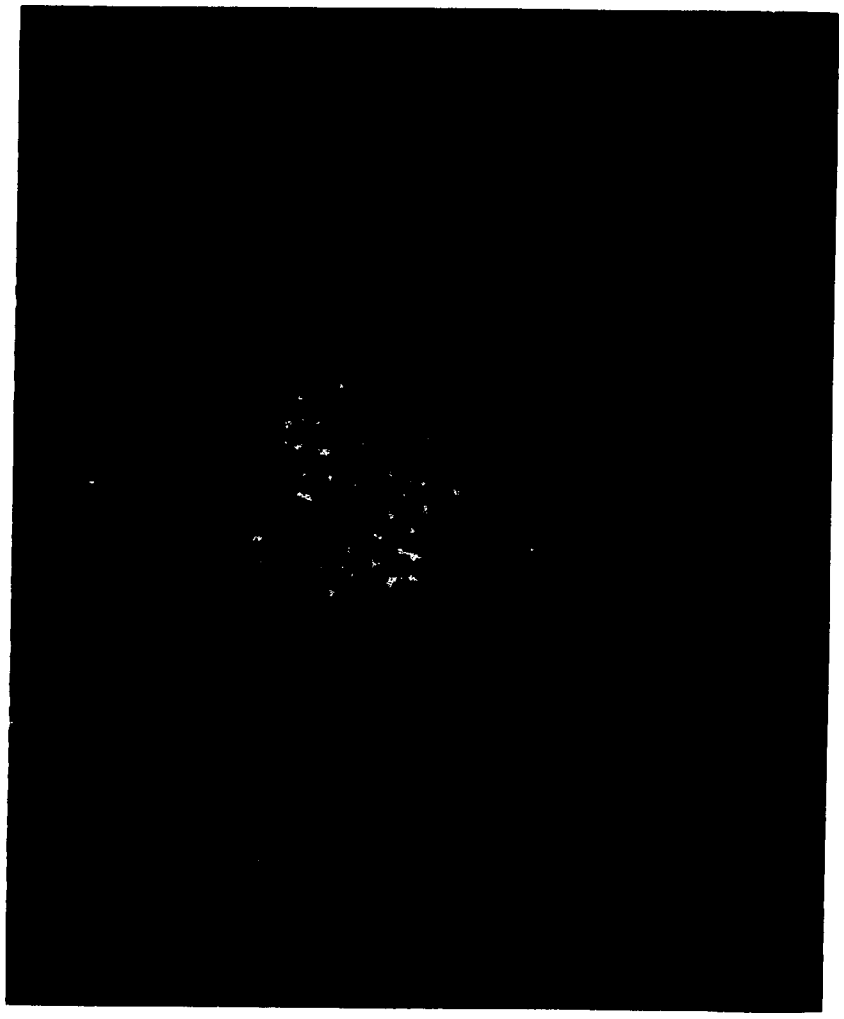


Longitudinal Section

Figure 14. Lamellar microstructure of the NaCl-NaF eutectic. 500X.



Figure 15. Lamellar microstructure of the FeO-FeS eutectic. 100X.



Transverse Section

Darker Phase = NaF

Figure 16. Microstructure of the NaBr-NaF eutectic. 500X.

morphologies cannot be compared since the variation of solid interphase boundary energy with crystallographic orientation cannot as yet be quantitatively evaluated. Various authors[21, 40, 45] have attempted to show geometrically that the interphase surface area can be lowered by forming rods instead of lamellae if the volume ratio of the discontinuous to continuous phase is less than about 0.3. The volume ratio and identities of the discontinuous phases for the five eutectics studied are shown in Table II.

TABLE II

Volume Ratios of Discontinuous Phases

Eutectic	Discontinuous Phase	Volume Ratio $\left(\frac{\text{Vol.\% disc.}}{\text{Vol.\% cont.}}\right)$
LiF-NaF	LiF	0.95
MnO-MnS	MnO	0.77
FeO-FeS	FeO	0.52
NaCl-NaF	NaF	0.30
NaBr-NaF	NaF	0.20

The two eutectics in which the volume fraction of the discontinuous phase was highest gave very uniform lamellar microstructures, while only small regions of less uniform lamellae were obtained in the other three eutectics in which the volume fraction of the discontinuous phase was 0.52 or less. However, the rod morphology of the FeO-FeS, NaCl-NaF and NaBr-NaF eutectics may be due to the third component impurity modification mechanism postulated by Chadwick.[37] Lamellar phase morphologies have been obtained in high

purity metallic eutectics in which the volume ratio of the discontinuous phase was as low as 0.1,[37] while eutectic phases with volume ratios close to 1.0 have been solidified in the rod-like morphology by adding impurities.[43] The presence of impurities is indicated in all of the eutectics studied by the existence of colony structures, which Chilton and Winegard[41] have shown occur only in the presence of impurities. The colony structures of the FeO-FeS (Figure 15), NaCl-NaF and NaBr-NaF eutectics were generally more extensive than those of the LiF-NaF and MnO-MnS eutectics.

The width of the lamellae, λ, in the MnO-MnS microstructure is increased by decreasing the solidification rate, R (Figure 17). This effect has been observed in metallic eutectics[35, 17, 33, 45] as well as in the LiF-NaF system. The curve of logarithm λ versus logarithm R for LiF-NaF obtained by Penfold and Hellawell[22] is shown in Figure 17 for comparison with the MnO-MnS data. A single measurement of solidification rate versus lamellar spacing was made for each of the alkali halide eutectics in this study (Figure 17). The LiF-NaF data point fell close to but not on the LiF-NaF curve of Penfold and Hellawell. The LiF-NaF[22] and MnO-MnS curves have approximately the same slope, but the spacings of the MnO-MnS lamellae are slightly smaller for any particular solidification rate than the spacings of the LiF-NaF lamellae. This could indicate a difference in the liquid phase diffusion coefficients and/or the interphase boundary energies of the two eutectics. This

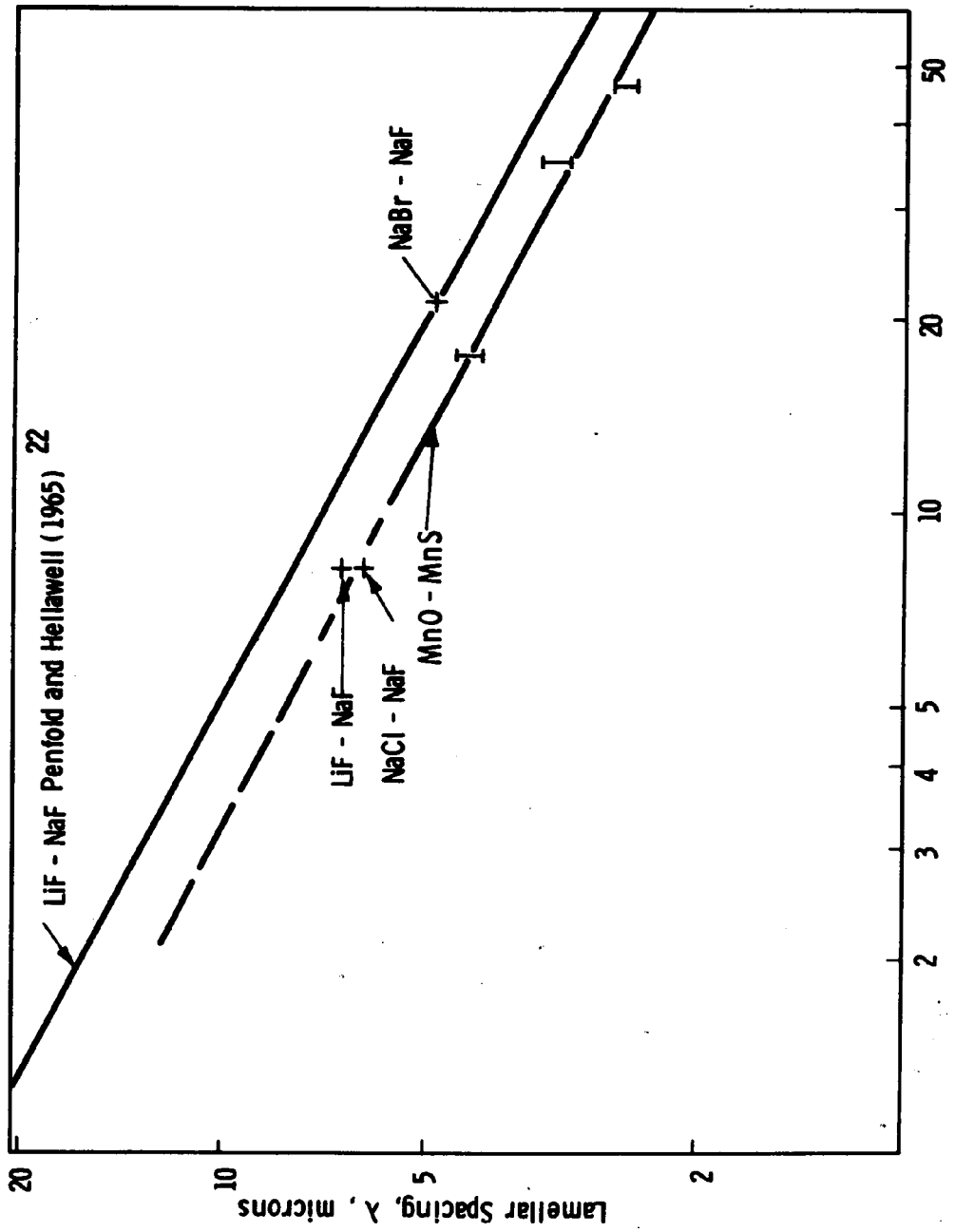


Figure 17. Lamellar spacing versus solidification rate for the MnO-MnS eutectic compared with alkali halide eutectic data of Penfold and Hellawell[22] and this study.

would not be unexpected, but data are not available on their diffusion coefficients or solid interphase boundary energies for correlation. The same data as in Figure 17 can be plotted in the fashion of Tiller,[40] Chadwick,[17] and Yue[36] as lamellar spacing, λ, versus the inverse square root of the growth rate, $R^{-1/2}$ (Figure 18). Both the LiF-NaF data of Penfold[22] and the MnO-MnS data of this study can be represented by straight lines drawn through the origin of this plot. This type of curve has been observed empirically in all the metallic eutectics studied to date, but the reason for it has not been well established theoretically.

It can be concluded, therefore, that the lamellar phase morphology is the stable form for the MnO-MnS and LiF-NaF eutectics. The evidence further indicates that the lamellar morphology occurs in some regions of the FeO-FeS, NaCl-NaF and NaBr-NaF eutectics and thus may be the equilibrium morphology for these eutectics at lower impurity levels than those of this study. The most uniform lamellar microstructures were obtained for the eutectic systems in which the volume ratio of the discontinuous to the continuous phase was above 0.5, where the lamellar morphology can provide a lower interphase boundary area than the rod morphology in addition to providing a lower energy, crystallographically oriented plane boundary.

The translucent ceramic phases present in the eutectic ingots of this study permit an additional method of microstructural analysis not available in the metal eutectics of

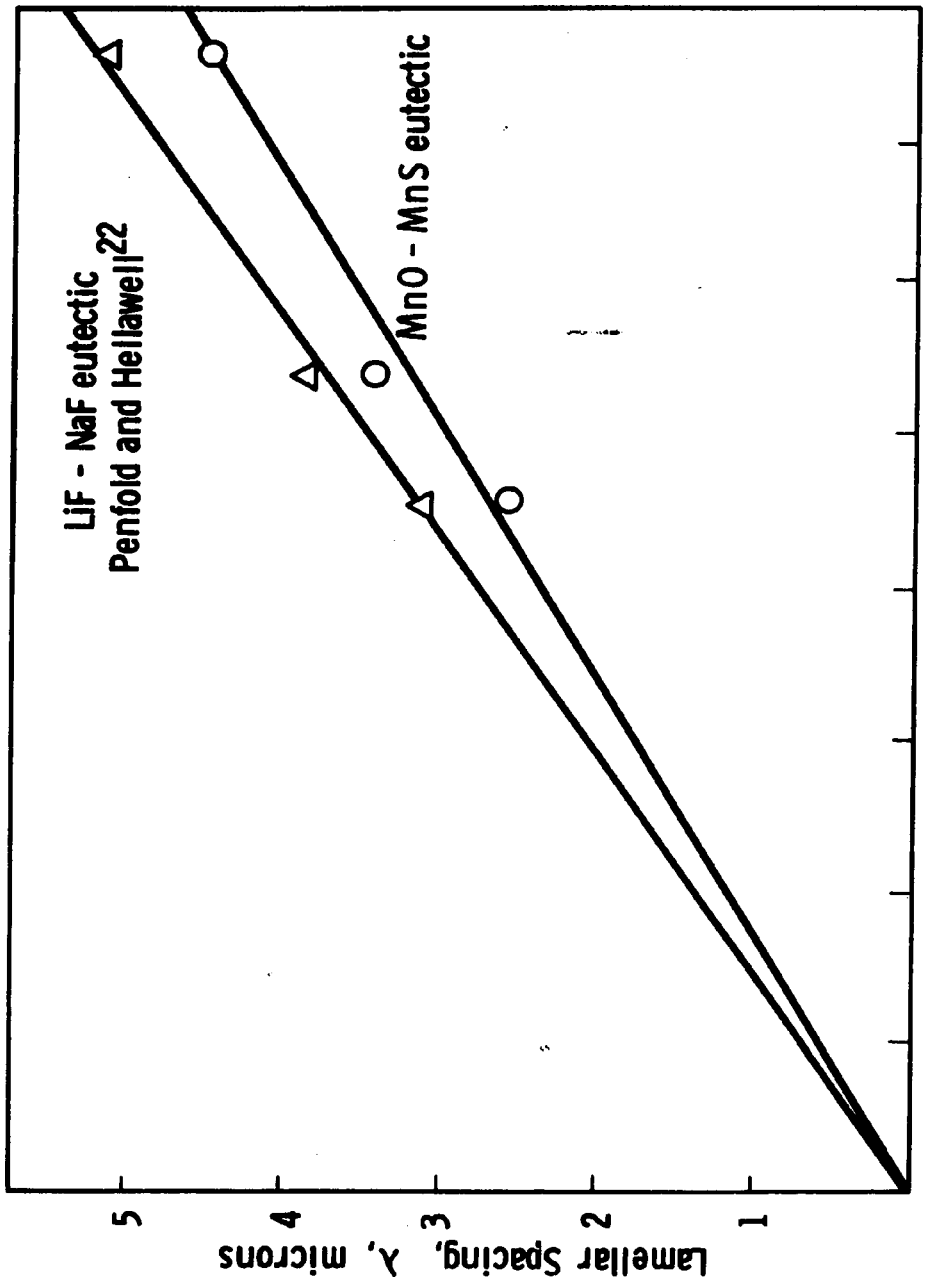


Figure 18. Lamellar spacing versus the inverse square root of solidification rate for MnO-MnS and LiF-NaF. LiF-NaF after Penfold and Hellawell.[22]

previous investigations. Alternating light and dark bands were observed in high angle sections of MnO and MnS plates at high (500X) reflected light magnifications with the use of a green filtered (Wratten 57) tungsten filament light source (Figure 12). The separation of the bands increased as the angle of sectioning approached 0° with respect to the plane of the lamellae. The bands were more closely spaced in the MnS phase, which has a higher index of refraction (n_{MnS} = 2.70) than that of the MnO phase (n_{MnO} = 2.16). Careful examination also showed that the tip of the MnS wedge was a dark band and the tip of the MnO wedge was a light band. These observations indicated that the bands observed were Newton or Fizeau bands. They are caused by interference (dark) or reinforcement (light) of the light waves reflected from the polished upper surface of the lamellae and the internal phase boundary between the plates. Interference occurs when there is an integral number of waves in the optical path between the two surfaces for the MnS plates. This is because the light is reflected at the upper surface of the MnS from a medium of greater index (n_{MnS} - 2.70) than that in which it is traveling ($n_{air} \sim 1$) while at the internal surface the reverse is true (n_{MnO} = 2.16). When a train of waves is reflected at a surface of a medium of a higher index the reflected wave train loses half a wavelength.[122] Thus, at the tip of the MnS wedge where the plate thickness is less than a wavelength of light, the optical path length is negligible, and the only effect is the loss

of the half wavelength for the waves reflected at the first surface. Therefore, the tip of the MnS wedge will remain dark for all wavelengths since the waves reflected from the second surface of lower refractive index do not lose a half wave. In the case of the MnO plates the half wave loss occurs at both the first and second surfaces [optical path = air (1.0) → MnO (2.16) → MnS (2.70)]; therefore, the tip will always be a light band. This also means that the dark bands in MnO occur at thicknesses of an integral number of wavelengths plus a half wavelength in contrast to MnS. The spacing of the bands is a function of the wavelength of the light, index of refraction of the phase, and angle of section of the lamellae. It appears that these phenomena could be used as aids in determining precise thicknesses or angles of lamellae or the identity of translucent phases in lamellar eutectics. This permits analysis, not possible in opaque solids, of a third dimension from a two dimensional surface.

b. Colony Structure

Each of the ionic eutectics studied showed colony structures similar to those encountered in metallic eutectic microstructures (Figures 19 and 20). It is assumed from studies of metallic eutectics[17] that these colonies were generated by an impurity-controlled, cellular solidification front. Colonies can be identified by their boundary zones where the discontinuous phase forms coarse rods curving away from the primary direction of solidification. In the

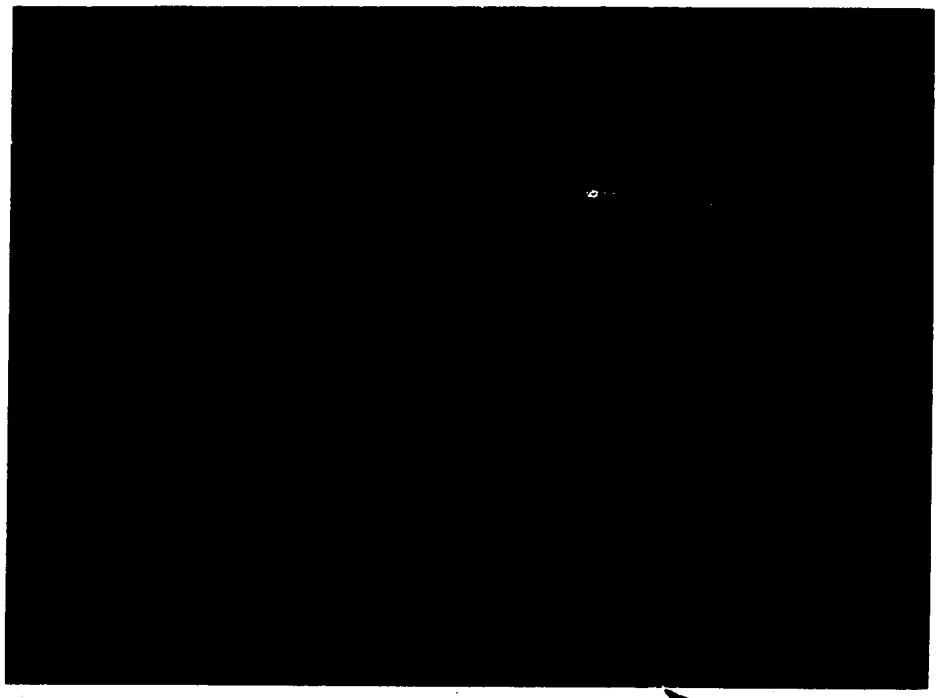


Figure 19. Transverse cross section of MnO-MnS eutectic colonies. 100X.

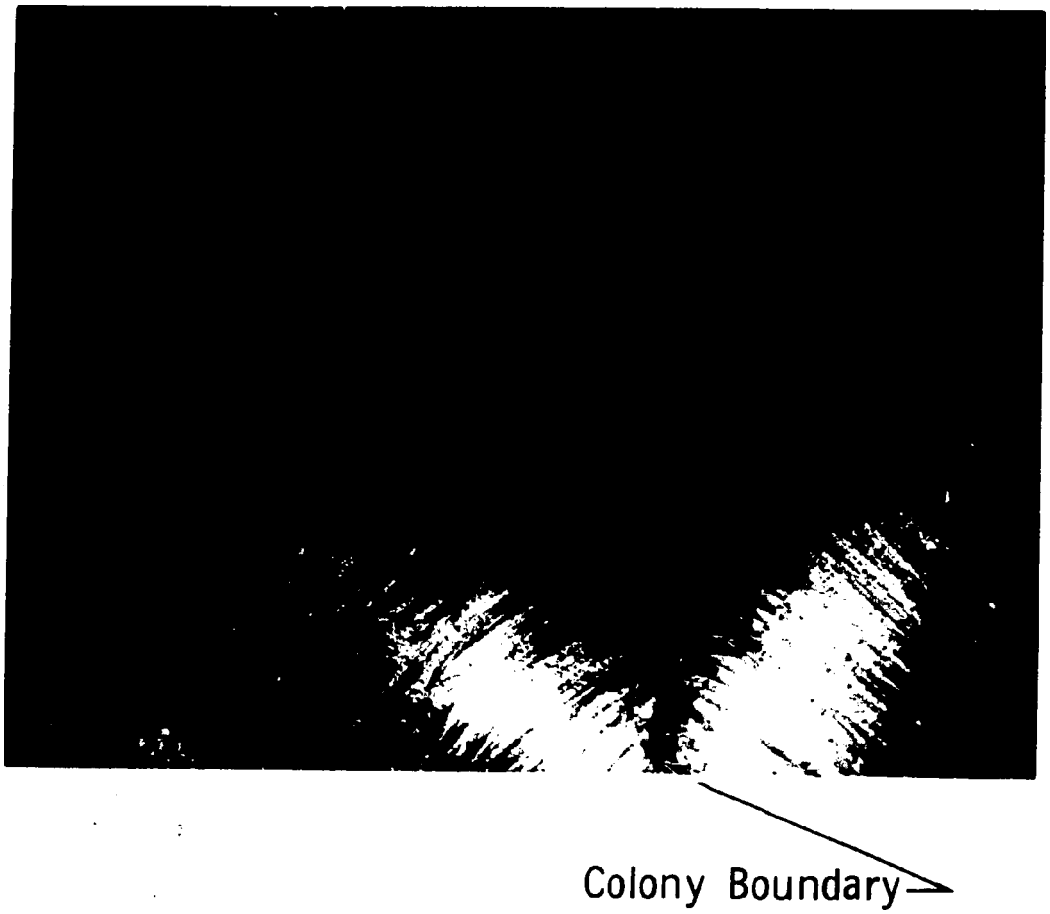


Figure 20. Transverse cross section of NaBr-NaF eutectic colonies. 500X.

initial portion of all ingots each colony tends to consist of a single grain, and there are many such grain-colonies. As solidification continues some colonies become elongated in the growth direction (Figure 21). The number of colonies and grains in an ingot cross section gradually decreases as some are squeezed out by others which may have more favorable orientations (Figure 22). Repeated nucleation of grains as noted by Cooksey et al[21] in metallic eutectics was not observed beyond the short initial region of random colonies.

The solidification front very quickly stabilized as a single large cell extending across the entire ingot cross section (Figures 23 and 24). Transverse bands or discontinuities in the microstructure (Figure 23) similar to those reported by Kraft[43] in the Al-$CuAl_2$ system were observed in the MnO-MnS ingots at locations which correlated with interruptions in crucible traverse rate or furnace conditions. Kraft was unable to trace all such banding in his eutectics to process variations and therefore concluded that some banding was inherent in the solidification process. The fact that the bands observed have a curved shape which is always normal to the rod or lamellar growth directions in a longitudinal cross section indicates that they represent the shape of the domed solidification front at the time of the perturbation which caused the banding.

The rapid formation of a single cell or domed solidification front across the entire cross section in all the

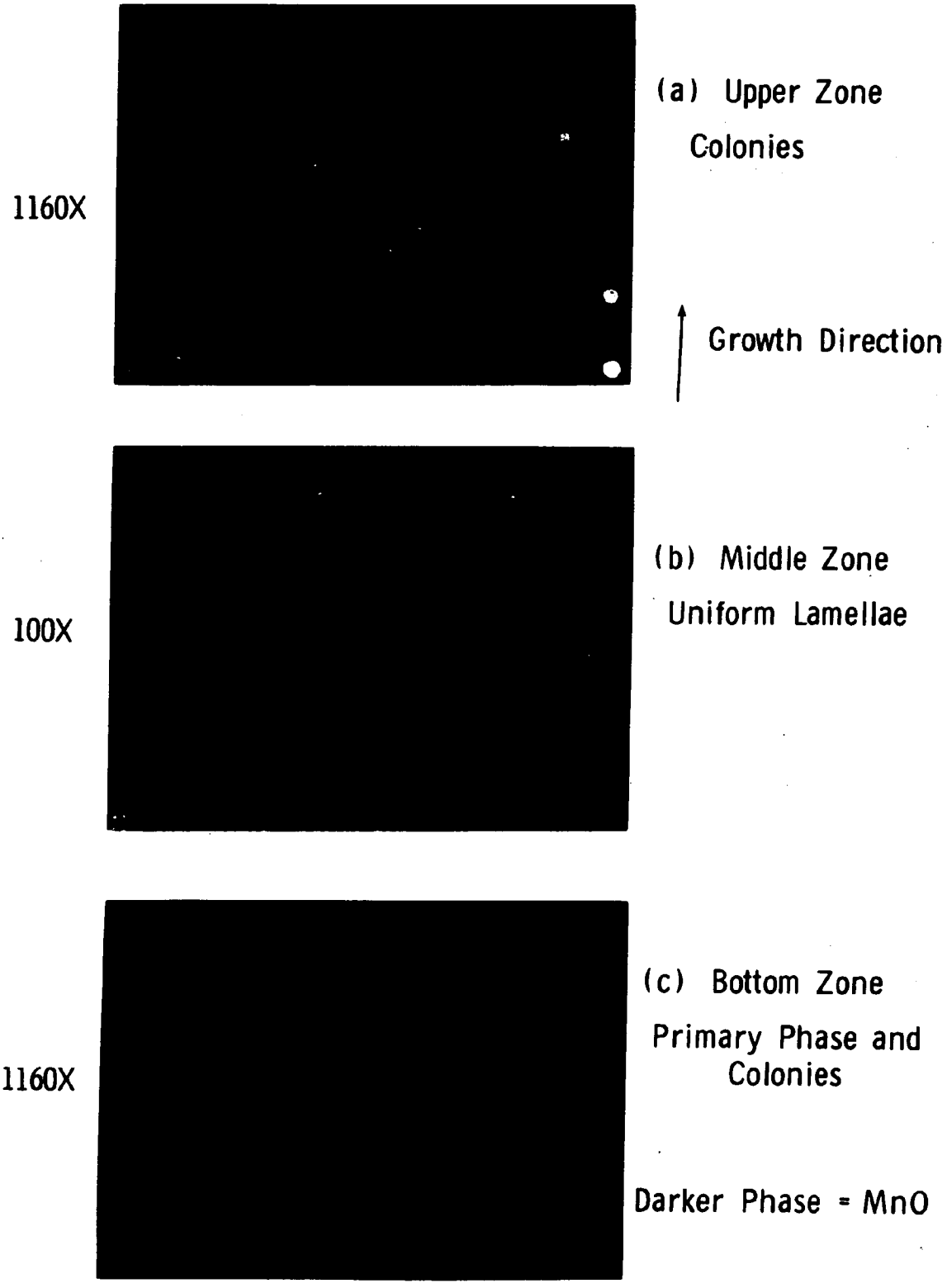
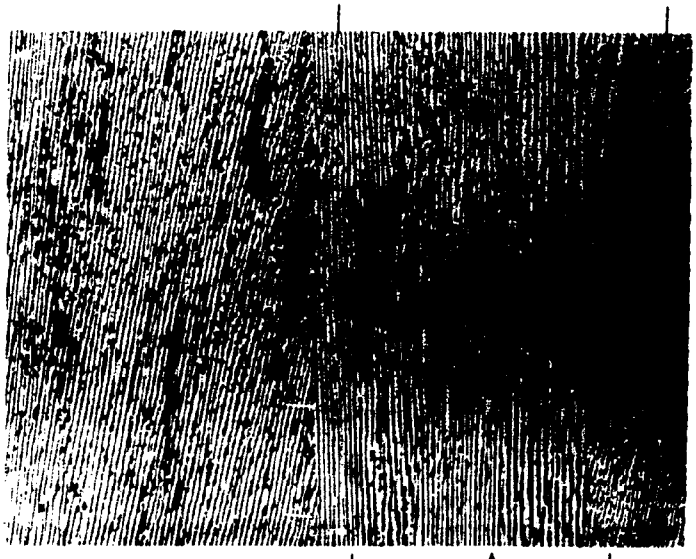
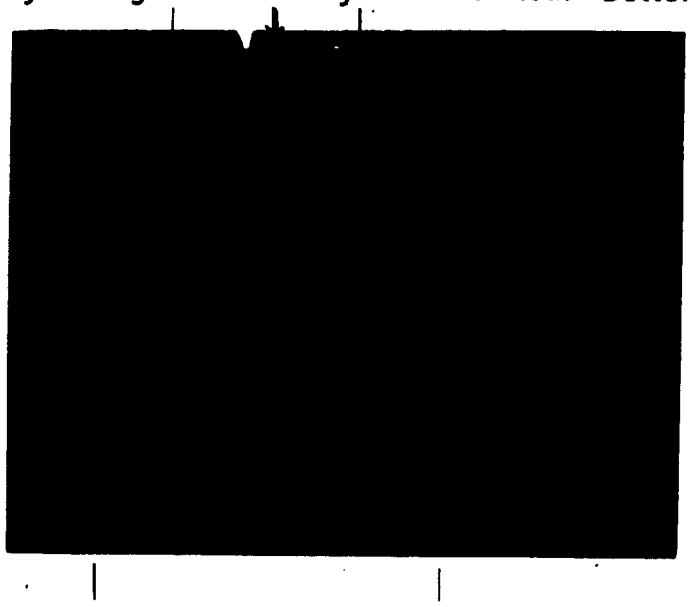


Figure 21. Colony development along MnO-MnS eutectic ingot.



(a) Favorably Oriented Grain Growing to the Exclusion of Others in Center of Ingot

(b) Colony being Excluded by Others Near Bottom of Ingot.



Growth Direction

Darkest Phase = MnO
Lightest Phase = Fe
Matrix Phase = MnS

Figure 22. Longitudinal section of grain and colony boundaries in MnO-MnS eutectic. 75X.

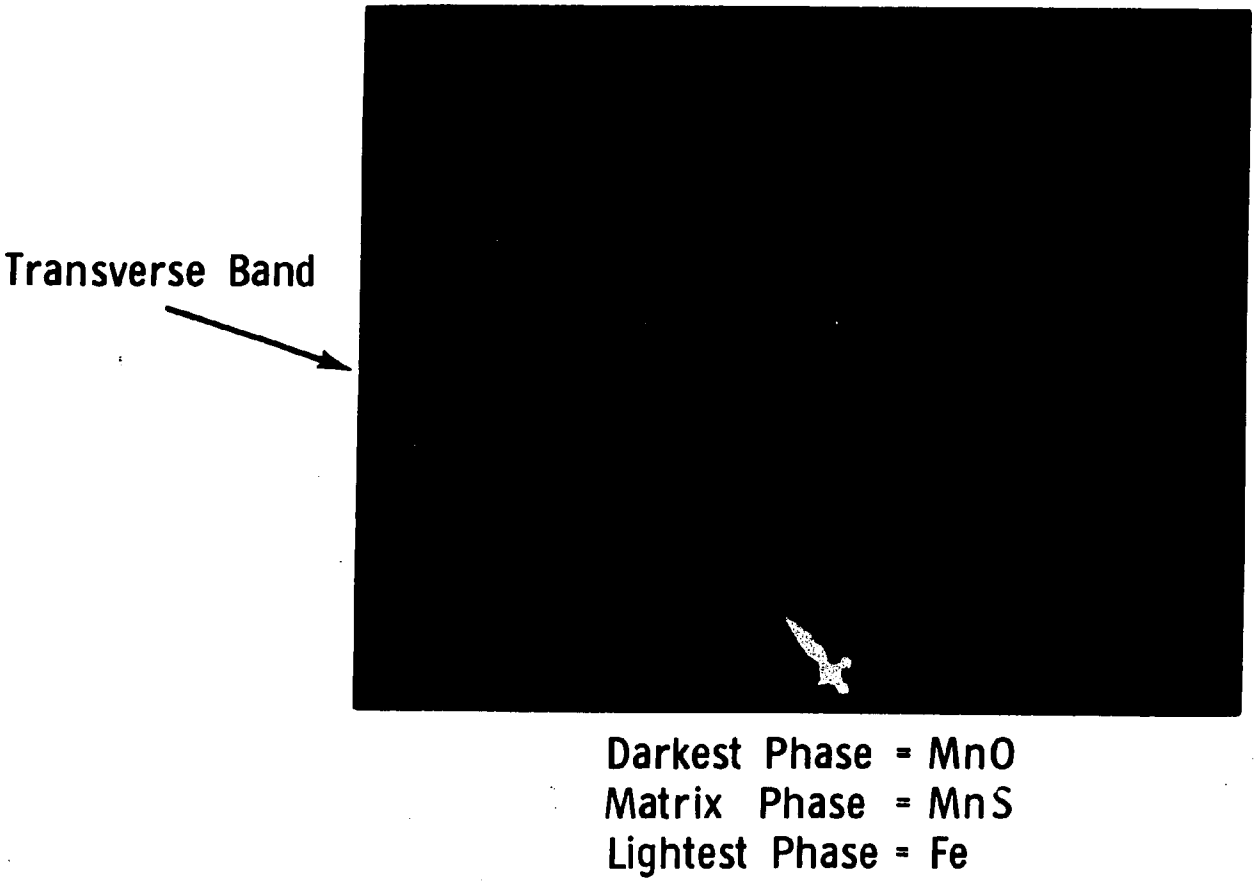
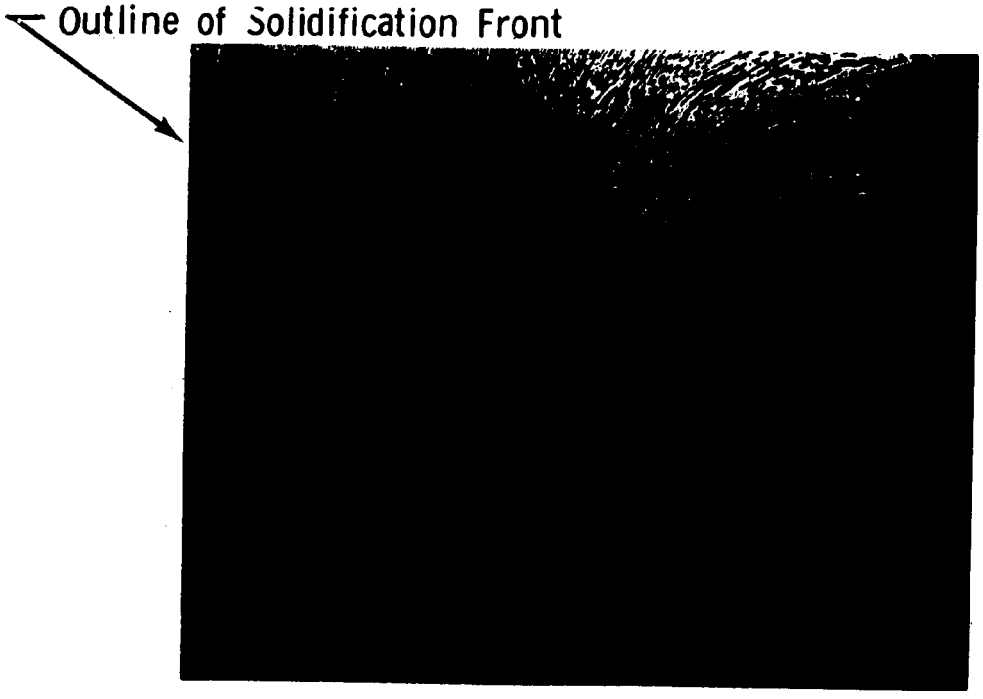


Figure 23. Longitudinal section of MnO-MnS eutectic ingot showing transverse band outlining domed solidification front. 100X.



(a) Transverse Section



(b) Longitudinal Section

Figure 24. Transverse and longitudinal sections of MnO-MnS eutectic ingots showing microstructure and outline of solidification front near crucible wall. 75X.

ingots made in this study may be due to thermal as well as impurity diffusivity effects. The thermal conductivity of iron and graphite is about 35 and 100 BTU/hr/ft^2/°F/ft, respectively, while the oxide-sulfide and alkali halide eutectics, which are relatively good insulators, would be expected to have much lower values. Thus, a radial temperature gradient probably exists along the ingot-crucible radius, causing the non-planar solidification front. The effect of the convex solidification front described above is to cause a slight longitudinal curvature of the eutectic grains and their lamellae towards the crucible wall. This curvature becomes more severe as the solidification front radius of curvature becomes smaller near the crucible wall (Figure 24).

The variation in the effect of a curving growth front on the lamellar-to-rod breakdown within a single colony cell is shown in Figure 25. The lamellae which extend radially to the boundary of the cell and thus must curve only within the plane of the lamellae evidently do not degenerate into the rod morphology as easily as do those which must curve in a direction normal to their plane. This seems to support the hypothesis that the low index coincident planes at the phase interface have such a reduced solid surface energy compared with any high index or complex boundary that they stabilize the lamellar structure even when a rod-like or globular morphology would permit reduction in interphase surface area. Thus, as long as the solidification front normal

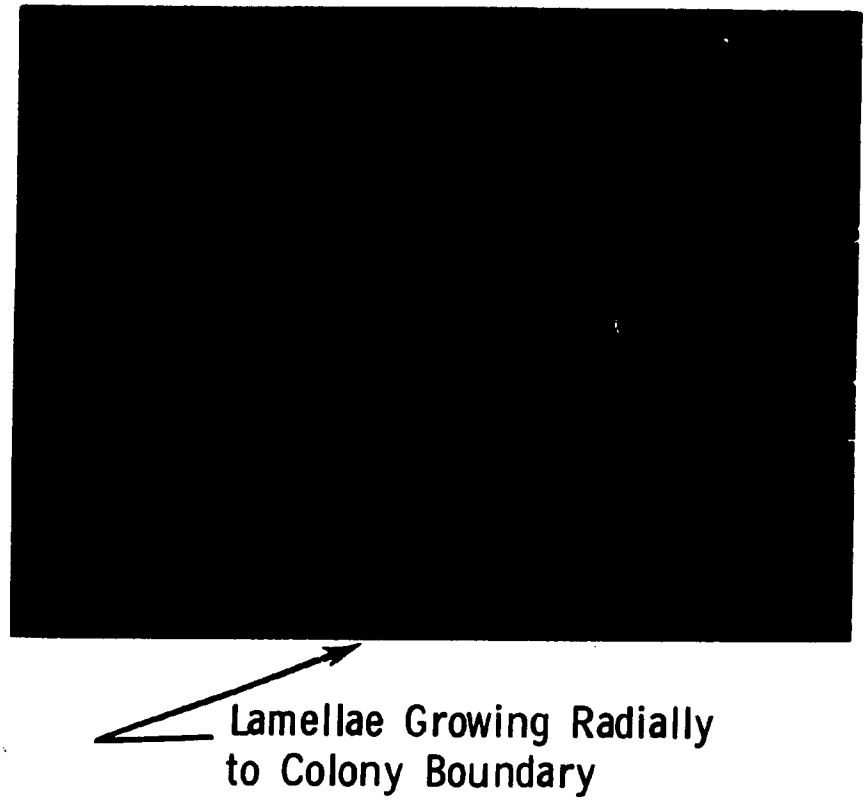


Figure 25. Transverse section of MnO-MnS eutectic colonies showing stability of lamellae growing radially to colony boundary. 150X.

remains in the plane of the lamellae, so that the low index phase boundaries are retained, there is no tendency for breakdown into the rod morphology. When the front normal bends sufficiently out of the lamellar plane, it apparently forces the interphase boundary away from the low index, low energy planes, and the total phase boundary energy can then be reduced by formation of the rod morphology which reduces the phase boundary area. This explanation agrees with the findings of Hunt and Chilton[45] that curvature of the solidification front around an obstacle causes the lamellar-to-rod transition if the curvature is in a direction normal to the plates but does not cause the transition if the curvature is in the plane of the plates. Chadwick's hypothesis[37] that the lamellar-to-rod transition at colony boundaries is primarily due to segregation of impurities to the boundaries by the radial component of diffusion from a colony cell tip is not supported by this data. Chadwick's impurity modification mechanism is not, however, refuted by the data. The geometrical effect seems to be the primary factor in the case studied here.

There also seemed to be a tendency for the lamellae in the grains around the periphery of the ingot cross section to become radially oriented (Figure 26), while the lamellar regions in the center of the ingot cross section retained a random orientation about the growth axis. This effect is probably related to the convex solidification front which would tend to favor grains with radially

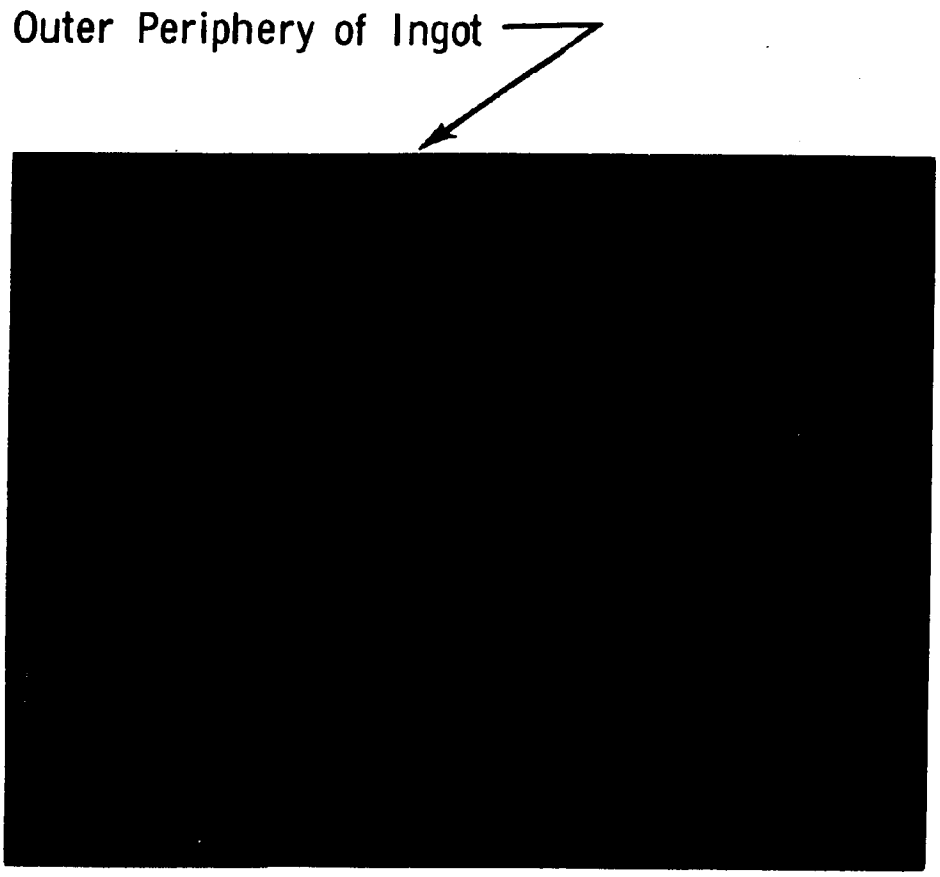


Figure 26. Transverse section of MnO-MnS ingot showing lamellae growing radially to the outer periphery of ingot. 75X.

oriented lamellae since they would be least disturbed by the radially curving growth pattern imposed by the convex front.

The overall microstructural appearance of all the completely solidified ingots showed the three characteristic zones observed by previous investigators[17, 32] in metallic eutectics: (1) an initial zone of many small, isotropic, randomly oriented grains caused by random nucleation, (2) a central zone of increasingly fewer elongated grains of well developed unidirectional structure, and (3) a final region of marked colony formation caused by impurity segregation to the end of the ingot. Some typical cross sections of these three regions are shown for the MnO-MnS eutectic in Figure 21.

c. Irregularities

Irregularities observed in the eutectic microstructure of the MnO-MnS ingots include dendrites of the primary phases, voids and iron particles.

Primary dendrites of MnO, MnS and Fe were observed in various parts of the MnO-MnS ingots melted in Ferrovac iron crucibles (Figure 27). Typical branched appearances were noted for all three materials. A fairly thick halo of MnS appears around the MnO dendrites (Figure 27a), while only a thin, discontinuous halo of MnO appears around MnS dendrites (Figure 27b). Sundquist et al[123] have studied the relationships between dendritic halos and relative undercoolings of hyper- and hypoeutectic metal alloys. In a previous study[52] they concluded that eutectic solidification

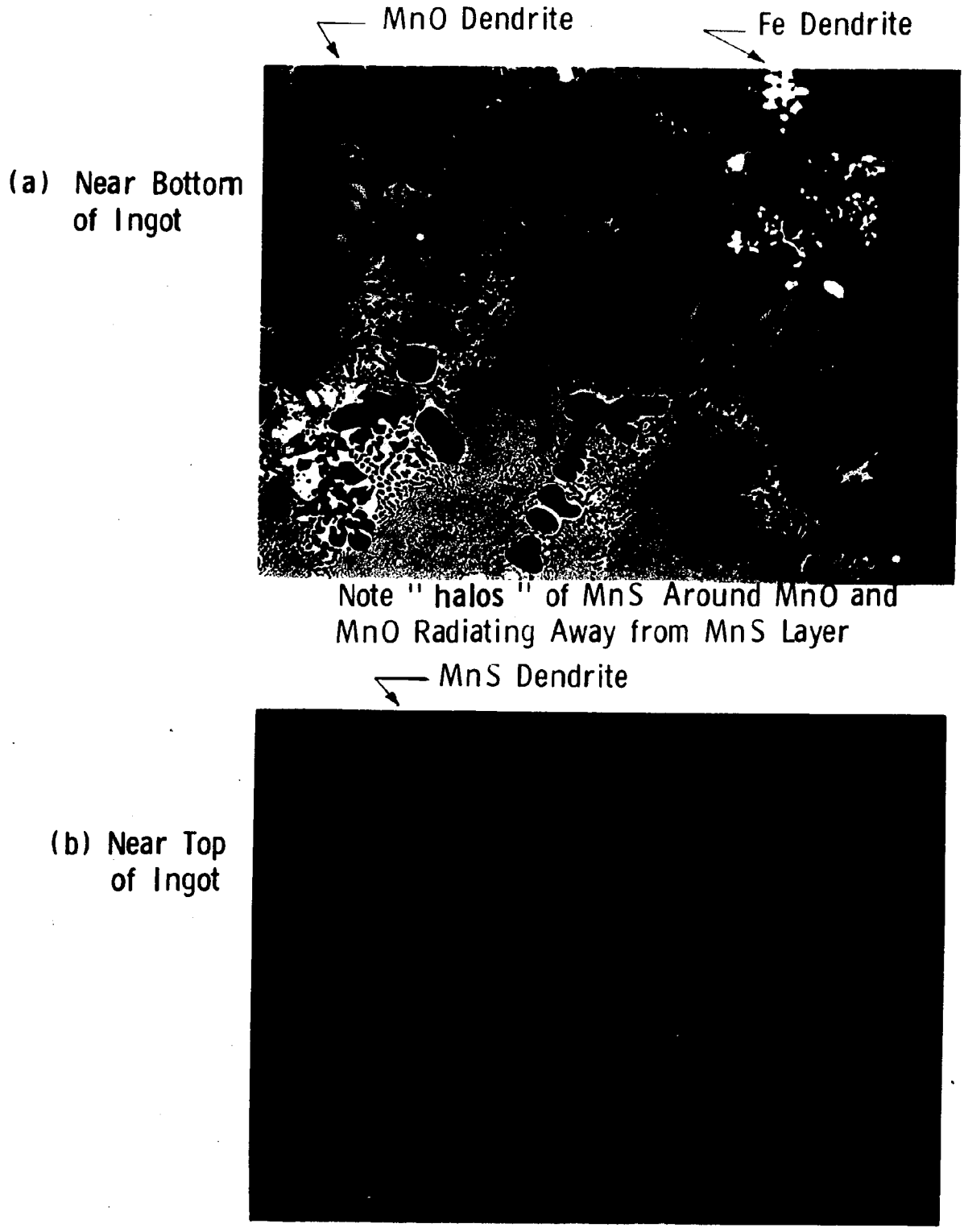


Figure 27. Dendrites of MnO, MnS and Fe in transverse sections of MnO-MnS eutectic ingots. 100X.

would occur at a low undercooling in the presence of primary particles of only one of the two phases in most binary eutectics. This indicates that only one of the two phases can nucleate the eutectic in the absence of impurities. They correlated the presence of thick halos of the second phase around primary dendrites of the first phase with large undercoolings, and thin or discontinuous halos with small undercoolings. Thus, primary MnS must cause the eutectic to nucleate at less undercooling than MnO, indicating that MnS is the primary nucleating phase. Sundquist et al[123] also noted that the eutectic radiates away from primary particles of the nucleating phase but not from those of the other phase. Continuous eutectic rods or lamellae radiate from the MnS particles but not from MnO particles in the random zone at the beginning of MnO-MnS ingots (Figure 21a). It is concluded that MnS nucleates the MnO-MnS eutectic and that MnO does not.

In addition to the branched MnS dendrites a second form was observed. These consisted of a single thin disc oriented with its radius generally in the growth direction. Sometimes they contained a thin, dark central line which could be a plate of MnO (Figure 28).

MnS dendrites of both types were segregated to the upper portions of the ingots, while MnO dendrites were segregated to the bottoms of the eutectic ingots. The formation of primary dendrites of both eutectic end-members in the same ingot could be explained several ways. The two

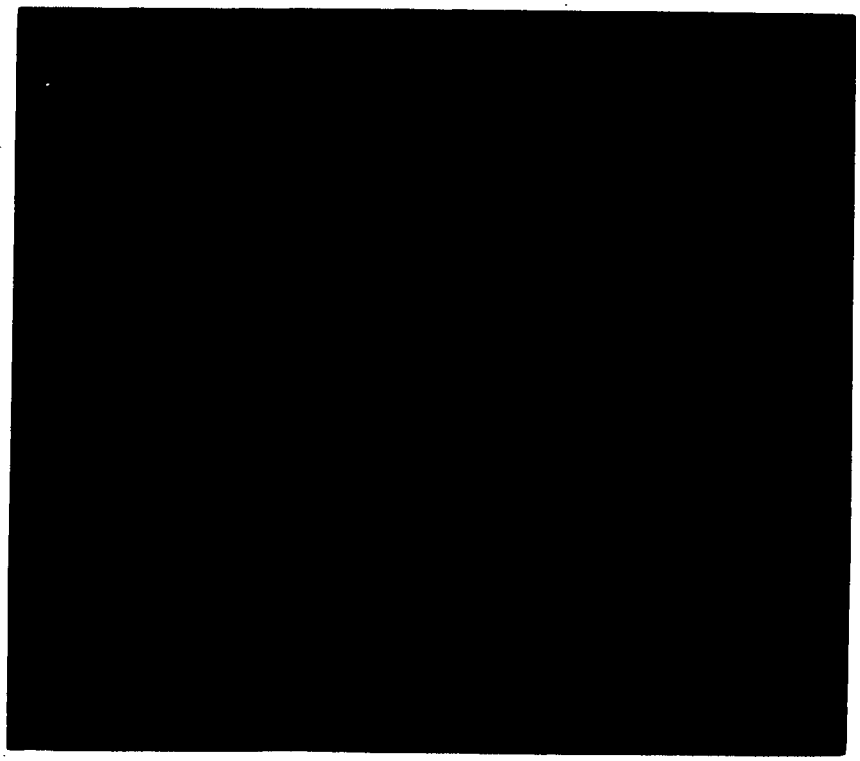


Figure 28. Pronounced colony structure and MnS "discs" in transverse section at top of MnO-MnS ingot. 25X.

primaries could form in different regions of the melting eutectic mixture due to inadequate mixing of the pure powder phases and insufficient subsequent mixing of the nominally eutectic liquid. They could also form at different times in the solidification process due to differences in the effects of impurities on the two phases and in impurity levels in the melt as solidification proceeds. On the other hand, the observed distribution could be the result of segregation of previously formed dendrites. Mechanisms for such segregation have been summarized by Davies:[124]

> 1. "Differences in the density of the solid dendrite and the liquid, i.e., a gravity effect.
>
> 2. "Convective stirring caused by temperature gradients in the liquid.
>
> 3. "A surface energy gradient effect such as that reported by Kawai and Keller in explanation of discrepancies in density measurements of polymer single crystals."

Kawai and Keller[125] have shown that a particle will come to rest in a liquid where a surface energy gradient caused by temperature or composition variations exists at the level where the forces due to gravitational and interfacial free energy balance. The surface energy effect becomes significant when the surface-to-volume ratio of the particles is large. The platelike MnS dendrites at the top of some of the MnO-MnS ingots have diameter to width ratios of 100/1 with a high inherent surface-to-volume ratio. This effect has not been quantitatively evaluated here, but Davies[124] has shown that it could be significant in segregation effects in copper-tin alloys. The MnS plates are

almost all oriented with their long axis parallel to the growth direction, supporting the above hypothesis since this is the direction of both the composition and temperature gradients.

Cole and Winegard[126] have considered the effects of both thermal and solute convection on macrosegregation in unidirectionally solidified alloys. Solute convection is caused by inherent density differences between alloy constituents in the liquid, while thermal convection is due to local density inversions caused by temperature variations in the liquid. Thermal convection should be minimal in vertical solidification from the bottom to the top of an ingot since the positive temperature gradient should not tend to cause convection currents. In the experiments in this study a positive temperature gradient existed at the solidification front. A negative gradient, however, might exist above that. This could have induced convective stirring and interacted with the inherent density differences of the phases or with solute convection to give the macrosegregation observed. According to Cole and Winegard's[126] analysis, the high temperature gradients and low solidification rates used in this study to minimize the microsegregation caused by cell formation would tend to promote macrosegregation by thermal-solute convection.

Many of the MnO-MnS ingots possessed a boundary layer at the crucible wall (Figure 24). This layer exhibited a coarse microstructure with a curvature away from the

crucible wall in some cases, indicating a curved solidification front (Figure 24).

Uniform distributions of small iron globules and fibers occurred in some regions of the MnO-MnS eutectic ingots (Figures 19 and 24). The fact that the fibers and strings of globules appeared to be oriented with the growth direction of the eutectic indicates that they are probably solidifying simultaneously with the eutectic phases at the same solidification front. Some iron of the crucible would be dissolved very rapidly in the eutectic liquid formed above 1232°C since the melting point of the iron is only 1535°C. The iron particles appear to lie primarily in the MnS phase but are almost always adjacent to MnO particles. This might indicate that an Fe-MnO phase boundary has a lower energy than an Fe-MnS phase boundary.

The ingot region where the iron, MnO and MnS phases solidified together could be considered a ternary or three component metal-ceramic eutectic. The presence of some of the iron phase as fibers elongated in the growth direction suggests eutectic solidification as a method of creating a metal fiber reinforced ceramic in which the metal fibers would be uniformly distributed and oriented in the ceramic matrix. This is difficult to achieve by mechanical dispersion of fibers. In addition, the metal fibers should tend to place the ceramic matrix in compression below the eutectic temperature since the thermal coefficients of metallic phases tend to be higher than those of ceramic phases

(Figure 33).

It appears, however, that the iron particles may be the cause of, or at least tend to associate with, flaws in the lamellar microstructure (Figure 29). They also tend to segregate at grain boundaries (Figure 30) and transverse bands (Figure 23).

Small spherical voids were usually present in both phases of the MnO-MnS eutectic (Figures 12 and 21b). The voids tended to occur in the MnS phase but adjacent to MnO phase particles. This might be caused by vacancies and small voids being squeezed out of the MnO phase as it is compressed by the MnS matrix during cooling due to the difference in thermal expansion of the two phases. Fewer voids are noted when a large number of iron particles are present, suggesting that iron might diffuse into the voids under certain conditions.

B. Property Relationships

1. THERMAL EXPANSION

The thermal coefficients of expansion of the individual phases in a eutectic ceramic composite are important since the phases must cool from the eutectic solidification temperature to room temperature, with maintenance of the structural integrity of the composite across the interphase boundaries, in order to form a useful material. The linear thermal expansion in percent of the manganese oxide (MnO) phase after Foex[109] is shown in Figure 31. Data for the



Lightest Phase = Fe
Matrix Phase = MnS
Darkest Phase = MnO

Figure 29. Iron globules associated with lamellar flaws in MnO-MnS eutectic. 500X.

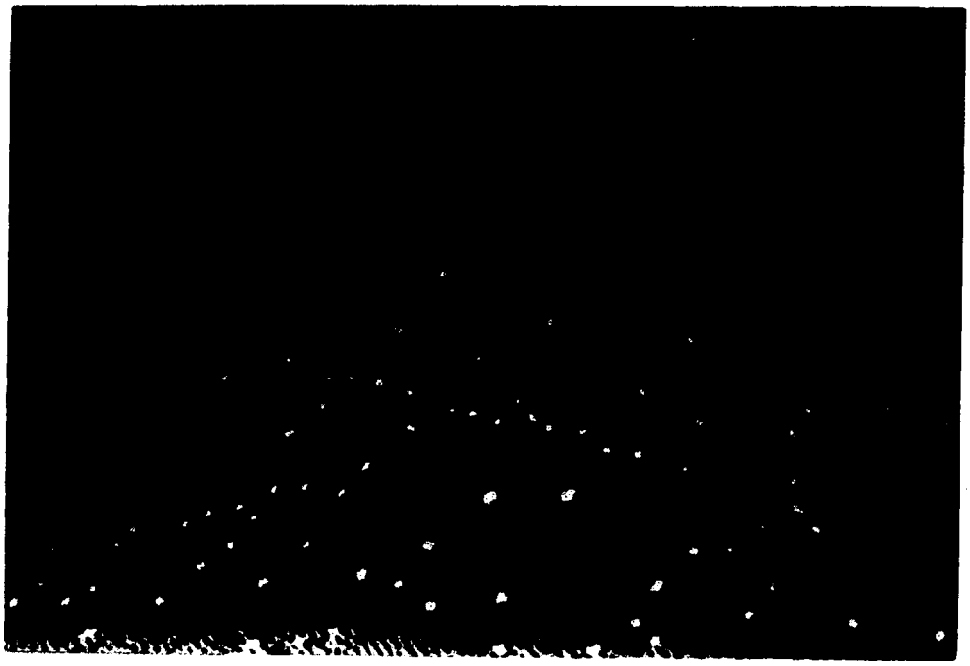


Figure 30. Iron globules segregated to low angle boundaries in MnO-MnS eutectic. Transverse section. 250X.

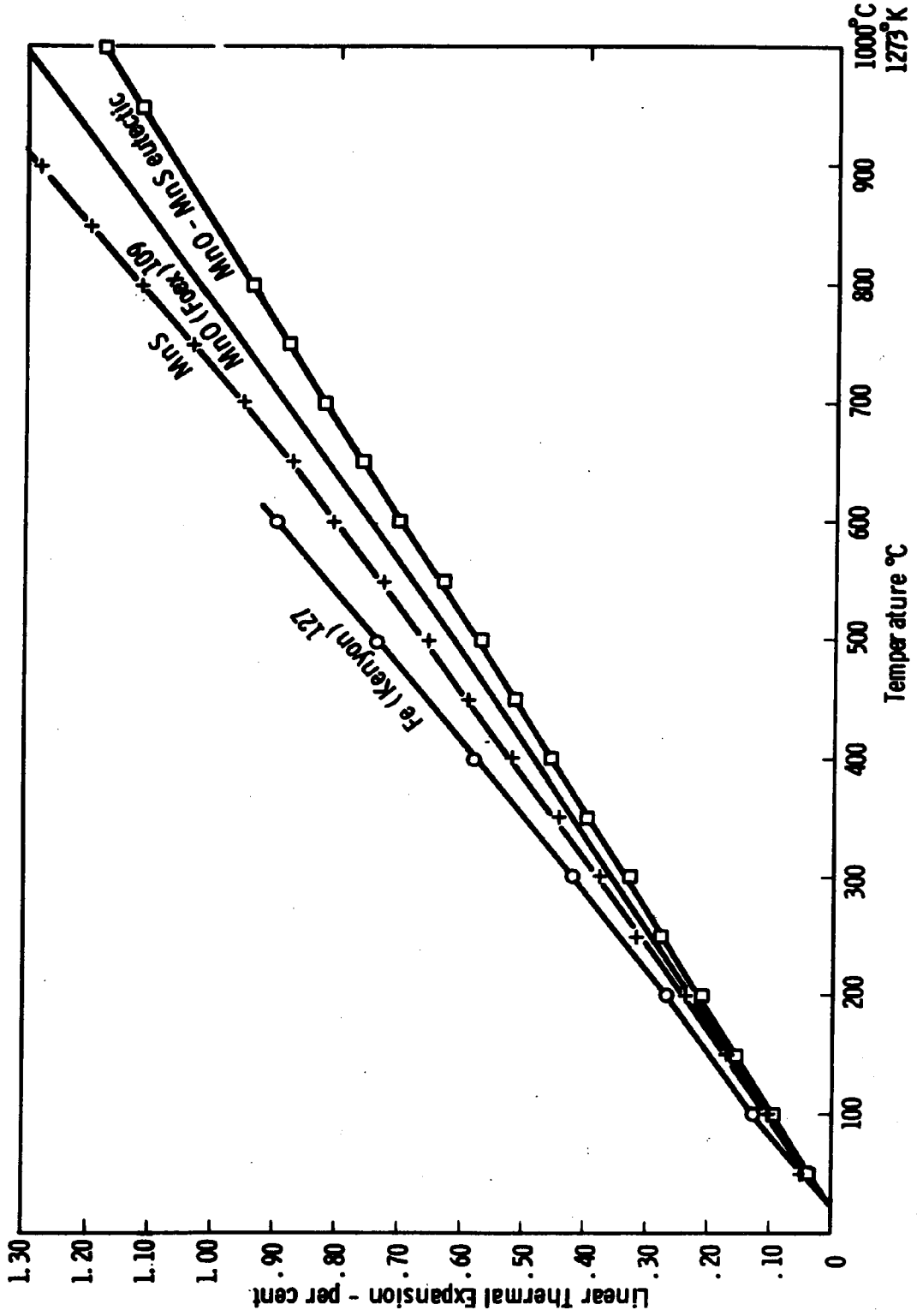


Figure 31. Linear thermal expansions for MnO, MnS, MnO-MnS eutectic and Fe from room temperature to 1000°C. Dilatometric data.

thermal expansion of MnS was not available in the literature, however, except for a narrow temperature region below room temperature. The change in lattice parameter of MnS with temperature determined by a back-reflection x-ray technique is shown in Figure 32 along with the data for the platinum standard used to calibrate the temperature[120] and the data of Foex[109] for MnO converted to a lattice parameter basis. The room temperature (25°C) lattice parameter of the MnO determined in this study was used to convert Foex's data to change in lattice parameter versus temperature. The percent linear expansion of MnS and of the MnO-MnS eutectic along with data for Fe[127] are also shown in Figure 31.

A fused silica rod dilatometer was used to measure the thermal expansion of the MnO-MnS eutectic ingots in the growth direction only. The expansion of polycrystalline MnS was also measured by this technique to assure that the two types of measurement were directly comparable. The expansion curve for the eutectic and for the polycrystalline MnS used to correlate the x-ray and dilatometric results are plotted in Figure 31 for comparison. The x-ray data indicate a value of $15 \pm 1.0 \times 10^{-6}/°C$, while the dilatometer data indicate a value of $14.5 \pm 0.5 \times 10^{-6}/°C$ for the thermal expansion coefficient of MnS over the range from 25 to 1000°C.

The estimate of precision for the x-ray data is based on a possible 2θ angle measurement error of $\pm 0.02°$ for the platinum temperature standard and a variable factor for the

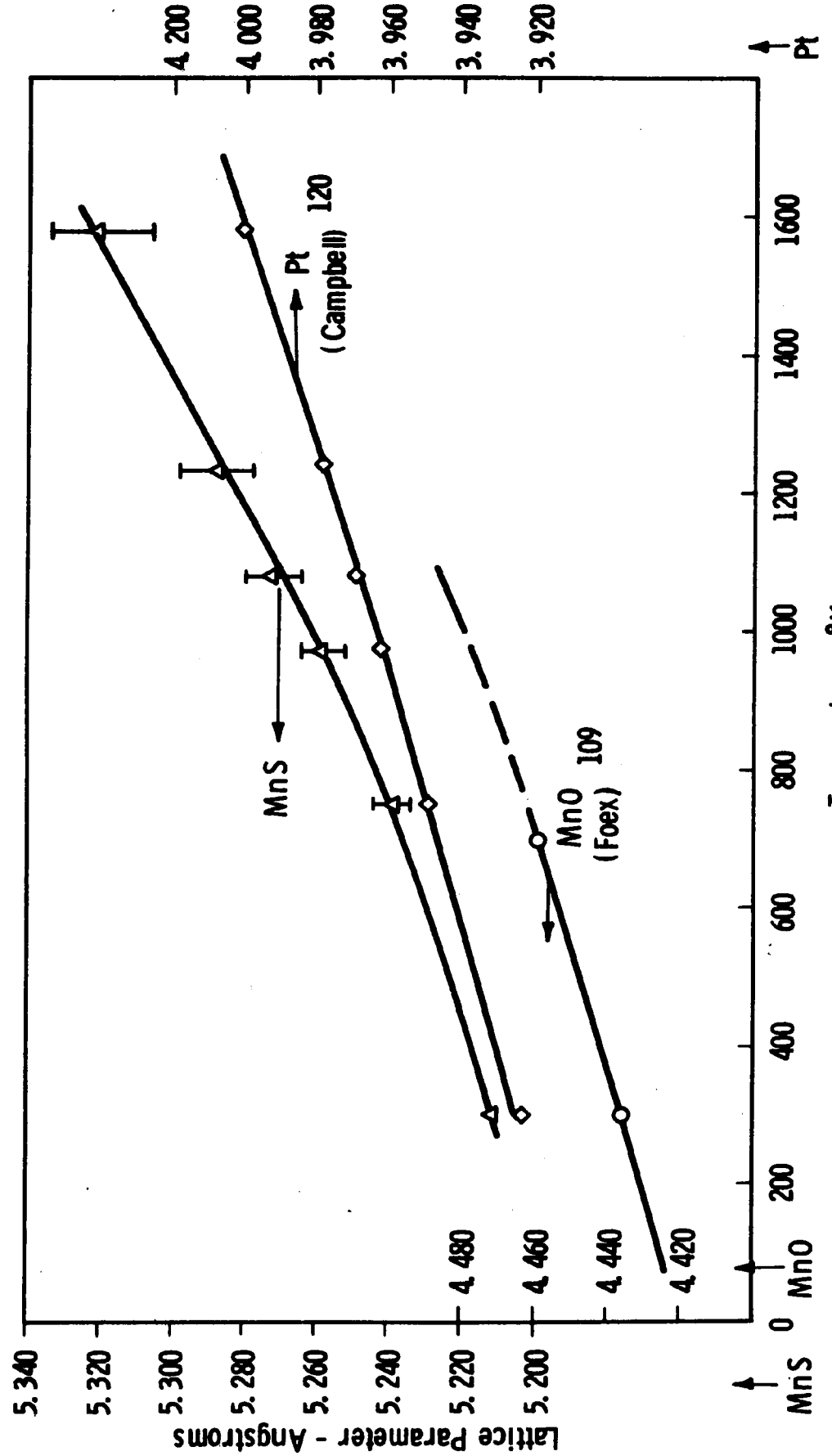


Figure 32. Lattice parameter versus temperature for MnS, MnO109 and Pt.120

uncertainty of identification and measurement of the diffraction lines at the higher temperatures for the MnS phase. This was due to the severe broadening of the MnS lines and the presence of additional phase lines as the temperature and time at temperature increased.

The mean thermal coefficient of the MnO-MnS eutectic between 25 and 700°C was found to be $12 \pm 0.5 \times 10^{-6}/°C$ by the dilatometric method. The data of Foex[109] indicate that the value for MnO is $13.5 \times 10^{-6}/°C$ over this same range. Thus, the MnO-MnS eutectic exhibits a lower thermal coefficient than MnS, as would be expected, but also a lower value than that of MnO, which would not be expected if Foex's data is correct.

Several models have been proposed for predicting the thermal expansion of a multiphase composite:[128] a linear mixture equation, Turner's equation,[129] and Kerner's equation.[130] The linear equation assumes a linear volume fraction (V_i) relationship between the thermal expansion of the composite (a_c) and its component phases (a_i):

$$a_c = \frac{\sum_i a_i V_i}{\sum_i V_i}$$

Turner takes into account the difference in bulk modulus of the component phases:

$$a_c = \frac{\sum_i \frac{a_i P_i K_i}{d_i}}{\frac{P_i K_i}{d_i}}$$

where a_c and a_i are the linear expansion coefficients of the composite and the i-th phase, P_i is the weight fraction, K_i is the bulk modulus, and d_i is the density of the i-th phase. Thus, Turner's equation reduces to a volume fraction relation for phases with the same bulk moduli and to a weight fraction relationship for phases of the same modulus to weight ratios. Kerner's equation includes the volume fraction, V_i, shear moduli, G_i, and bulk modulus, K_i, of the included phases, the composite K_c, and the matrix, K_m:

$$a_c = \sum_i a_i V_i + 4\frac{G_i}{K_c} \sum_i \left[\frac{K_c - K_i}{4G_m + 3K_m} (a_m - a_i) V_i \right]$$

Unfortunately, modulus data are not available for MnS or MnO, but Gilman[81] has shown that the shear compliance, C_{44}, for NaCl-type crystals varies logarithmically with interatomic distance; therefore, the C_{44} value for MnO and MnS can be estimated to be 3.2 and 1.9 x 10^{11} dynes/cm^2 respectively. Assuming elastic isotropy where $(S_{11} - S_{12} - 1/2\ S_{44}) = 0$, the shear modulus, G, is equal to the shear compliance, C_{44}. Young's modulus, E, and bulk modulus, K, can be calculated, assuming Poisson's ratio, ν, of 0.3, from the relationships:

$$G = E/\{2(1 + \nu)\} \quad \text{and} \quad K = E/\{3(1 - 2\nu)\}.$$

A plot of the mean linear thermal expansion of MnS, MnO and the MnO-MnS eutectic between 25 and 1000°C versus atomic, weight volume, and stress equilibrium calculations of thermal expansion variation predicted by the above equations is shown in Figure 33.

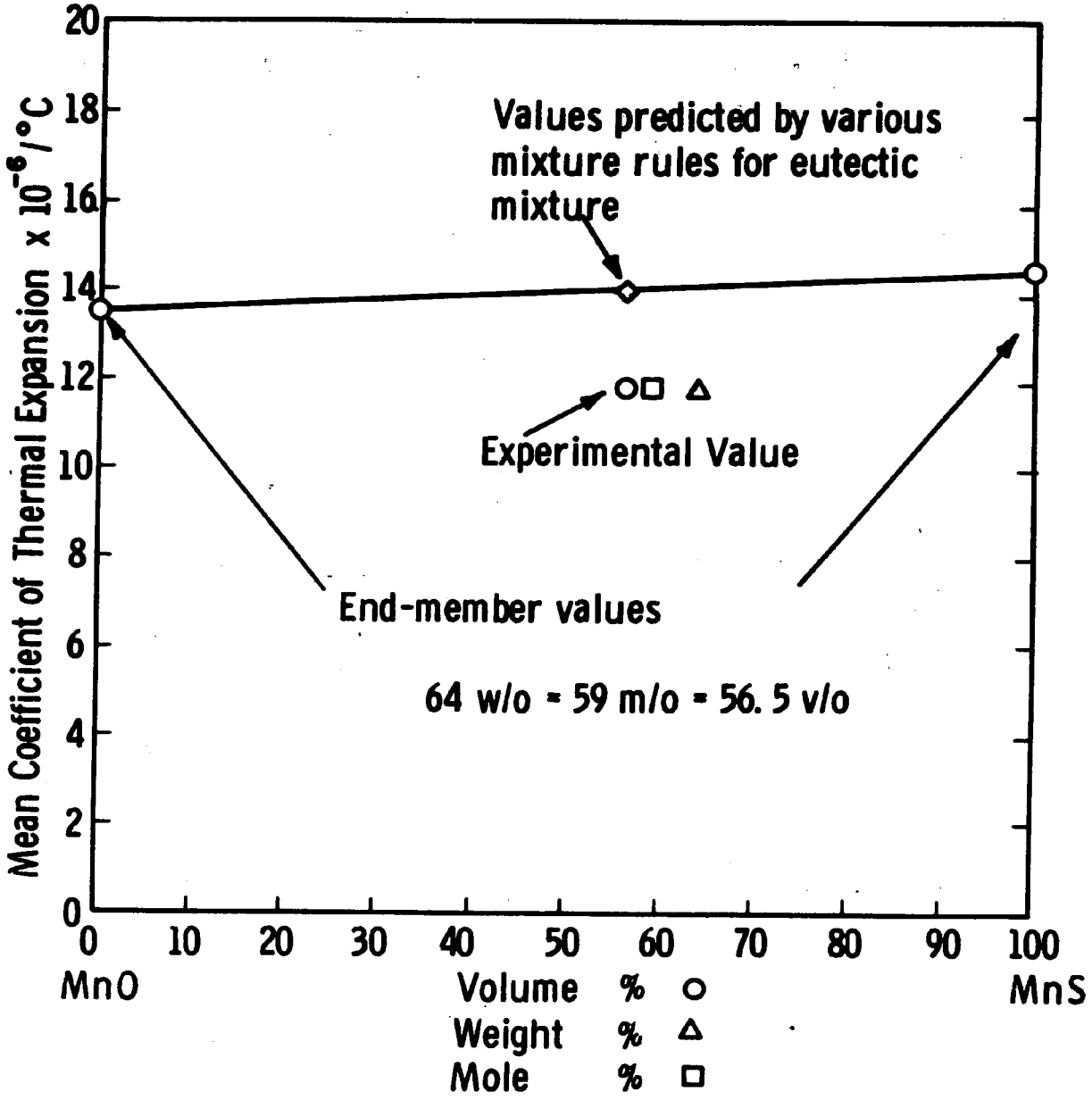


Figure 33. Experimental mean linear thermal expansion coefficients of MnO, MnS and the MnO-MnS eutectic compared with various calculated eutectic values.

The linear mixture rule line predicts a mean coefficient of 14.1 x 10^{-6}/°C for the eutectic. Turner's equation predicts a value of 14 x 10^{-6}/°C. Kerner's equation involves too many unknown quantities to permit evaluation for the MnO-MnS system. It appears, therefore, that the applicable mixture rules cannot be used to predict the low expansion coefficient observed.

The expansion measurements were made in an evacuated chamber which was constantly evacuated by a mechanical vacuum pump. The MnS specimen had a surface layer of oxidation product, and the eutectic specimen exhibited slight internal and external oxidation and coalescence of the MnO phase at colony boundaries on microstructural analysis subsequent to dilatometric testing. The dilatometric data of Figure 31 was obtained on the heating cycle, but no significant difference was noted in the cooling curve. Foex's data for MnO was assumed to be correct and was not checked in this study.

Rosenfield and Averback[131] have shown that elastic stresses can affect the apparent thermal coefficient of materials according to the relationship

$$\left(\frac{\delta\alpha}{\delta\sigma}\right)_T = \frac{-1}{E^2}\left(\frac{\delta E}{\delta T}\right)_\sigma ,$$

where α is the thermal expansion coefficient, σ is the elastic stress and E is the elastic modulus. For materials in which the elastic modulus decreases with increasing temperature, elastic stress effect should cause the expansion coefficient to increase under tension and decrease under compression. Thus, the coefficient of MnS would be

increased and that of MnO would be decreased under the stresses due to cooling in the eutectic composite. In Rosenfield and Averbach's work the coefficient of expansion of invar is decreased about 20% and that of 1020 steel increased about 5% at their elastic limits by this effect; therefore, it could conceivably cause an effect of the order of magnitude of that observed in the MnO-MnS eutectic if the decrease of the expansion coefficient of MnO were sufficiently greater than the increase effected in the MnS phase. Since the Young's modulus, E, of MnO would be expected to be higher than that of MnS, it would not be predicted that the change in α would be as great in MnO as in MnS.

It does not appear that extensive plastic deformation should occur at the small differential strains between the phases indicated by their similar expansion coefficients. Rosenholtz and Smith,[132] however, have shown that the linear thermal expansion of a polycrystalline solid can vary by a factor of 10 to 20 percent according to the amount of plastic strain caused or relieved by the previous thermal and stress history of the part. In particular, they found a sharp drop in thermal expansion in steel and magnesium when they were stressed just beyond the yield point and a more gradual decrease at large plastic strains. Hordon et al[133] also observed significant changes in thermal expansion with plastic strain in various aluminum alloys. They also observed changes in the elastic modulus in an inverse relationship to the thermal expansion changes, which they

attributed to pinning of mobile dislocations by solute and vacancy diffusion and annealing out of vacancies in small and large strain regions, respectively. Therefore, if there are even local regions of plastic strain in the eutectic solid, they could contribute to the decrease in thermal expansion of either or both phases and the resultant low total value observed for the eutectic.

The most likely causes of the anomolous behavior of the eutectic thermal expansion are the previously mentioned oxidation effect and the coalescence of the MnO rods at colony boundaries into large globules which were observed subsequent to dilatometric testing. These effects have not been analyzed quantitatively. However, the coalescence effect would be expected to cause differences in the measured thermal dilatation during the heating and cooling cycles. No significant difference was observed. The difference might have been masked by instrumental hysteresis, however. The oxidation of the MnS dilatometer specimen seems to be only on the surface, and its expansion value appears to be valid since it agrees with the x-ray determination. Manganese oxide is only stable in the presence of a significant partial pressure of oxygen above 500°C. Its equilibrium vacancy content is also a function of the oxygen partial pressure. The eutectic surface oxidation appeared to be primarily in the outer 0.001 inch layer of the MnS phase only.

2. DEFORMATION AND FRACTURE

The plastic deformation and fracture results obtained in this study are discussed in terms of their apparent relationships with the crystallography and microstructure of MnS, MnO and the MnO-MnS eutectic composite.

a. Crystallographic Effects

The deformation and fracture of MnS single crystals when indented on various crystallographic planes with a Vickers microindenter have been studied by Chao, Thomassen and Van Vlack.[64] They found that the primary glide system was $\langle 110 \rangle \{110\}$, as in most NaCl-type crystals. They also observed an unusual $\langle 110 \rangle \{111\}$ system subsequent to $\{110\}$ fracturing but no other secondary glide systems. The primary fracture mode for unconstrained MnS crystals was on $\{100\}$ as found in other NaCl types, but $\{110\}$ fracture occurred around indentations on $\{100\}$ surfaces and was attributed to the interaction of $(01\bar{1})$ and $(10\bar{1})$ slip near the surface. A minor amount of fracture occurred on $\{110\}$ planes at 90° to the $\{100\}$ indented surface. They also noted that a minor amount of MnO in the grain boundaries of polycrystalline MnS caused grain boundary fracture.

The deformation and fracture study for the MnO phase was performed on ground and polished or cleaved faces of a single crystal, flame-fusion grown boule obtained from Marubeni-Iida-America, Inc. The boule unfortunately had a relatively high percentage of a dispersed phase in a globular or dendritic form. The dispersed phase appeared lighter

than the MnO matrix in reflected light and was located primarily near the surface of the boule and in low angle boundaries (Figure 34). The dispersed phase probably does not greatly affect the plastic deformation and fracture modes around the Vickers indentations used in this study, however,

Vickers diamond pyramid indentations on a (100) surface of the MnO boule are shown in Figure 35. Slip traces parallel to <100> directions around the 10 kg indentations appear identical to those observed in MnS due to glide on {110} planes at 45° to the (100) surface.[64] As in MnS, a 45° rotation of the indenter does not affect the slip modes observed.

The slip lines around indentations on the (110) surface also were consistent with those observed in MnS and with the hypothesis of slip on {110} planes (Figure 36). Although some difficulties were encountered in polishing a {111} surface on the specimen available, the slip lines were visible and consistent with the {110} glide system. Since all slip lines observed on the {100}, {110} and {111} planes were consistent with {110} glide and no slip lines which indicated {100} or {111} slip were observed, it is concluded that {110} is the primary slip mode in MnO, at least in a constrained plastic field around a hard indenter. Some of the slip lines in the above figures can be observed to propagate through the dispersed phase particles without apparent change in direction. This might indicate that the particles have a similar crystal structure and that some of

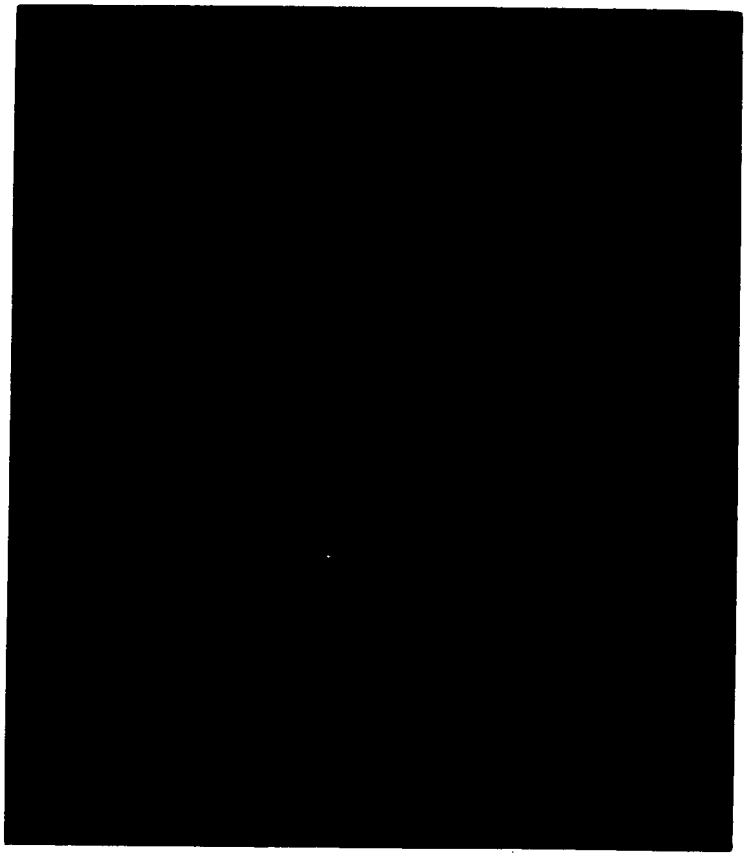


Figure 34. Dispersed phase particles in low angle boundary and kink in crack at Vickers indentation in MnO single crystal. 100X.

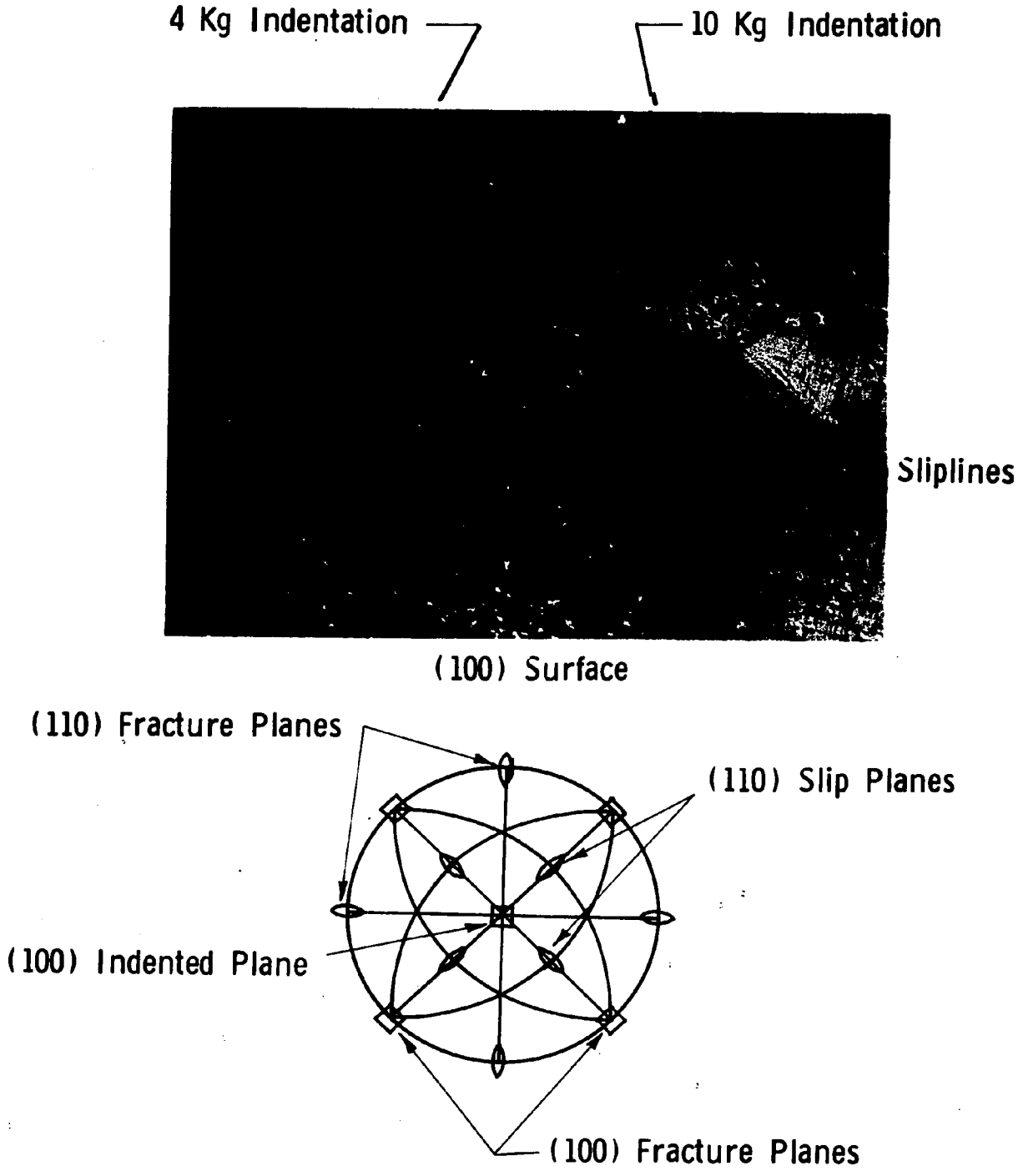


Figure 35. Slip lines and fractures around Vickers indentations on (100) surface of MnO single crystal. 100X. Oblique light.

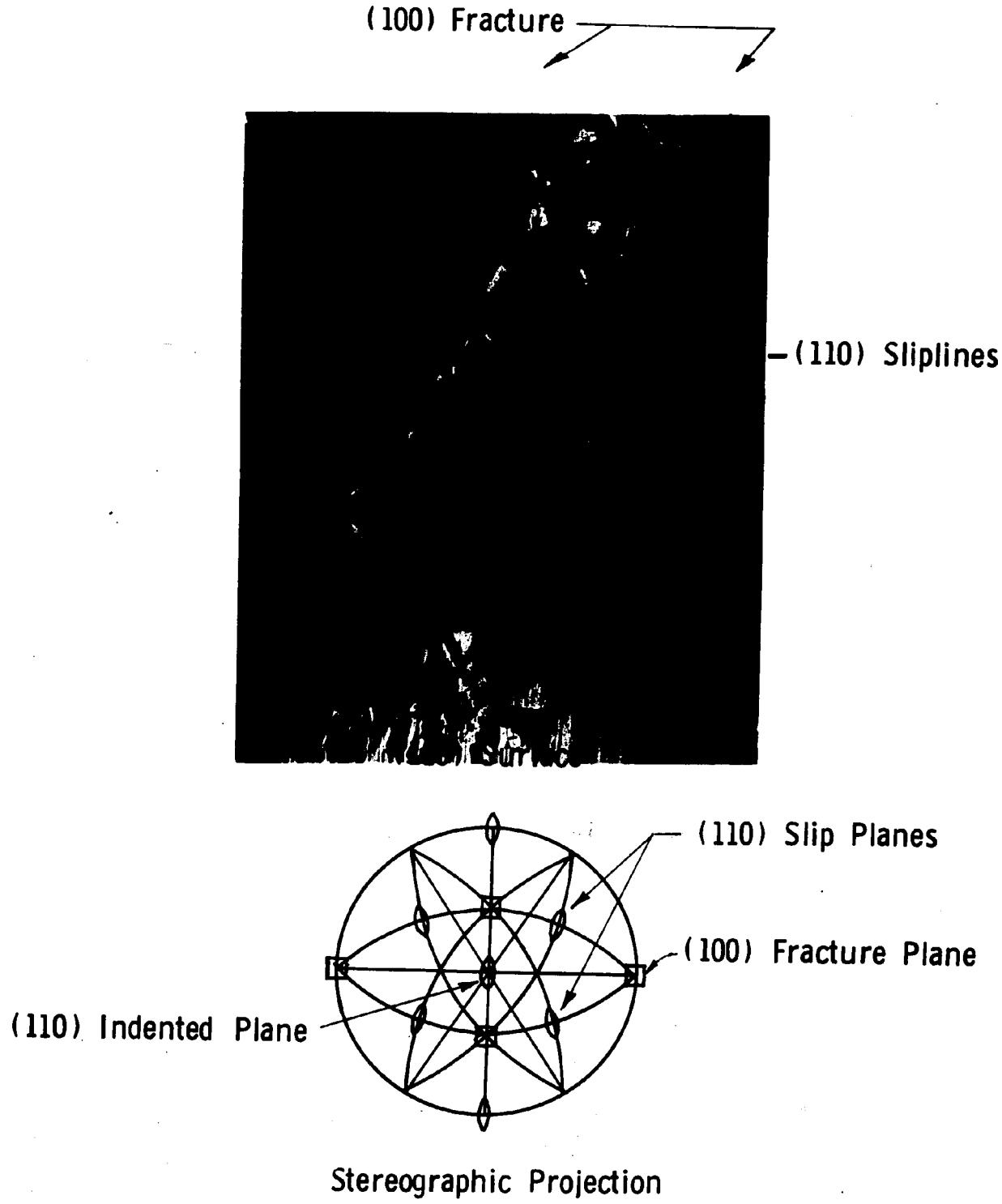


Figure 36. Slip lines and fractures around Vickers indentations on (110) surface of MnO single crystal. 100X. Oblique light.

them are crystallographically oriented with respect to the MnO phase. This hypothesis is further supported by the observation that the branches of the dendrites tend to be aligned in <110> directions throughout the matrix. Thus, the unknown phase is probably a cubic or tetragonal higher oxide of MnO with a higher index of refraction than MnO which causes its higher reflectivity. It also appears to be more brittle than MnO since large cracks appear in the particles ahead of even very fine slip traces in the matrix. The exact composition or crystal structure was not determined, however.

Several methods of etching the MnO were attempted, but it was not possible to produce visible etch pits on the surfaces tested.

The MnO boule fractured completely several times during indentation tests on various {100} or multiple {100} surfaces; therefore, it is concluded that primary fracture is by {100} cleavage as in most NaCl-type crystals, including MnS.

Fracture behavior of MnO during indentation on the various planes differed from that of MnS, however. At light loads (4 kg) only <100> cracks were observed on the {100} surface (Figure 35). Since this was not observed in MnS, there must be a significant difference in the relative ease of operation of the various fracture modes in the two systems. Since {100} cleavage is relatively easy in MnO and the above cracks occurred at low indenter loads, and thus

lower levels of plastic strain than the {110} fractures, it is postulated that the {100} cracks may be simple tension cracks rather than fractures caused by multiple slip interaction. In any case, a dislocation interaction mechanism to explain these cracks is not readily apparent. At larger plastic strains <110> fractures appeared in addition to the <100> cracks mentioned above (10 kg indentation, Figure 35). These cracks corresponded to those observed on {100} surfaces of MnS by Chao et al[64] and presumably are due to the same mechanism of interaction of $(01\bar{1})$ and $(10\bar{1})$ slip near the (001) surface in MnO. When both types of fracture occur around large indentations the <100> and <110> cracks tend to predominate on opposite sides in the indentation (Figure 35). This may be due to the fact that the indentation was not made exactly normal to the crystallographic plane, but it could also indicate that the initiation of one of the two types of fracture relieves the strains contributing to the other. The presence of dispersed particles may also interfere with the normal fracture behavior around an indentation. All the <110> cracks appeared significantly wider than the <100> cracks, but it is not clear why this occurred.

Fractures around indentations on the {110} surface were entirely on {100} planes, but the {110} slip was not as extensive around an indentation as on the {100} planes (Figure 36). The cracks parallel to the growth axis of the boule were also wider and longer with more branches and jogs

than those normal to the growth axis on this surface. This may be due to asymmetry of internal strain caused by the flame fusion growth process.

On the {111} surface very asymmetric fracture patterns were obtained. Again, this may have been due to the asymmetric indentations on the small and somewhat non-planar surface available. However, those indentations with the points of the Vickers diamond in the <110> directions gave primarily <110> cracks, while those with their points in the <100> direction gave primarily <100>. Some of both types of crack, however, are observable around all the indentations. Since all the cracks observed were consistent with either {110} or {100} cleavage, it can be concluded that these are the two primary modes of fracture under the constrained conditions of the indentation test for MnO and that the occurrence of one tends to suppress the other.

b. Microstructural Effects

Vickers indentations were also made on the transverse $(11\bar{2})$ and longitudinal (110) and (111) sections of the lamellar MnO-MnS eutectic regions. The purpose of this study was to determine how the oriented lamellar microstructure might affect the slip and fracture patterns, especially around a Vickers pyramid indenter compared with the results on single crystals of the two phases.

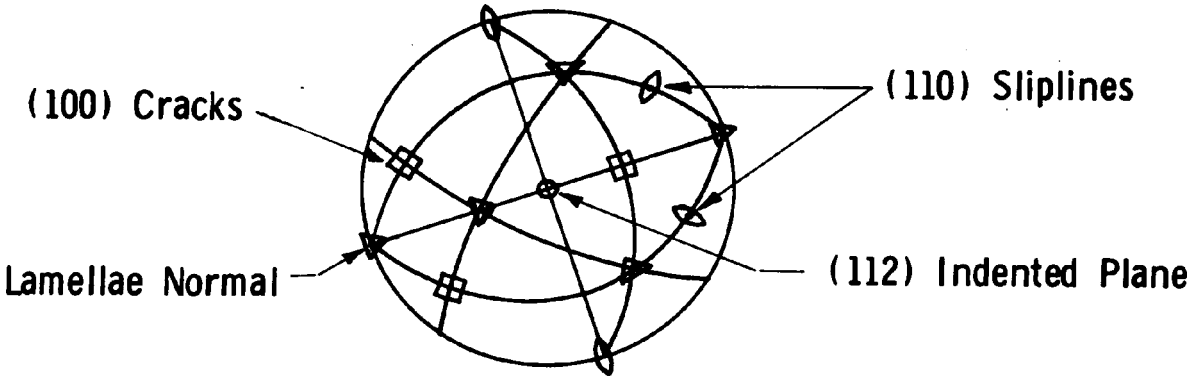
The first observation was that fracture tended to propagate along the (111) interphase boundary when indentation was performed near a free edge of a specimen or when

cleavage with a sharp blade was attempted. This effect was used to advantage in the preparation of x-ray precession specimens and was observed in all the eutectics in which orderly lamellar regions existed. The cleavage path was entirely in the MnO phase adjacent to the MnS boundary in all MnO-MnS cases checked. Indentations at sufficiently light loads and in the interior of transverse $(11\bar{2})$ cross sections where a more symmetric constraint was present exhibited less (111) fracture and more (100) fractures (Figure 37). Indentations on (111) surfaces normal to the lamellae did not show cracks (Figure 38). Indentations on longitudinal (110) surfaces caused fractures primarily at the interphase boundaries in a $[11\bar{2}]$ direction (Figure 38), although for a heavier indenter load a crack in a [111] direction normal to the lamellae was observed. This latter type of crack might be due to the interaction of (011) and $(10\bar{1})$ slip near the (110) indented surface (Figure 38). The cracks observed in the eutectic composite in many cases were very complex with many jogs across lamellae joining short sections along lamellar boundaries, but a consistent change in direction between phases was not observed.

Slip traces at about 66° to each other were observed on the transverse $\{112\}$ surface which corresponded within the angular variation of the lamellae to $(10\bar{1})$ and $(0\bar{1}1)$ slip planes (Figure 37). There were no noticeable slip lines around indentations on the (110) or (111) surfaces. The slip lines on the transverse surface were very straight



(112) Surface



Stereographic Projection

Figure 37. Slip lines and fractures around Vickers indentations on $(11\bar{2})$ surface of MnO-MnS eutectic. 100X. Oblique light.

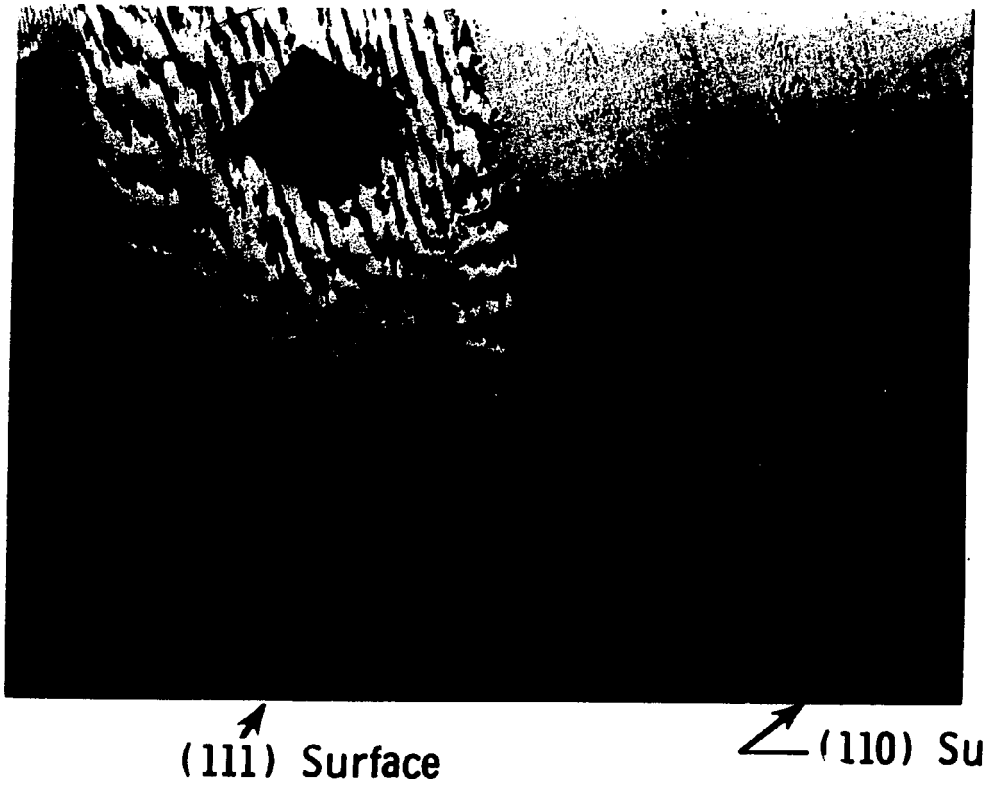


Figure 38. Vickers indentations on (111) and (110) surfaces of MnO-MnS eutectic. 100X.

and apparently not affected by crossing the lamellar phase boundary.

The above results indicate that the plastic deformation of the MnO-MnS eutectic results primarily from slip on {110} planes and is relatively unaffected by the necessity of operating through two different phases and their phase boundary. The fracture behavior seems to be more significantly altered by the two phase composite since a fracture mode along the phase boundaries is observed in addition to {100} fracture as in the MnO and MnS single crystals. No well defined {110} fracture was observed in the eutectic microstructure.

3. HARDNESS

The hardness results obtained in this study are discussed in this section in terms of their variation with crystallographic and microstructural orientation.

a. Crystallographic Effects

The variation in hardness with orientation of the Knoop indenter on the (111), (110) and (100) planes of single crystal MnS has been reported by Chao, Van Vlack, Oberin and Thomassen.[80] Since MnS with a maximum of 1.8% oxygen in solution is one of the major phases of the MnO-MnS eutectic, their results are replotted in Figure 39 for comparison with the MnS and MnO-MnS hardness.

The variation in hardness with direction on the (111), (110) and (100) planes of single crystal MnO has been

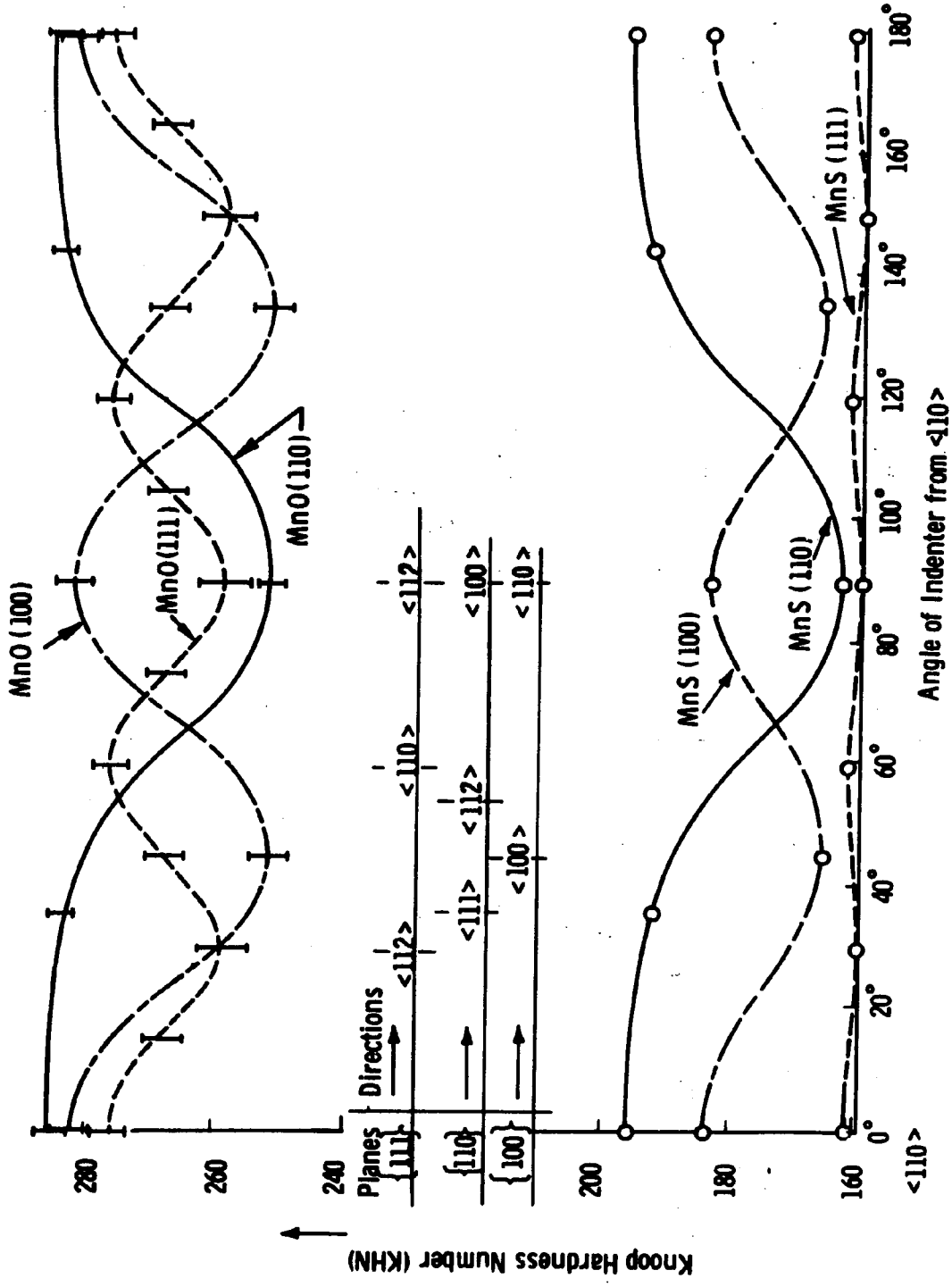


Figure 39. Crystallographic variations in Knoop Hardness Number (KHN) for MnO and MnS80 single crystals.

determined in this study, and the results are also plotted in Figure 39. Figure 39 was constructed from this data with the assumption of six-fold symmetry on a (111) plane, two-fold symmetry on a (110) plane and four-fold symmetry on a (100) plane. These symmetries have been observed in all previous hardness studies on NaCl-type crystals.[88] Hardness indentations taken at random orientations between the low index directions on each plane all gave values intermediate between the highest and lowest of the low index values, indicating that the data reported in Figure 39 include the maxima and minima on the planes tested. The hard directions on each plane of MnO also corresponded with the hard directions on the same planes of MnS, suggesting that the controlling plastic deformation modes are probably the same in both materials. This would be expected since their crystal structures and bonding are the same type.

The following differences between the relative hardnesses of the two single crystals can be observed in Figure 39:

1. The hardness of MnO is significantly higher than that of MnS for all planes and orientations. This is as expected since Wooster[107] has shown that in an isomorphous structural series of compounds, the hardness generally increases with melting point, and MnO has a higher melting point (1830°C) than does MnS (1620°C).

2. The hardness on the (111) plane of MnO varies

more than that of MnS (± 8 KHN for MnO, ± 1 KHN for MnS) and is relatively higher compared with the (110) and (100) plane hardnesses than is the (111) hardness in MnS. (KHN refers to Knoop Hardness Number.)

The MnO-MnS eutectic hardness was definitely determined on only the longitudinal (110) plane in the [11$\bar{2}$] and [111] directions, the interfacial (111) plane in the [110], [110] + 45° and [11$\bar{2}$] directions, and the transverse (11$\bar{2}$) plane in the [110] and [111] directions of the lamellar ingot regions. Therefore, from a crystallographic standpoint, the Knoop hardness on these planes with the long axis of the indenter oriented in these directions is all that can be compared between the single crystals and the oriented eutectic polycrystals. For this reason only the hardness on the (110) and (111) planes of single crystal MnO and MnS are plotted for comparison with the eutectic data in Figure 40. In the MnO and MnS single crystals, the Knoop hardness is lower when the long axis of the indenter is aligned in a <100> direction than when it is aligned in a <110> direction on the {110} surface (Figures 39 and 40). Measurements at intermediate indenter orientations gave hardness values intermediate between the [100] and [110] values; therefore, it was assumed that these represent the minimum and maximum hardness directions on the (110) surface. A significant sampling of hardness values was taken at <111> orientations intermediate between <110> and <100> directions for plotting in Figures 39 and 40. The hardnesses in the <111>

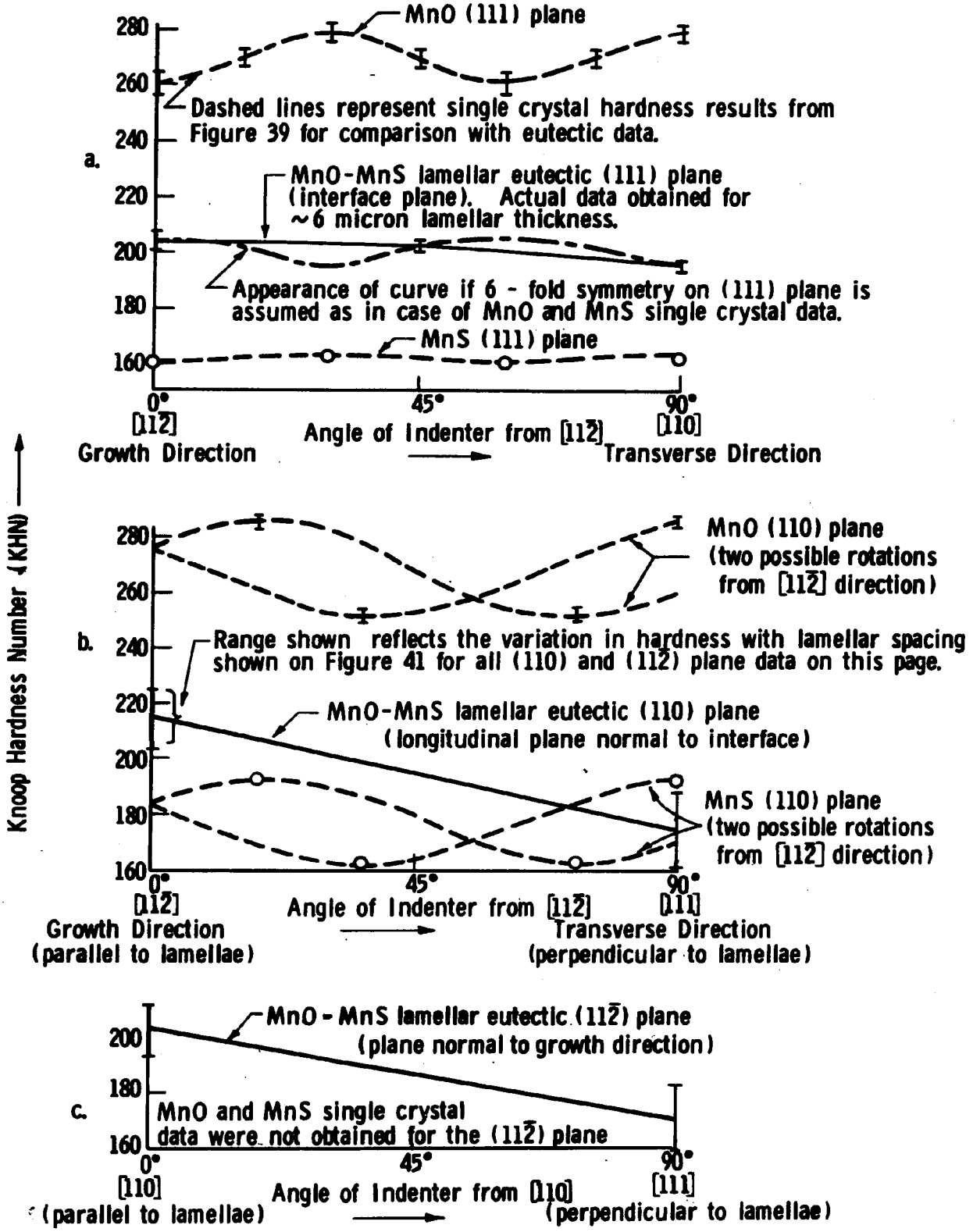


Figure 40. Knoop hardness versus direction on the (111), (110) and (11$\bar{2}$) planes of the MnO-MnS lamellar eutectic and comparison with MnO and MnS single crystal hardness results.

directions are only slightly lower than those in the <110> directions. It is assumed that the hardness in the <112> directions would also be intermediate between those of the <110> and <100> since no values higher than the <110> or lower than the <100> were observed in hardness tests at random orientations between these directions. In the MnO-MnS lamellar eutectic the Knoop hardness is lower when the long indenter axis is aligned perpendicular to the lamellae which is the [111] direction on both the $(11\bar{2})$ and (110) surfaces (Figure 40). The hardness measured with the indenter axis parallel to the lamellae or in the $[11\bar{2}]$ and [110] directions on the (110) and $(11\bar{2})$ surfaces, respectively, was significantly higher than in the [111] direction. Hardness values for indenter orientations intermediate between the parallel and perpendicular orientations were intermediate between the higher parallel and lower perpendicular values but are not plotted in the figures since a significant number of tests was not made. The MnO and MnS single crystal hardness curves for the (110) and (111) planes shown in Figure 40 do not show the same type of variation with direction as do the eutectic hardness curves. The hardness variations for indenter orientations parallel and perpendicular to the eutectic lamellae on the (110) and $(11\bar{2})$ planes are very similar to each other but are quite different from the variations observed in the single crystals of the two phases. Therefore, it must be concluded that the lamellar microstructure is more important in determining directional hardnesses

in the eutectic than the crystallographic hardness characteristics of the single crystal eutectic phases.

The crystallographic orientation effect observed in MnS by Chao and Van Vlack[64] was explained on the basis of the strong preference for $\langle 110 \rangle \{\bar{1}10\}$ slip in this crystal and the number of such slip planes required to operate to accomodate the indentation for each indenter orientation. Since the hardness variations and slip lines observed in MnO are so similar to those of MnS, as discussed previously, it must be assumed that the same explanation holds for the crystallographic hardness variation in MnO. The deviation from the single crystal hardness versus orientation relationship in the oriented eutectic of the two phases must therefore be due to some influence which interferes with the above slip patterns.

b. Microstructural Effects

The microstructure of the MnO-MnS eutectic in the regions where hardness tests were performed consisted of parallel lamellae or plates of the two phases from 3 to 10 microns in width (Figure 12). The crystal structures of the two phases were of the same NaCl-type and were similarly oriented with reference to a common boundary, as discussed above. It would be expected, however, that the inter-lamellar boundary orientation, previous deformation, internal stresses and defects would have some effect on the Knoop indentation hardness versus orientation of this two phase composite.

The hardness with the Knoop indenter axis parallel and perpendicular to the lamellae on both the transverse, $(11\bar{2})$, and longitudinal, (110), section of several MnO-MnS ingots is summarized in Figure 41 for the range of lamellae spacings observed. The curves indicate that when the indenter is parallel to the lamellae on both the longitudinal (110) and transverse $(11\bar{2})$ surfaces the hardness is 35 to 40 kg/mm^2 greater than when it is perpendicular to the lamellae. This seems consistent with the observation in random polycrystalline materials that indentation hardness increases as grain size decreases, since the major deformation should occur at right angles to the elongated Knoop indenter. Thus, the primary slip planes are blocked every one to five microns by interphase boundaries when deformation must occur perpendicular to the lamellae, and not blocked significantly at all when slip can propagate parallel to the lamellae. However, for both parallel and perpendicular indenter orientations, the hardness decreased about 3 kg/mm^2 per micron decrease in lamellar width (Figure 41). This does not support the above qualitative explanation predicting that the hardness should increase for decreasing lamellae width at least for the parallel indenter orientation. It does not refute the above explanation, however, since the lamellae width range studied ($\sim$3 to 10 microns) is so small compared with the difference between the effective interphase boundary width between the parallel and perpendicular orientations ($\sim\frac{1000}{1}$ ratio) that the width effect could well

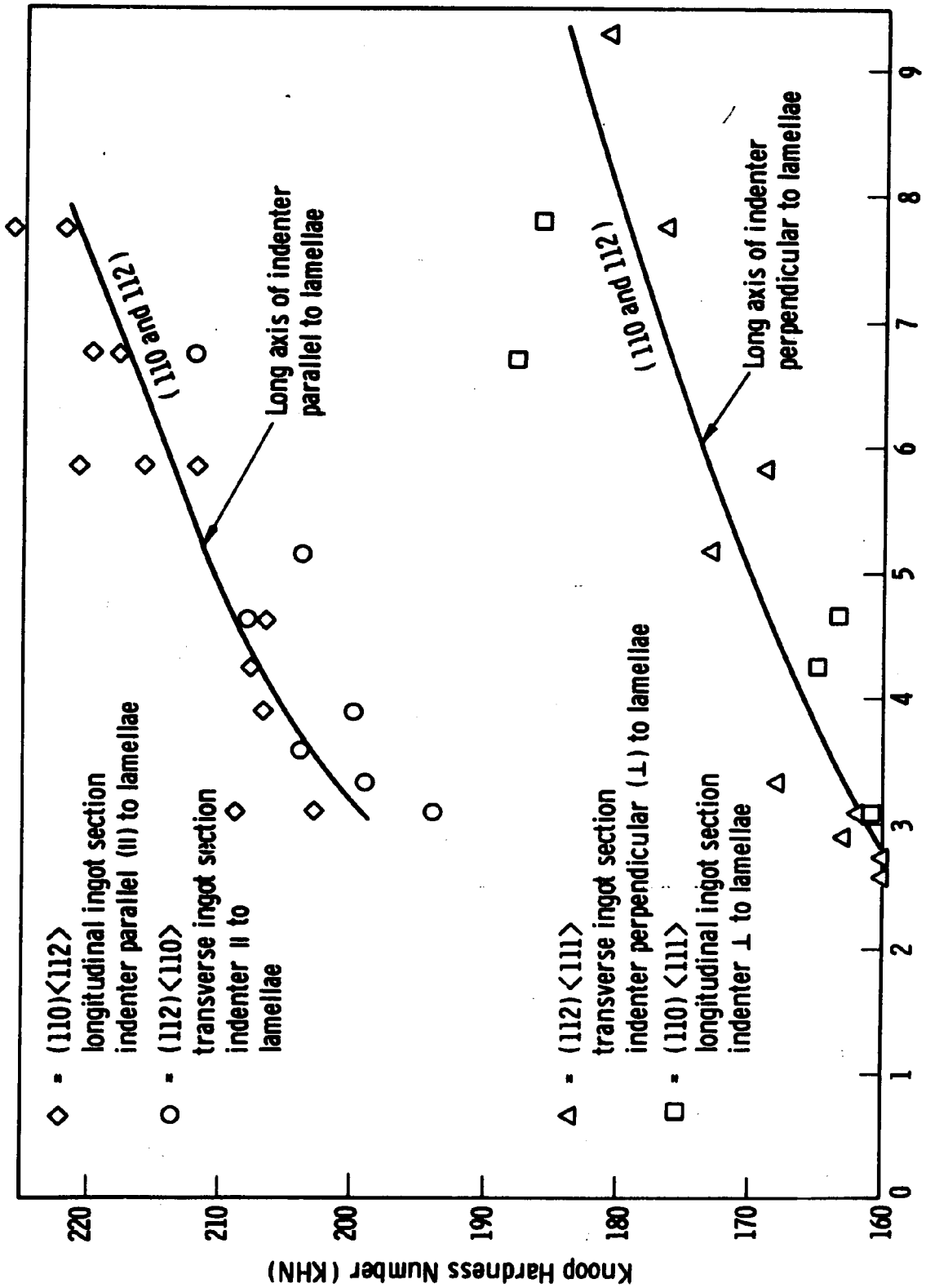


Figure 41. Microstructural variations in the Knoop Hardness Number (KHN) for the MnO-MnS eutectic. Each point represents the average of five hardness readings.

be masked by other changes occurring as the lamellae width decreases. Whatever the factor or factors responsible, they must be equally effective in reducing the hardness for both parallel and perpendicular orientations, and they must increase their effect with decreasing lamellar width, λ, which could also mean with increasing solidification rate. There are several effects which might behave in the above manner, such as (1) impurity distribution, (2) age-hardening, (3) thermal strains, and (4) microcracks.

The distribution of impurities can be affected by altering the solidification rate. If the impurities have a partition coefficient, K_x, less than one, higher solidification rates mean less time for redistribution of rejected impurities away from the solidification front, so that more impurity is retained in the solid. If the solute is retained in solution it will generally tend to cause solution hardening to occur, unless the solubility limit is exceeded and the excess solute precipitated as a softer third phase distributed throughout the eutectic. The only visible third phase in the MnO-MnS eutectic was low-metalloid iron from the crucible which, according to the data of Chao et al,[80] has a room temperature Vickers hardness of 80 kg/mm^2 compared with 145 kg/mm^2 for MnS and 225 kg/mm^2 for MnO. Metallographic examination did not indicate a significant variation in iron particle content with lamellae width. Another type of third phase is the tiny spherical voids distributed throughout the phases. Variations in void content

from grain to grain of the same lamellar width were greater than variations due to lamellar width change alone, making it impossible to correlate the two factors. In addition to acting as a zero-strength phase, such voids could act as crack initiators.

Slower solidification rates might also give an age-hardening effect, while faster rates might not give time for precipitation to occur in the finer spaced lamellae.

The thermal stresses and strains which occur on cooling a two phase lamellar or rod-like eutectic from the eutectic solidification temperature to room temperature could also significantly affect the physical properties of the composite. The change in dimensions of the different phase particles for the same temperature change, ΔT, would be different if each particle were unconstrained and had a different thermal expansion coefficient. If the solid composite is to maintain its structural integrity, however, all phases present must contract at the same rate and for the same total amount as the overall unit, if shear between the phases is negligible. Turner[129] has postulated that stresses acting on individual phase particles under the above conditions are a function of the coefficient of expansion of the composite, α_c, and the phase i, α_i, the temperature difference, ΔT, and bulk modulus, K_i of the phase considered, as below:

$$\sigma i = (\alpha_c - \alpha_i)\ \Delta T\ K_i$$

This relationship assumes that the linear thermal expansion is directly proportional to the cubical expansion coefficient. Using values of the bulk modulus of MnO and MnS calculated from C_{44} shear compliances, the shear stress due to a 1200°C ΔT and a 2×10^{-6}/°C $\Delta\alpha$ would be about 12,000 psi in MnO and 7,200 psi in MnS. This calculation is very approximate, however, since it does not take into account the changes in both elastic modulus and thermal expansion coefficient with temperature over the large temperature range considered, in addition to the many assumptions involved in the estimation of room temperature moduli. Values for the critical shear stress and fracture stress are not available for either MnS or MnO; therefore, it is not possible to state whether plastic deformation or fracture are likely under the imposed thermal stresses.

The total strain for the 1200°C ΔT from the eutectic temperature to room temperature can be calculated on the basis of thermal expansion data reported in another section of this report. It is found to be of the order of 0.24% on a linear basis. This does not appear to be beyond the range of possible elastic strains, but since the yield stress of ionic solids can vary widely due to its sensitivity to the number, type and distribution of defects in the crystal, local plastic strain relief cannot be discounted.

The stress for fracture in a perfect crystal should be about E/π,[78] where E is the elastic modulus normal to the cleavage plane. Due to prior plastic flow and surface

defects, however, the actual fracture stress may be as low as $E/10^5$, which would be below the possible thermal stress levels for the MnO-MnS eutectic. The primary cleavage planes in both MnO and MnS are the {100} planes. There are three {100} planes symmetrically arrayed at angles of 54.7° to the {111} phase boundary on which cleavage might occur. Microcracks were not observed on any planes in the eutectic prior to cleavage or indentation, but {100} cracks were noted around indentations on the transverse $(11\bar{2})$ surface of the eutectic ingots. If microcracks on {100} planes or parallel to the {111} phase boundaries do exist, they must be more severe in the MnO phase since examination of {111} cleavage surfaces indicates that the fracture propagated entirely in the MnO phase. This would not be unexpected since MnO seems to behave in a more brittle fashion by exhibiting {100} tension cracks around small Vickers indentations which are not noted in MnS.

If microcracks or incipient cracks were caused by thermal stresses it would be expected that the number of such cracks per unit area of eutectic would increase with decreasing lamellar spacing, λ. Since a crack cannot transmit shear stresses, it might be expected than an increased density of such cracks would decrease the apparent hardness of the overall eutectic.

It is indicated, therefore, that the microhardness variation with lamellar spacing of the MnO-MnS eutectic might be due to an array of microcracks on {100} planes

along the phase boundary in the MnO phase. The distance between such cracks would decrease as lamellar spacing decreased, thus causing a decrease in hardness. Such microcracks could also cause the anisotropic variation of hardness parallel and perpendicular to the indenter by acting as low shear strength boundaries parallel to the lamellae but not perpendicular to them. The above hypothesis has not been conclusively proven in this study, however.

C. Summary of Results

The following results were obtained in this study:

1. Crystallographic Orientations

a. The equilibrium crystallographic orientation of the two phases in the MnO-MnS eutectic with respect to the interlamellar planes and growth direction has been determined as,

$$\begin{aligned} \text{Interface} &\parallel (111)_{MnO} \parallel (111)_{MnS} \\ \text{Growth Direction} &\parallel [11\bar{2}]_{MnO} \parallel [11\bar{2}]_{MnS} \end{aligned}$$

where $\parallel$ = is parallel to.

b. Analogous alkali halide compound eutectics with the same NaCl-type crystal structure did not show the same relationships as above, but all had low index interfaces and growth directions, as summarized below:

$$\begin{aligned} \text{NaCl-NaF:} \quad \text{Interface} &\parallel (110)_{NaCl} \parallel (110)_{NaF} \\ \text{Growth Direction} &\parallel [001]_{NaCl} \parallel [001]_{NaF} \end{aligned}$$

$$\begin{aligned} \text{NaBr-NaF:} \quad \text{Interface} &\parallel (110)_{NaBr} \parallel (110)_{NaF} \\ \text{Growth Direction} &\parallel [1\bar{1}1]_{NaBr} \parallel [1\bar{1}1]_{NaF} \end{aligned}$$

LiF-NaF: Interface $\parallel (111)_{LiF} \parallel (111)_{NaF}$
Growth Direction $\parallel [1\bar{1}0]_{LiF} \parallel [1\bar{1}0]_{NaF}$

In the halide eutectics with a common cation in the two phases, the interface was a plane containing both cations and anions so that the cation array was essentially continuous across the interface. In the system LiF-NaF where the anion was common to the two phases, an all-anion plane was the interface.

c. The FeO-FeS eutectic, in which the two phases have the NaCl- and NiAs-type structures respectively, exhibited an interface made up of heteropolar $(100)_{FeO}$ and homopolar $(0001)_{FeS}$ planes, as below:

Interface $\parallel (100)_{FeO} \parallel (0001)_{FeS}$
Growth Direction $\parallel [011]_{FeO} \parallel [10\bar{1}0]_{FeS}$

d. A 1 to 3° twist or tilt away from the above exact relationships was sometimes observed. In MnO-MnS the direction of the twist corresponded to the direction of curvature of the eutectic grains.

2. Microstructure

a. Unidirectionally continuous, two phase eutectic microstructures, analogous to those obtained in two component metallic and intermetallic systems, were grown in the following two component ionic compound eutectics: MnO-MnS, FeO-FeS, NaCl-NaF, NaBr-NaF and LiF-NaF.

i. Very uniform, regularly spaced lamellae were observed over large regions of the MnO-MnS and LiF-NaF eutectics. The FeO-FeS, NaCl-NaF, and NaBr-NaF eutectics

exhibited linear arrays of ribbons and rods of their discontinuous phase particles but did not have continuous lamellae over large regions.

ii. The matrix phase and discontinuous phase for each eutectic and their respective calculated volume percents were as follows:

TABLE III
Volume Percent of Matrix and Discontinuous Eutectic Phases

Matrix	Vol. %	Discontinuous	Vol. %
FeS	63.9	FeO	36.1
MnS	56.5	MnO	43.5
NaF	51.3	LiF	48.7
NaCl	76.9	NaF	23.1
NaBr	83.4	NaF	16.6

iii. The relationship between the interlamellar spacing, λ, and solidification rate, R, for MnO-MnS can be represented by a straight line on a plot of logarithm λ versus logarithm R or by a straight line projecting toward the origin in a plot of λ versus $R^{-1/2}$.

iv. Newton bands were observed in both MnO and MnS lamellar phases when they were sectioned at low angles to the plane of the lamellae.

b. A colony structure developed along the length of the ingots in all five systems studied in a manner similar to metallic eutectics.

i. Initial solidification occurred by random

nucleation and growth of eutectic grains in the bottom of the crucible. Some of these grains extended as elongated colonies in the growth direction.

ii. A single cell or convex solidification front developed across the entire ingot diameter and across many eutectic grains in the central parts of MnO-MnS ingots.

iii. The final zone to solidify at the top of the ingots developed a severe colony structure similar to that observed in metallic eutectics. In metallic eutectics this has been attributed to the effect of impurities segregated to the upper end of the ingot during solidification.

iv. Lamellae radially oriented to a convex solidification front did not break down into rods as was the case for lamellae of other orientations to such a front.

c. Irregularities

Several irregularities were observed in the eutectic microstructure.

i. Transverse growth discontinuities or bands were observed at locations in the MnO-MnS ingots corresponding to process interruptions. The transverse bands outlined the solidification front which was normal to the growth direction of the rods or lamellae of the eutectic at all points.

ii. Primary dendrites of MnO tended to occur in the upper ends, and dendrites of MnS tended to occur in the lower ends of vertically solidified MnO-MnS ingots.

iii. Thick, continuous halos of MnS occurred around

MnO dendrites, but thin, discontinuous MnO halos occurred around MnS dendrites.

iv. Fibers and strings of globules of iron were uniformly distributed throughout some regions of MnO-MnS ingots. The iron particles tended to associate with the MnO phase, grain boundaries, transverse bands, and lamellar flaws.

v. Small, nearly spherical voids occurred in uniform dispersions over some regions of the MnO-MnS eutectic. They tended to occur in the MnS phase adjacent to MnO rods and lamellae. They were not observed in regions where there was a high concentration of iron particles.

3. Thermal Expansion

a. The mean thermal expansion coefficient of MnS between 25 and 1000°C was $14.5 \pm 0.5 \times 10^{-6}/°C$.

b. The mean thermal expansion coefficient of the eutectic was $12 \pm 0.5 \times 10^{-6}/°C$. This was lower than that of either the MnS or MnO ($13.5 \times 10^{-6}/°C$) phase.

4. Deformation and Fracture

a. The preferred slip planes around Vickers indentations on (100), (110) and (111) surfaces of MnO were all (110) planes, as in MnS.

b. MnO cleaved preferentially on (100) planes but around Vickers indentations exhibited (110) cracks normal to (100) surfaces at the intersections of (110) slip planes lying 45° to the (100) surface.

c. Slip bands corresponding to (110) planes appeared around indentations on MnO-MnS lamellar eutectic surfaces.

The bands were not altered by crossing phase boundaries.

d. The lamellar MnO-MnS eutectic fractured in the MnO phase parallel to the phase boundary, (111), in unconstrained cleavage but also exhibited {100} cracks around indentations.

5. Hardness

a. The Knoop microhardnesses measured on the (100), (101), and (111) planes of the MnO single crystal are tabulated below for the low index directions at which the long axis of the Knoop indenter was oriented in each plane.

TABLE IV

MnO Single Crystal Knoop Hardness (KHN units)

Plane	Indenter Direction [010]	[011]	[101]	[111]	[112]
(100)	252	282			
(101)	252		286	284	
(111)			276		259

b. The Knoop microhardness values measured for indenter orientations parallel and perpendicular to the lamellae on transverse and longitudinal cross sections of the MnO-MnS ingots are tabulated below. The corresponding crystallographic planes and directions are noted for comparison with the single crystal data.

TABLE V

MnO-MnS Eutectic Knoop Hardness (KHN units)

Indenter orientation to lamellae to [hkl] direction	parallel		perpendicular	
	[110]	[11$\bar{2}$]	[111]	
Indented plane	(11$\bar{2}$)	(110)	(11$\bar{2}$)	(110)
Ingot cross section	transverse	longitudinal	transverse	longitudinal
Hardness value (KHN)	203	215	170	177

Indented plane	(111)	
Indenter orientation	[11$\bar{2}$]	[110]
Hardness value (KHN)	205	195

c. The Knoop microhardness of the MnO-MnS eutectic decreased at an average rate of 3KHN units per micron decrease in lamellar width for all cross sections and indenter orientations.

CHAPTER V

CONCLUSIONS

The following conclusions were reached in this study:

1. Low index crystallographic growth directions and interface planes are preferred by all the lamellar eutectic phases studied.

   a. The same growth direction and interface plane occur in both phases where both phases have the NaCl-type structure.

   b. No two eutectics studied have the same combination of growth direction and interface plane.

   c. Slight crystallographic twist or tilt misorientations (1 to 5°) occur in some cases.

   d. For the MnO-MnS eutectic, the direction of twist is determined by the direction of curvature of the solidification front.

2. Unidirectionally oriented lamellar and rod-like microstructures can be grown in binary alkali halide and oxide-sulfide ceramic compound eutectics by unidirectional solidification.

   a. A lamellar phase morphology is established in the MnO-MnS and LiF-NaF eutectics. A tendency towards this morphology is observed in the other eutectics studied.

   b. The phase of lower volume fraction is discontinuous, and the phase of higher volume fraction is continuous in all cases studied.

c. The interlamellar spacing, λ, of the MnO-MnS eutectic increases as the solidification rate, R, decreases, according to a relationship of the type observed for metallic eutectics:

$$\lambda = AR^{-1/2}.$$

d. Newton bands are observed in thin, wedge-shaped sections of translucent ceramic phases which could be useful in two dimensional microstructural analysis of lamellar eutectics.

3. The eutectic colony structure and its development as solidification proceeds along the length of an ingot is very similar to that observed in metallic eutectics.

a. Many eutectic grains nucleate in an initial zone. Some of these continue to grow as single elongated colonies. A single colony cell forms in the center of the ingot and finally breaks down into many small colonies due to impurity concentration at the end of the ingot which solidifies last.

b. Lamellae oriented radially to a curved solidification front and grains consisting of arrays of such lamellae persist in the eutectic microstructure in preference to those with non-radial orientations with respect to the growth front.

4. Microstructural irregularities occurred in the MnO-MnS lamellar eutectic which were useful in analyzing the eutectic solidification process.

a. Perturbations of furnace conditions or of crucible

motion through the furnace cause transverse discontinuities outlining the solidification front in the eutectic microstructure.

b. Primary MnS dendrites with densities less than the eutectic liquid segregate to the top of the ingot, and the MnO dendrites with higher densities segregate to the bottom.

c. The MnS phase nucleates the MnO-MnS eutectic, but the MnO phase does not.

d. Excess metallic iron from the crucible is uniformly distributed as fibers and strings of globules parallel to the rods or lamellae of the ceramic phases in the MnO-MnS and FeO-FeS eutectics under certain conditions. The iron particles tend to be associated with the MnO phase, eutectic grain boundaries, transverse bands and lamellar flaws.

5. The mean thermal coefficient of expansion from room temperature to 1000°C of the MnO-MnS eutectic ($12 \times 10^{-6}/°C$) is significantly less than that of either the MnS phase ($14.5 \times 10^{-6}/°C$) or the MnO phase ($13.5 \times 10^{-6}/°C$). This is probably due to modification of the eutectic by oxidation or coalescence of non-lamellar phase particles during high temperature dilatometry.

6. The preferred slip planes in MnO and in the MnO-MnS eutectic are {110} types as in the case of MnS.

7. The preferred cleavage plane in the MnO phase is the {100}, as in MnS. The MnO-MnS eutectic exhibits both {100} cleavage and cleavage parallel to the {111} interlamellar

planes in the MnO phase.

8. The Knoop indentation hardness of single crystal MnO and the MnO-MnS lamellar eutectic vary with indentation direction and the scale of the eutectic microstructure.

a. The Knoop hardness of MnO is higher than that of MnS but varies with orientation of the indenter in a manner similar to the variation in MnS.

b. The Knoop hardness of the MnO-MnS eutectic varies primarily with the orientation of the indenter to the lamellae and does not correspond to the crystallographic variations noted in single crystals of the two phases.

c. The Knoop hardness for both perpendicular and parallel orientations of the indenter to the lamellae decreases with decreasing lamellae width.

REFERENCES

1. Chao, H. C., Y. E. Smith and L. H. Van Vlack, "The MnO-MnS Phase Diagram," Trans. AIME, 227, p. 796 (1963).

2. Lyman, Taylor (Ed.), ASM Metals Handbook, American Society for Metals, Metals Park, Novelty, Ohio, p. 7 (1948).

3. Levin, E. M., C. R. Robbins and H. F. McMurdie, "FeO FeS, Fig. 1902," "NaCl-NaF, Fig. 1619," "LiF-NaF, Fig. 1467," "NaBr-NaF-NaI, Fig. 1635," Phase Diagrams for Ceramists, The American Ceramic Society, Columbus, Ohio (1964).

4. Stockdale, D., "Numerical Relationships in Binary Metallic Systems," Proc. Roy. Soc. A, 152, p. 81 (1935).

5. Gorboff, A., J. Soc. Phys.-Chim. Russe, 41, p. 1241 (1909). After ref. 17.

6. Desch, C. H., "Note on the Composition of Eutectic Mixtures," Trans. Faraday Soc., p. 160 (1910).

7. Hume-Rothery, W. and E. Anderson, "Eutectic Compositions and Liquid Immiscibility in Certain Binary Alloys," Phil. Mag., 5, p. 383 (1960).

8. Darken, L. S. and R. W. Gurry, Physical Chemistry of Metals, McGraw-Hill, p. 342 (1953).

9. Hilty, D. C. and W. Crafts, "Manganese Modification of the Fe-S-O System," J. of Metals, AIME (Sept. 1954).

10. Crafts, W. and D. C. Hilty, "Sulphide and Oxide Formation in Steel," Elec. Furnace Steel Proc., AIME, 71 (1953).

11. Gowland, W , "The Early Metallurgy of Silver and Lead, Part I," Archeologia, lvii (1924).

12. Guthrie, F., "On Salt Solutions and Attached Water," Phil. Mag., iv, p. 11 (1875).

13. Brady, F. L., "The Structure of Eutectics," J. Inst. of Metals, 28, p. 372 (1922).

14. Desch, C. H., Textbook of Metallography, Longmans, Greene and Co., London, p. 21 (1918).

15. Scheil, E. "Uber die eutektische Kristallisation," Z. Metallk, 45, p. 298 (1954).

16. Ellwood, E. C. and K. Q. Bagley, "The Structure of Eutectics," J. Inst. Metals, 76, p. 631 (1949).

17. Chadwick, G. A., "Eutectic Alloy Solidification," Prog. in Materials Sci., 12, (1963).

18. Vogel, R., Z. Anorg. Chem., 76, p. 425 (1912). After ref. 17.

19. Lamplough, F. E. E. and J. T. Scott, "The Growth of Metallic Eutectics," Proc. Roy. Soc. A, 90, p. 600 (1914).

20. Loxham, J. G. and A. Hellawell, "Constitution and Microstructure of Some Binary Alkali Halide Mixtures," J. Am. Cer. Soc., 47, pp. 184-188 (1964).

21. Cooksey, D. J. S., D. Munson, M. P. Wilkinson and A. Hellawell, "Directional Freezing of Some Binary Eutectics," Phil. Mag., 10, p. 745 (1964).

22. Penfold, D. and A. Hellawell, "Microstructures of Alkali Halide Eutectics LiF-NaF and NaCl-NaF," J. Am. Cer. Soc., 48, p. 133 (1965).

23. Truelove, P. and A. Hellawell, "Habit Planes between Phases in the Systems NaCl-NaF and LiF-NaF," Phil. Mag., 11, p. 1309 (1965).

24. Pfann, W. G., "Principles of Zone Melting," J. Metals, 4, p. 747 (1952).

25. Gulliver, G. H., Metallic Alloys, Chas. Griffin, London.(1921)

26. Scheuer, E., "Zum Kornseigerungsproblem," Z. Metallk, 23, p. 237 (1931).

27. Hayes, A. and J. Chipman, "Mechanism of Solidification and Segregation in a Low-Carbon Rimming Steel Ingot," Trans. AIME, 135, p. 85 (1939).

28. Rutter, J. W. and B. Chalmers, Can. J. Physics, 31, p. 15 (1935). After ref. 17.

29. Tiller, W. A., K. A. Jackson, J. W. Rutter and B. Chalmers, "The Redistribution of Solute Atoms During the Solidification of Metals," Acta Met., 1, p. 428 (1953).

30. Rutter, J. W. and B. Chalmers, "A Prismatic Substructure Formed During Solidification of Metals," Can. J. Physics, 31, pp. 15-39 (1953).

31. Tiller, W. A and J. W. Rutter, "The Effect of Growth Conditions Upon the Solidification of a Binary Alloy," Can. J. Physics, 34, pp. 96-121 (1956).

32. Weart, H. W. and D. J. Mack, "Eutectic Solidification Structures," Trans. AIME, 212, p. 664 (Oct. 1958).

33. Portevin, A. M., "The Structure of Eutectics," J. Inst. Metals, 29, p. 239 (1923).

34. Rosenhain, W. and P. Tucker, Phil. Trans., 209A, p. 89 (1909). After ref. 17.

35. Chadwick, G. A., "Solidification of Al-$CuAl_2$ Eutectic Alloys," J. Inst. Metals, 91, p. 169 (Jan. 1963).

36. Yue, A. S. "Microstructure of Magnesium-Aluminum Eutectic," Trans. AIME, 224, p. 1010 (1962).

37. Chadwick, G. A., "Modification of Lamellar Eutectic Structures," J. Inst. Metals, 91, p. 298 (1963).

38. Fraser, M. J. and A. A. Burr, "A Simple Semi-micro X-ray Technique," Metal Prog. 70, p. 114 (1956).

39. Eastwood, L. M., "Structure and Origin of the Copper-Cuprous Oxide Eutectic," Trans. AIME, 111, p. 181 (1934).

40. Tiller, W. A., "Polyphase Solidification," Liquid Metals and Solidification, ASM (1957).

41. Chilton, J. P. and W. C. Winegard, "Solidification of a Eutectic Made from Zone-Refined Lead and Tin," J. Inst. Metals, 89, p. 162 (1961).

42. Yue, A. S., "Lamellar Tilt Boundary of Mg-32 Wt. Pct. Al Eutectic," Trans. AIME, 230, p. 39 (Feb. 1964).

43. Kraft, R. W. and D. L. Albright, "Microstructure of Unidirectionally Solidified Al-$CuAl_2$ Eutectic," Trans. AIME, 221, p. 95 (Feb. 1961).

44. Davies, V. deL., "Mechanisms of Crystallization in Binary Eutectic Systems," J. Inst. Metals, 93, p. 10 (1964).

45. Hunt, J. D. and J. P. Chilton, "An Investigation of the Lamella → Rod Transition in Binary Eutectics," J. Inst. Metals, 91, p. 338 (1962).

46. Tammann, G., A Textbook of Metallography (Transl.), The Chem. Cat. Co., New York (1925).

47. Straumanis, W. and N. Brakss, Z. Phys. Chem., 30B, p. 117 (1935). After ref. 17.

48. Brandt, W. H., "Solution of the Diffusion Equation Applicable to the Edgewise Growth of Pearlite," J. Appl. Phys., 16, p. 139 (1945).

49. Zener, C., "Kinetics of the Decomposition of Austenite," Trans. AIME, 167, p. 550 (1946).

50. Tiller, W. A., "Polyphase Solidification," Liquid Metals and Solidification, ASM, Cleveland, Ohio, pp. 276-318 (1958).

51. Li, C. and H. W. Weart, "On Steady State Phase Transformations," J. Metals, 14, p. 86 (1962).

52. Sundquist, B. E. and L. F. Mondolfo, "Heterogeneous Nucleation in the Liquid-to-Solid Transformation in Alloys," Trans. AIME, 221, p. 157 (1961).

53. Sundquist, B. E. and L. F. Mondolfo, "Orientation Relationships in the Heterogeneous Nucleation of Solid Lead from Liquid Lead," Trans. AIME, 221, p. 607 (1961).

54. Van der Merwe, J. H., "Misfitting Monolayers and Oriented Overgrowth," Disc. Faraday Soc., 5, pp. 201-214 (1949).

55. Kraft, R. W., "The Structure of the Mg-Mg_2Sn Eutectic," Trans. AIME, 227, p. 398 (1963).

56. Barrett, C. S., "Orientations in Castings and in Deposited Films, Chap. XX," Structure of Metals, McGraw-Hill, New York, pp. 510-520 (1952).

57. Edmunds, G., "Grain Orientation of Cast Polycrystalline Zinc, Cadmium and Magnesium," Trans. AIME, 143, p. 183 (1941).

58. Kraft, R. W., "Crystallography of Equilibrium Phase Interfaces in Al-$CuAl_2$ Eutectic Alloys," Trans. AIME, 224, p. 65 (1962).

59. Lysaght, V. E., Indentation Hardness Testing, Reinhold, New York (1949).

60. Mott, B. W., Micro-indentation Hardness Testing, Butterworths, London (1956).

61. Tabor, D., The Hardness of Metals, Clarendon Press, Oxford (1951).

62. Williams, S. R., Hardness and Hardness Measurements, ASM, Chicago (1942).

63. Keh, A. S., "Dislocations in Indented Magnesium Oxide Crystals," J. Appl. Physics, 31, pp. 1538-1545 (1960).

64. Chao, H. C., L. Thomassen and L. H. Van Vlack, "Deformation and Fracture of MnS Crystals," ASM Trans. Quart., 57, p. 386 (June 1964).

65. Petty, E. R., "The Hardness Anisotropy of Aluminum Single Crystals," J. Inst. Metals, 91, pp. 54-62 (1962).

66. Partridge, P. G., "The Microhardness Anisotropy of Magnesium and Zinc Single Crystals," J. Inst. Metals, 92, pp. 50-55 (1963).

67. Brace, W. F., "Plastic Deformation of Quartz During Indentation," Geol. Soc. Amer. Bull., 69, p. 1539 (1958).

68. Holm, E., R. Holm and E. I. Schobert, "Theory of Hardness and Measurements Applicable to Contact Problems," J. Appl. Phys., 20, p. 319 (1949).

69. Cottrell, A. H., Dislocations and Plastic Flow, Clarendon Press, Oxford (1953).

70. Brace, W. F., "Experimental Study of the Indentation of Rocks and Minerals," Final Report, NSF Project G4647, Mass. Inst. Tech. (1961).

71. Westbrook, J. H., "Temperature Dependence of Strength and Brittleness of Some Quartz Structures," J. Am. Cer. Soc., 41, pp. 433-440 (1958).

72. Wolff, G. A. et al, "Relationships of Hardness, Energy Gap and Melting Point of Diamond Type and Related Structures," Halbleiter und Phosphore, Brunswick, Vieweg (1958).

73. Englehardt, W. von, "Abrasion Resistance and Surface Energy of Solid Substances," Naturwiss, 33, pp. 195-203 (1946).

74. Kolsky, H., "Some Aspects of Mechanical Testing of Nonmetallic Solids," in Physics of Non-destructive Testing, Brit. J. Appl. Phys. Supp. No. 6, pp. 1-4 (1957).

75. Bernhardt, E. O., "Uber Mikroharte der Feststoffe im Grenzbereich," Z. Metallkunde, 33, pp. 135-144 (1941).

76. Roesler, F. C., "Indentation Hardness of Glass as an Energy Scaling Law," Proc. Phys. Soc. London B, 69, pp. 55-60 (1956).

77. Westbrook, J. H., "Flow in Rock Salt Structures," WADC Tech. Report, 58-304, ASTIA Document AD155651, General Electric Co. Research Lab., p. 6 (1958).

78. Gilman, J. J., "Mechanical Behavior of Ionic Crystals," Progress in Ceramic Science, J. E. Burke, Ed., Pergamon Press, New York, pp. 146-199 (1961).

79. Moore, J. W., in Plastic Deformation of Nonmetallic Phases within Ductile Metals, Ph.D. thesis of R. J. Warrick, Univ. of Michigan (1963) Figure 49, p. 111.

80. Chao, H. C., L. H. Van Vlack, F. Oberin and L. Thomassen, "Hardness of Inclusion Sulfides," ASM Trans. Quart., 57, pp. 885-891 (1964).

81. Gilman, J. J. and W. G. Johnston, "The Origin and Growth of Glide Bands in Lithium Fluoride Crystals," Dislocations and Mechanical Properties of Crystals, J. C. Fisher et al, Eds., Wiley, New York, p. 116 (1956).

82. Stokes, R. J., T. L. Johnston and C. H. Li, "Effect of Surface Condition on the Initiation of Plastic Flow in MgO," Trans. AIME, 215, p. 437 (1959).

83. Dorn, John E. and Jim D. Mote, "On the Plastic Behavior of Polycrystalline Aggregates," Materials Science Research, 1, Stadelmaier and Austin, Eds., Plenum Press, New York, p. 12 (1963).

84. Johnston, T. L., R. J. Stokes and C. H. Li, "Crack Nucleation in Magnesium Oxide Bicrystals Under Compression," Phil. Mag., 7, pp. 23-34 (1962).

85. Day, R. B. and R. J Stokes, "Grain Boundaries and the Mechanical Behavior of MgO," Honeywell Research Report HR-64-292, Contract AF 33(615)-1282 (Dec. 1964).

86. Taylor, G. I., "Plastic Strain in Metals," J. Inst. Metals, 62, p. 307 (1938).

87. Buerger, M. J., "Translation Gliding in Crystals of the NaCl Structure Type," Amer. Mineralogist, 15, pp. 174-187 (1935).

88. Kuznetsov, V. D., Surface Energy of Solids, Transl. from Russian, Her Majesty's Stationery Office, London (1957).

89. Armstrong, R., I. Codd, R. M. Douthwaite and N. J. Petch, "The Plastic Deformation of Polycrystalline Aggregates," Phil. Mag., 7, p. 45 (1962).

90. Day, R. B. and R. J. Stokes, "Grain Boundaries and the Mechanical Behavior of Magnesium Oxide," Honeywell Report HR-64-292, Contract AF-33(615)-1282 (1964).

91. Kocks, U. F., "Polyslip in Polycrystals," Acta Met, 6, pp. 85-94 (1958).

92. Petch, N. J., "The Fracture of Metals," Prog. in Metal Phy., 5, p. 1 (1954).

93. Li, J. C. M., "Petch Relation and Grain Boundary Sources," Trans. AIME, 227, pp. 239-247 (1963).

94. Kochendorfer, A., Plastiche Eigenschaften von Kristallen, Springer, Berlin, p. 22 (1941).

95. Naharoo, F. R. N., Some Recent Developments in Rheology, V. G W. Harrison, Ed., Brit. Rheologists Club, United Trade Press, London, p. 38 (1950)

96. Eshelby, J. D., F. C. Frank and F. R. N. Nabarro, "The Equilibrium of Linear Arrays of Dislocations," Phil. Mag., 42, p. 351 (1951).

97. Bishop, J. F. W. and R. Hill, "A Theory of the Plastic Distortion of a Polycrystalline Aggregate under Combined Stresses," Phil. Mag., 42, p. 414 (1951).

98. Livingston, J. D. and B. Chalmers, "Multiple Slip in Bicrystal Deformation," Acta Met., 5, pp. 322-327 (1957).

99. Adams, N. A. and G. T. Murray, "Direct Observation of Grain Boundary Sliding in Bicrystals of Sodium Chloride and Magnesia," J. Appl. Phys., 33, p. 2126 (1962).

100. Murray, G. T., J. Silgalis and A. J. Mountvala, "Creep Rupture Behavior of MgO Bicrystals," J. Amer. Cer. Soc., 47, p. 531 (1964).

101. Fleischer, R. L. and W. A. Backofen, "Effects of Grain Boundaries in Tensile Deformation at Low Temperature," Trans. AIME, 218, p. 243 (1960).

102. Aust, K. J. and N. K. Chen, "Effect of Orientation Difference on the Plastic Deformation of Aluminum Bicrystals," Acta Met., 2, pp. 632-638 (1954).

103. Clark, R. and B. Chalmers, "Mechanical Deformation of Aluminum Bicrystals," Acta Met., 2, pp. 80-86 (1954).

104. Elbaum, C., "Plastic Deformation of Aluminum Multicrystals," Trans. AIME, 218, pp. 444-448 (1960).

105. Westwood, A. R. C., "On the Fracture Behavior of Magnesium Oxide Bicrystals," Phil. Mag., 6, p. 195 (1961).

106. Austin, J. B., "Thermal Expansion of Nonmetallic Crystals," J. Am. Cer. Soc., 35 (Oct. 1952).

107. Wooster, W. A., A Textbook on Crystal Physics, Cambridge University Press, London (1938).

108. Ellefson, B. S. and N. W. Taylor, "Crystal Structures and Expansion Anomalies of MnO, MnS, FeO, Fe_3O_4 Between 100°K and 200°K," J. Chem. Phys., 2, p. 58 (1934).

109. Foex, Marc, "A Type of Transformation Common in the Lower Oxides of Mn, Fe, Co and Ni," Compt. rend., 227, pp. 193-194 (France) (1948).

110. Kingery, W. D., "Note on Thermal Expansion and Microstresses in Two-Phase Compositions," J. Am. Cer. Soc., 40, p. 351 (Oct. 1957).

111. Turner, P. S., "Thermal Expansion Stresses in Reinforced Plastics," J. Res. Nat. Bur. Stds., 37, pp. 239-250, RP1745 (1946).

112. Kerner, E. H., "Elastic and Thermoelastic Properties of Composite Media," Proc. Phys. Soc. London B, 69, pp. 808-813 (1956).

113. Laszlo, F., "Tessellated Stresses, Part I," J. Iron and Steel Inst., 148, pp. 173-199 (1943).

114. Fulrath, R. M., "Model Polyphase Ceramic Systems and Resultant Stress Systems," Mechanical Properties of Engineering Ceramics, Kriegel and Palmour, Eds., Interscience, p. 549 (1960).

115. Lauchner, J. H., "Mechanical Behavior of Ceramic Composites," Mechanical Properties of Engineering Ceramics, Kriegel and Palmour, Eds., Interscience, p. 575 (1960).

116. Swanson, H. E., R. K. Fuyat and G. M. Ugrinie, "Standard X-ray Diffraction Powder Patterns," NBS Circular 539, 4, p. 11 (1955).

117. Bonizewski, T. and R. G. Baker, "Dislocations in Manganese Sulfide Inclusions in Steel," Acta Met., 11, pp. 990-992 (1963).

118. Buerger, M. J., "The Photography of the Reciprocal Lattice," Am. Soc. X-ray and Electron Diffraction Monograph No. 1 (1944).

119. "Manual for the Use of the Buerger Precession Camera," Charles Supper Co., Watertown, Mass.

120. Campbell, W. J., "Platinum Expansion Values for Thermal Calibration of High Temperature X-ray Diffraction Cameras and Diffractometers," U.S. Bureau of Mines Information Circular IC8107 (1962).

121. "Instructions for Assembly and Operation of the Dilatometer Model HTV," Ernst Leitz Wetzlar, p. 15. (Data from Phys. Techn. Reichsanstalt)

122. Strong, John, Concepts of Classical Optics, W. H. Freeman Co., San Francisco (1958).

123. Sundquist, B. E., R. Bruscato and L. F. Mondolfo, "The Structure of Eutectics," J. Inst. Metals, 91, pp. 204-208 (1962).

124. Davies, G. J., "Anomalous Segregation in Tin-Rich Copper-Tin Alloys," J. Inst. Metals, 93, pp. 197-199 (1965).

125. Kawai, T. and A. Keller, "On the Gradient Column Method of Measuring Densities; with Particular Reference to Its Application to Polymer Single Crystals," Phil. Mag., 8, p. 1973 (1963).

126. Cole, G. S. and W. C. Winegard, "Thermal Convection during Horizontal Solidification of Pure Metals and Alloys," J. Inst. Metals, 93, pp. 153-164 (1964).

127. Kenyon, R. L., "Structure and Properties of Iron," Metals Handbook, T. Lyman, Ed., ASM, Metals Park, Novelty, Ohio, p. 427 (1948). (Data after Hidnert)

128. Smith, C. F., W. B. Crandall and R. B. Burdick, "Research on Thermal Properties of Zirconia," Office of Aerospace Research ARL-64-219 (Dec. 1964).

129. Turner, Phillip S., "Thermal Expansion Stresses in Reinforced Plastics," J. Res. N.B.S., 37, R.P.1745, p. 239 (Oct. 1946).

130. Kerner, E. H., "Elastic and Thermoelastic Properties of Composite Media," Proc. Phys. Soc. London B, 69, pp. 808-813 (1956).

131. Rosenfield, A. R. and B. L. Averbach, "Effect of Stress on the Expansion Coefficient," J. Appl. Phys., 27, p. 154 (Feb. 1956).

132. Rosenholtz, J. L. and D. T. Smith, "The Effect of Compressive Stresses on the Linear Thermal Expansion of Magnesium and Steel," J. Appl. Phys., 21, p. 396 (May 1950).

133. Hordon, M. J., B. S. Lement and B. L. Averbach, "Influences of Plastic Deformation on Expansivity and Elastic Modulus of Aluminum," Acta Met., 6, p. 446 (June 1958).